

INFORMATION TO USERS

This manuscript has been reproduced from the microfilm master. UMI films the text directly from the original or copy submitted. Thus, some thesis and dissertation copies are in typewriter face, while others may be from any type of computer printer.

The quality of this reproduction is dependent upon the quality of the copy submitted. Broken or indistinct print, colored or poor quality illustrations and photographs, print bleedthrough, substandard margins, and improper alignment can adversely affect reproduction.

In the unlikely event that the author did not send UMI a complete manuscript and there are missing pages, these will be noted. Also, if unauthorized copyright material had to be removed, a note will indicate the deletion.

Oversize materials (e.g., maps, drawings, charts) are reproduced by sectioning the original, beginning at the upper left-hand corner and continuing from left to right in equal sections with small overlaps. Each original is also photographed in one exposure and is included in reduced form at the back of the book.

Photographs included in the original manuscript have been reproduced xerographically in this copy. Higher quality 6" x 9" black and white photographic prints are available for any photographs or illustrations appearing in this copy for an additional charge. Contact UMI directly to order.

UMI

A Bell & Howell Information Company
300 North Zeeb Road, Ann Arbor, MI 48106-1346 USA
313/761-4700 800/521-0600

ULTRAFAST CARRIER DYNAMICS AND ENHANCED ELECTROABSORPTION
IN (Ga,In)As/(Al,In)As ASYMMETRIC DOUBLE QUANTUM WELL
STRUCTURES

by

Mark Francis Krol

Copyright © Mark Francis Krol 1995

A Dissertation Submitted to the Faculty of the
COMMITTEE ON OPTICAL SCIENCES (GRADUATE)

In Partial Fulfillment of the Requirements
For the Degree of

DOCTOR OF PHILOSOPHY

In the Graduate College

THE UNIVERSITY OF ARIZONA

1995

UMI Number: 9603386

Copyright 1995 by
Krol, Mark Francis
All rights reserved.

UMI Microform 9603386
Copyright 1995, by UMI Company. All rights reserved.

This microform edition is protected against unauthorized
copying under Title 17, United States Code.

UMI

300 North Zeeb Road
Ann Arbor, MI 48103

THE UNIVERSITY OF ARIZONA
GRADUATE COLLEGE

As members of the Final Examination Committee, we certify that we have read the dissertation prepared by Mark Francis Kroi entitled Ultrafast Carrier Dynamics and Enhanced Electroabsorption in (Ga,In)As/(Al,In)As Asymmetric Double Quantum Well Structures

and recommend that it be accepted as fulfilling the dissertation requirement for the Degree of Doctor of Philosophy

Nasser Peyghambarian



7/27/95

Date

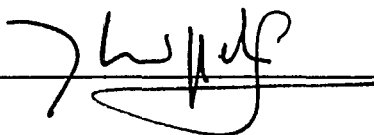
Rudolf Binder



7-27-95

Date

Bernard Kippelen



7/27/95

Date

Date

Date

Final approval and acceptance of this dissertation is contingent upon the candidate's submission of the final copy of the dissertation to the Graduate College.

I hereby certify that I have read this dissertation prepared under my direction and recommend that it be accepted as fulfilling the dissertation requirement.

Nasser Peyghambarian
Dissertation Director



7/27/95

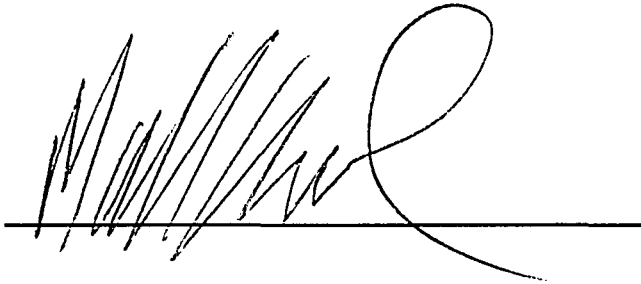
Date

STATEMENT BY AUTHOR

This dissertation has been submitted in partial fulfillment of requirements for an advanced degree at The University of Arizona and is deposited in the University Library to be made available to borrowers under rules of the Library.

Brief quotations from this dissertation are allowable without special permission, provided that accurate acknowledgment of source is made. Requests for permission for extended quotation from or reproduction of this manuscript in whole or in part may be granted by the copyright holder.

SIGNED: _____

A handwritten signature in black ink, consisting of several overlapping, slanted strokes followed by a large, circular flourish on the right side. The signature is written over a solid horizontal line.

ACKNOWLEDGMENTS

I thank my advisor, Prof. Nasser Peyghambarian, for his direction and expertise during my dissertation research. I also want to thank Prof. Galina Khitrova for many helpful discussions and the MBE growth of the samples used in the ultrafast tunneling experiments.

I owe a great thanks to my colleagues Sergey Ten and Brian McGinnis at the Optical Sciences Center for many hours of hard work and long discussions concerning the ultrafast experiment and theory. I also wish to acknowledge Paulo Guerreiro and Sang-Goo Lee for many helpful discussions.

All of the samples used in the modulator work were fabricated by Rich Leavitt and John Pham of the Army Research Laboratory in Adelphi, MD. I owe Rich an additional thanks for many helpful discussions concerning the design of the diode structures.

I thank Steve Johns, Ray Boncek, and John Stacy at the RL Photonics Center. Their support and friendship has been invaluable over the past six years. Additionally, I wish to acknowledge Doug Norton for writing the computer code to control the spectroscopy system and Mike Hayduk for his work on our initial electroabsorption studies. I also thank Andy Pirich and Jim Cusack of the RL Photonics Center for giving me the opportunity and the time to finish my degree.

I would like to thank my wife Lisa for her support and understanding during my graduate career. Surely, Lisa has felt the pressures of obtaining a doctorate just as I have - thanks for your tolerance Lisa. I also want to thank my two sons, Matt and Jeff, for making sure I kept my priorities straight at home.

Finally, I want to thank my mom and dad, Cynthia and Frank, for providing me with the opportunities I have had in life. Hopefully, I will be able to give my children the same opportunities they have given me. If it were not for them, I surely would not have had the opportunity to pursue this doctorate.

DEDICATION

I would like to dedicate this dissertation to my family

Lisa, Matt, and Jeff

and to my parents

Cynthia and Frank

TABLE OF CONTENTS

	Page
LIST OF FIGURES	9
LIST OF TABLES	14
ABSTRACT	15
1. INTRODUCTION	16
2. CARRIER DYNAMICS IN ASYMMETRIC DOUBLE QUANTUM WELLS	24
2.1 ADQW Sample Design	25
2.2 Sample Fabrication and Characterization	33
2.3 Time-Resolved Measurement System	38
2.4 Experimental Results	46
2.5 Discussion	49
2.6 Summary of Experimental Results	56
3. ULTRAFAST HOLE TUNNELING THEORY	57
3.1 Valence Band Structure Calculations	57
3.2 ADQW Valence Band Dispersion	66
3.3 Hole Tunneling Times	71
3.4 Discussion	76
3.5 Conclusions	78

TABLE OF CONTENTS - *Continued*

		Page
4.	ELECTROABSORPTION IN ASYMMETRIC DOUBLE QUANTUM WELLS	79
4.1	The Quantum Confined Stark Effect	79
4.2	Field-Dependent Excitonic Effects in ADQWs	89
4.3	Discussion	95
5.	ENHANCED ELECTROABSORPTION IN DOPED ASYMMETRIC DOUBLE QUANTUM WELLS	98
5.1	Real-Space Electron Transfer in ADQWs	99
5.2	Concept and Model	104
5.3	Low Temperature Results	116
5.3	Room Temperature Results	124
5.5	Summary	128
6.	SUMMARY AND SUGGESTIONS FOR FUTURE RESEARCH	130
6.1	Summary	130
6.2	Suggestions for Future Research	133

TABLE OF CONTENTS - *Continued*

	Page
APPENDIX A. FERMIS GOLDEN RULE	135
APPENDIX B. INTER/INTRA-SUBBAND SCATTERING MECHANISMS	138
REFERENCES	148

LIST OF FIGURES

Figure	Page
2-1 Schematic illustration of the electron and hole processes of interest in ADQW structures	25
2-2 Schematic diagram of the multiple-layer model of a semiconductor quantum well structure	26
2-3 Tunnel barrier width dependence of the first two electron bound state energies of a 40/L _b /60 ADQW structure	28
2-4 Probability densities of the first two electron bound states of a 40/25/60 ADQW structure	30
2-5 Tunnel barrier width dependence of the first two heavy hole and light hole bound state energies of a 40/L _b /60 ADQW structure	31
2-6 Probability densities of the first two heavy hole and light hole bound states for a 40/25/60 ADQW structure	32
2-7 Measured 77 K absorbance spectra of eight ADQW samples	35
2-8 Measured 77 K PL spectra of the ADQW samples	37
2-9 Schematic diagram of the KLM Ti:Sapphire laser used as the pump in the time-resolved pump/probe measurement system	38
2-10 Schematic diagram of the CW Cr:Forsterite laser used as the probe in the time-resolved pump/probe measurement system	39
2-11 Schematic diagram of the upconversion pump/probe system	41
2-12 Schematic diagram of how the reference pulse uses sum-frequency generation to time-resolve probe transmission changes	43
2-13 Illustration of the electron and hole tunneling processes investigated using the non-degenerate pump/probe system	45

LIST OF FIGURES - *Continued*

Figure	Page
2-14 Time-resolved differential transmission data for sample 40/27/60 at various carrier densities	47
2-15 Time-resolved differential transmission data for sample 40/37/60 at various carrier densities	48
2-16 Time-resolved differential transmission data for sample 40/100/60 at various carrier densities	49
2-17 Schematic diagram of the phonon assisted electron processes considered in the calculation of the electron tunneling times	52
2-18 Tunnel barrier width dependence of the fast recovery component at low carrier densities	54
2-19 Carrier density dependence of the fast recovery component for sample 40/27/60	55
3-1 Calculated valence band structure of a 80 Å GaAs/Ga _{0.7} Al _{0.3} As single quantum well	65
3-2 Valence band dispersion for the first four subbands of the 40/27/60 ADQW structure	67
3-3 Hole wavefunction of the HH ^N ₁ subband at various in-plane momenta . . .	68
3-4 Valence band dispersion for the first four subbands of the 40/27/60 ADQW structure in the absence of spin-orbit coupling	69
3-5 Hole wavefunction of the HH ^N ₁ subband at various in-plane momenta in the absence of spin-orbit coupling	70
3-6 Calculated dependence of the impurity-assisted tunneling time on initial state in-plane momentum	74

LIST OF FIGURES - *Continued*

Figure	Page
3-7	Calculated dependence of the alloy-assisted tunneling time on initial state in-plane momentum 75
4-1	Schematic diagram of an infinite potential quantum well of width L 82
4-2	Well width dependence of the Stark shift for the lowest energy optical transition of an infinite potential quantum well 84
4-3	Evolution of the $n = 1$ bound state of a finite-potential quantum well as a function of increasing external field 86
4-4	Room temperature optical absorbance spectra of a 40/35/70 ADQW structure at various applied voltages 88
4-5	Schematic diagram of an ADQW structure with the applied field equal to zero, the resonance field, and some value beyond resonance 90
4-6	Anti-crossing behavior of the $n = 1$ and $n = 2$ electron levels of a 70/30/100 ADQW structure 91
4-7	Measured NW heavy-hole excitonic absorbance spectra at fields near the resonance value 92
4-8	Measured absorbance spectra at fields near the resonance value over a wavelength range encompassing both NW and WW transitions 94
4-9	Schematic diagram showing the origin of the different resonance fields for the NW and WW excitonic transitions 96
5-1	Time-integrated PL spectra of a 40/35/70 ADQW structure at different applied reverse biases 101
5-2	Schematic diagram of the ADQW structure illustrating the relevant optical transitions at different applied fields 102

LIST OF FIGURES - *Continued*

Figure	Page	
5-3	PL peak positions as a function of applied reverse bias for various pump intensities showing the effects of space-charge buildup	103
5-4	Conduction and valence band structure of the doped ADQW modulator .	105
5-5	Field-dependence of the energy separation between the first electron levels in the WW and NW for different carrier densities	110
5-6	Minimum energy transition in the 40/35/70 ADQW structure as a function of applied field for various carrier densities	111
5-7	Electron density of the WW and NW as a function of applied field	113
5-8	Calculated 50 K free-carrier absorption spectra of the 50/35/70 ADQW structure at various applied fields	114
5-9	Apparent shift of the WW band edge for the doped 50/35/70 ADQW structure as a function of applied field	115
5-10	Measured absorbance spectra of the doped modulator for applied fields of 0 and 74 kV/cm	117
5-11	Measured decrease in the PL FWHM width as a function of applied field	119
5-12	Measured PL emission spectrum showing the red shift of the short-wavelength edge with increasing applied field	120
5-13	Measured absorbance spectra of the undoped 40/35/70 ADQW structure at applied fields of 0 and 74 kV/cm	121
5-14	Comparison of the band edge shifts for the doped and undoped ADQW structures	123
5-15	Calculated 300 K free-carrier absorption spectra of the 50/35/70 ADQW structure at various applied fields	125

LIST OF FIGURES - *Continued*

Figure		Page
5-16	Measured I-V characteristics of the n-i-n diode used to apply the external field for the doped ADQW structure	126
5-17	Schematic diagram of a ADQW period with n-type superlattice and p-type delta-doped barrier to suppress current flow	127

LIST OF TABLES

Table		Page
2.1	Room temperature ternary material data	27
2.2	Conduction and valence band offset data	28
2.3	Parameters used to calculate the LO-phonon assisted electron tunneling times	53

ABSTRACT

An experimental study, utilizing a novel nondegenerate transmission pump/probe technique, of ultrafast electron and hole tunneling in (Ga,In)As/(Al,In)As asymmetric double quantum wells (ADQWs) is presented. A single time constant is observed at low carrier densities indicating the holes tunnel from the narrow well (NW) to the wide well (WW) at least as fast as electrons. At high carrier densities a two component decay is observed, consistent with phase-space filling and space-charge effects blocking tunneling carriers. The fast transfer of electrons was confirmed to be a LO-phonon assisted process. A detailed theoretical study of ultrafast hole tunneling at low carrier densities indicates that in ternary materials alloy disorder is responsible for fast hole transfer between the wells.

Enhanced electroabsorption in selectively doped (Ga,In)As/(Al,In)As ADQWs by the use of real space electron transfer is demonstrated. The electron concentration in both the WW and NW is investigated by field-dependent absorption and photoluminescence spectroscopy. The results are compared to absorption changes in an undoped ADQW structure which utilizes the quantum confined Stark effect. The doped modulator exhibits a significantly larger red-shift with applied field than the undoped structure.

CHAPTER 1

INTRODUCTION

The optical properties of semiconductor heterostructures have been the topic of intense research and development for the past decade. Indeed, many new interesting physical phenomena and novel optical devices have been demonstrated.[1] A majority of the research and development utilized GaAs-based semiconductor heterostructures. The GaAs/(Ga,Al)As multiple quantum well (MQW) system was studied intensely since these materials are easily grown by molecular beam epitaxy (MBE) and the required optical testing equipment, i.e. tunable and ultrafast laser systems, were readily available for investigation of the materials optical properties in the 850 nm region of the optical spectrum.

Recently, however, optical interconnects and fiber-based communications systems have emerged as the most promising photonics technologies.[2] Many of these systems require devices which are compatible with the optical fiber transmission windows of 1.3 and 1.5 μm . The wavelength requirement of these applications renders GaAs-based materials and devices useless since the wavelength region in which the GaAs/(Ga,Al)As MQW materials have large optical and electro-optic nonlinearities is not compatible with the transmission wavelengths of optical fiber. As a result, ternary materials lattice-matched to InP are becoming technologically important since these materials can be

readily designed to have large optical and electro-optic nonlinearities in the 1.3 and 1.5 μm wavelength regions.[3] In this dissertation, a study of ultrafast carrier dynamics and electroabsorption in ternary asymmetric double quantum wells (ADQWs) is presented.

Ultrafast carrier dynamics, i.e. electron and hole tunneling, in ADQWs have been intensely studied for the pursuit of fundamental physics and optical and opto-electronic device applications. Most studies of carrier dynamics in ADQWs have utilized the GaAs/(Ga,Al)As heterostructure system. However, ternary ADQWs which are compatible with optical fiber-based applications, have only been the subject of one study.[4] The first investigation of electron tunneling, to the best of our knowledge, was performed by Tsuchiya, et al. using GaAs/AlAs double-barrier heterostructures.[5] A number of investigations in unbiased GaAs/(Ga,Al)As ADQWs by several groups followed the initial study.[6,7] Resonant and nonresonant electron tunneling was also studied in biased ADQW structures.[8,9] The studies of nonresonant electron tunneling in biased structures provided evidence that the interaction of electrons with longitudinal optical (LO) phonons was the dominant mechanism resulting in picosecond electron tunneling when the separation between the first two electron energy levels was greater than the LO phonon energy.[10] Deveaud, et al. presented a comprehensive experimental study of electron tunneling in GaAs/(Ga,Al)As ADQWs showing that electrons can tunnel between the wells with transfer times approaching 2 ps when the electron levels are near resonance and the barrier is thin enough.[11] Exciton dynamics have also been

studied in ADQW structures.[12,13] Experimental and theoretical studies of hole tunneling in ADQW structures have also been performed.[14,15] Fast hole tunneling between the wells may occur when there are resonances between hole subbands due to the presence of an applied electric field [16,17] or due to valence band mixing between subbands associated with the individual wells.[18] In all of the work referenced, time-resolved photoluminescence (PL) was used to investigate the carrier dynamics. The PL techniques typically yield a single time-constant curve where the time-constant corresponds to the transfer time of either electrons, holes, or both between the wells. Transmission techniques, on the other hand, have only been used in a few studies of carrier dynamics in ADQWs.[19,20]

Electroabsorption in ADQW structures has also received considerable research attention. The coupled nature of ADQWs leads to enhanced field-dependent effects in quantum wells structures.[21] The anti-crossing behavior of bound state levels in the presence of an applied field leads to the delocalization of the electron or hole envelope wavefunctions. The result is an enhanced Stark shift of the band edge absorption spectrum.[22,23] The enhancement is particularly useful for applications such as optical fiber compatible devices where narrow well widths are required to maintain wavelength compatibility.[24] Novel field-dependent excitonic effects in coupled quantum wells have also been thoroughly investigated.[25,26]

More recently, there has been considerable interest in the use of modulation-doped quantum well structures to enhance the electro-optic performance of semiconductor modulators. Sawaki, et al. were the first to demonstrate the ability to control the spatial location of an excess electron density in ADQW structures with an external field applied parallel to the quantum well planes.[27] The application of real space electron transfer to (Ga,Al,In)As quantum well electroabsorption modulators was first demonstrated by Wegener, et al.[28] The device utilized the spatial transfer of excess electrons from a doped reservoir to a single quantum well in the presence of an external field applied perpendicular to the quantum well plane. The excess electron density in the quantum well effectively quenches the band edge absorption.[29,30] Vodjdani, et al. used modulation-doped GaAs/(Ga,Al)As ADQWs and real space electron transfer to develop a novel intersubband absorption modulator for infrared applications.[31] The device relied on the transfer of excess electrons between the coupled wells to populate or de-populate the ground-state level of the intersubband transition.[32]

The research presented in this dissertation can be divided into three phases. The initial work was the development of an all-optical asymmetric Fabry-Perot reflection modulator for use at 1.3 μm .[33] The project started as a Master's thesis with the end result being the work presented in this dissertation. A detailed account of the theoretical modeling, design, and demonstration of the modulator can be found in Reference 34. We

demonstrated an on/off contrast ratio in excess of 1000:1 and an insertion loss of only 2.2 dB. The operating bandwidth of the modulator was large, achieving an on/off contrast ratio of greater than 100:1 over a 5 nm optical band. The operating speed of the modulator was found to approach 1 GHz.

Although the modulator was demonstrated to have excellent performance characteristics in terms of contrast ratio and insertion loss, the operating speed of the device is limited by the recombination time of the electrons and holes in the spacer material. The speed requirements of optical interconnect applications require that the device must turn-on *and* turn-off on picosecond time-scales.[2] Since the nonlinearities utilized rely on the generation of real carriers, the turn-on speed can be fast, i.e. < 1 ps, if short optical pulses are used. The turn-off time, however, is the primary factor which limits operational speed. An alternative to using conventional quantum wells as the spacer material is to use asymmetric double quantum wells (ADQWs). As will be discussed in the next chapter ADQWs can be designed to have recovery times of less than 10 ps. Hence, these materials may be useful as nonlinear spacers for all-optical asymmetric reflection modulators.

An additional limitation of the modulator is that, even for low-speed applications, the device relies on optical control. This is not always desirable since the original control signals are usually electronic (i.e. TTL or ECL) in form, making the need for electronic-to-optical conversion and ultimately optical control signals impractical. An obvious solution

is to use electronic control signals and the quantum confined Stark effect (QCSE). However, for (Ga,In)As/(Al,In)As quantum wells, the QCSE is small for the well widths required to obtain wavelength compatibility. As will be discussed in the following chapters, real-space electron transfer in ADQWs may be an attractive alternative to conventional quantum well structures for electroabsorption applications such as the asymmetric reflection modulator.

The second phase was a study of carrier dynamics in (Ga,In)As/(Al,In)As ADQW structures.[35] The study is the first investigation, to the best of our knowledge, of electron and hole tunneling in this material system. The results are particularly interesting since a novel nondegenerate time-resolved pump/probe system was utilized. The transmission system employed a femtosecond Ti:Sapphire laser and continuous-wave Cr:Forsterite laser. Femtosecond time resolution was obtained through the use of sum-frequency generation in a nonlinear crystal. It was found that electrons tunnel with picosecond speeds in these materials due to interaction with LO phonons. Additionally, the study reveals for the first time that holes can tunnel as fast or faster than electrons when the carriers are generated away from the Brillouin zone center. The experimental findings are supported by a theoretical study of hole tunneling. The study revealed that the randomly fluctuating alloy potential provides a very efficient mechanism for hole transfer in the presence of strong mixing between valence subbands.

The final phase of the research was the development of a selectively doped (Ga,In)As/(Al,In)As ADQW electroabsorption modulator.[36] The device utilized an external field and real space electron transfer to control the spatial location of excess electrons in the system. The modulator is the first demonstration of efficient field-dependent absorption modulation using excess electron transfer in ADQWs. The performance of the doped modulator was compared to an undoped ADQW structure which utilized only the quantum confined Stark effect. The doped structure was found to exhibit a field-dependent red shift which was six times larger than the red shift exhibited by the undoped structure.

The dissertation report is organized into six chapters, including this introduction. The experimental investigation of electron and hole tunneling in (Ga,In)As/(Al,In)As ADQWs is presented in Chapter 2. The up-conversion pump/probe system is also described along with a discussion on the design and characterization of the MBE grown samples. Chapter 3 provides a detailed description of the theory used to model the hole dynamics in ADQW structures. A description of the method used to solve the 4x4 Luttinger Hamiltonian is given, and then the resultant band structure is used to determine the hole tunneling rates assuming ionized impurity and alloy fluctuations are the dominant scattering mechanisms in the valence band. A review of the quantum confined Stark effect and novel field-dependent excitonic effects in ADQWs is presented in Chapter 4. Electroabsorption in selectively doped (Ga,In)As/(Al,In)As ADQWs is discussed in

Chapter 5. A simple self-consistent model which can be used to predict the performance of doped structures is presented along with an experimental study of real space transfer of excess electrons in undoped ADQW structures. Finally, Chapter 6 summarizes the results of the research and describes possible future research directions.

CHAPTER 2

CARRIER DYNAMICS IN ASYMMETRIC DOUBLE QUANTUM WELLS

Asymmetric double quantum wells (ADQWs) are of interest for applications such as optical networks where high speed all-optical and optoelectronic devices are required. ADQWs consist of a wide quantum well (WW) coupled to a narrow quantum well (NW) by a thin tunnel barrier as shown in Fig. 2-1. Recently, rapid electron tunneling has been observed in GaAs/(Ga,Al)As ADQWs by a number of groups.[6-13] However, these materials are incompatible with the optical fiber transmission windows of 1.3 and 1.5 μm . In this chapter, an experimental study of carrier dynamics in (Ga,In)As/(Al,In)As ADQWs will be presented.[35] These ternary materials are fully compatible with optical fiber based systems and are useful for optical communications device applications. The results presented here represent, to the best of our knowledge, the first study of carrier dynamics in ternary ADQWs. The results are significantly different from those reported on GaAs/(Al,Ga)As based structures and is a consequence of the disordered nature of the ternary materials and the unique experimental conditions under which we investigated the carrier dynamics.

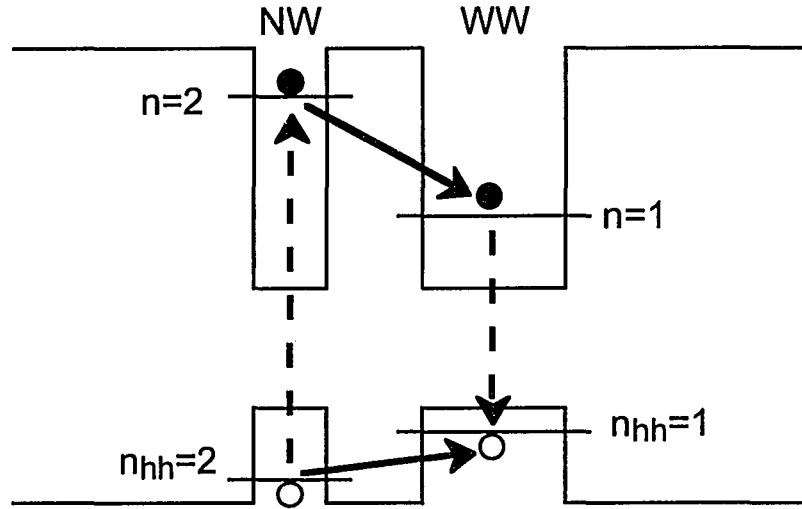


Figure 2-1 Schematic illustration of an ADQW structure and the electron and hole processes of interest in ADQW structures. The dashed lines represent optical transitions, and the solid lines represent transitions involved in the tunneling of electrons and holes.

2.1 ADQW Sample Design

The ADQW samples were designed using a 2x2 matrix formalism described by Kolbas, et al.[37] This formalism is similar to that used for the design of multiple-layer optical structures and relies on matching the following two boundary conditions at each interface of the quantum well structure:

$$\chi_j(z)\Big|_{z=z_j} = \chi_{j+1}(z)\Big|_{z=z_j} \quad (2.1a,b)$$

$$\frac{1}{m_j^*} \left(\frac{\partial \chi_j(z)}{\partial z} \right) \Big|_{z=z_j} = \frac{1}{m_{j+1}^*} \left(\frac{\partial \chi_{j+1}(z)}{\partial z} \right) \Big|_{z=z_j}$$

where $\chi(z)$ and m^* are the envelope wavefunctions and effective masses in the j and $j+1$ layers, respectively, and z_j is the location of the interface between the j and $j+1$ layers.

The wavefunctions in each layer are assumed to be of the form

$$\chi_j(z) = A_j \exp(ik_j z) + B_j \exp(-ik_j z) \quad (2.2)$$

where A_j and B_j are the forward and backward plane-wave amplitude coefficients and k_j is the free-particle momentum and is equal to

$$k_j = \sqrt{\frac{2m_j(E - V_j)}{\hbar^2}} \quad (2.3)$$

where E is the particle energy, V_j is the potential barrier energy in the j th layer, and \hbar is Planck's constant divided by 2π . Figure 2-2 illustrates a typical multiple layer structure considered. The bound state energies were found by first setting $A_0 = 0$ in the first layer,

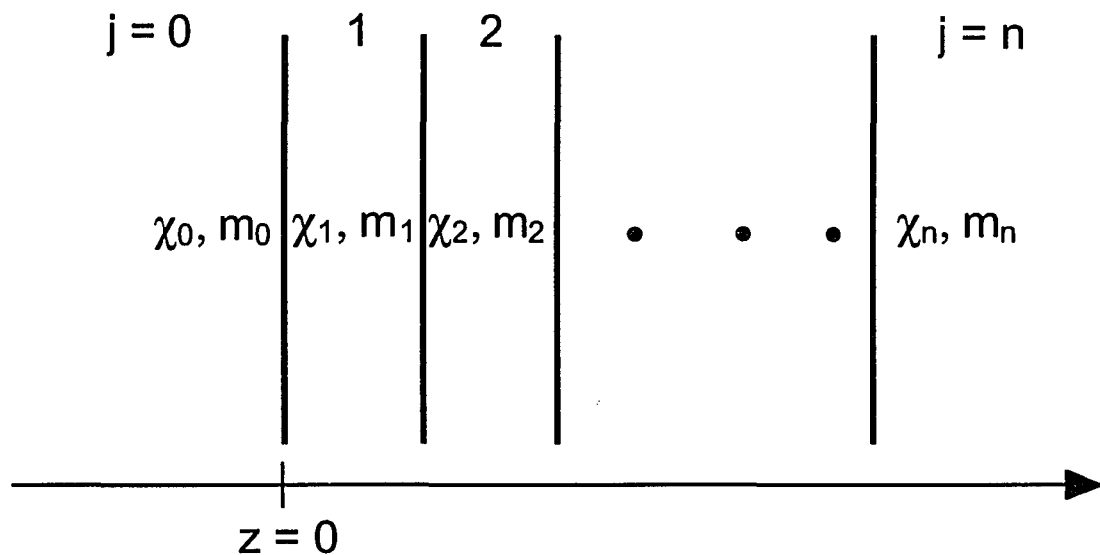


Figure 2-2 Schematic diagram of the multiple-layer model of a semiconductor quantum well structure.

assumed to be an infinitely thick finite-potential confining layer. The boundary condition that the wavefunction and its first derivative be zero at $z = -\infty$ is then automatically satisfied in this layer. The B_n coefficient in the last layer of the structure, also assumed to be an infinitely thick finite-potential confining layer, is then found as a function of energy by successively satisfying Eqs. 2.1a and 2.1b at each interface. Allowed bound states correspond to energies where $B_n = 0$. The wavefunction in the last layer is then a purely decaying exponential and satisfies the above boundary condition at $z = +\infty$. For the ADQW structures studied here are composed of five layers, i.e. $n = 4$.

The ADQW samples studied were composed of $\text{Ga}_{1-x}\text{In}_x\text{As}$ wells and $\text{Al}_{1-y}\text{In}_y\text{As}$ barriers lattice-matched to InP. For lattice-matched conditions, the fractional compositions must be $x = 0.53$ and $y = 0.52$. The properties of these two materials at room temperature are listed in Table 2.1.

Table 2.1 Room temperature ternary material data.[24]

	x	E_g (eV)	m_c^*/m_o	m_{hh}^*/m_o	m_{lh}^*/m_o
$\text{Ga}_{1-x}\text{In}_x\text{As}$	0.53	0.736	0.041	0.377	0.0516
$\text{Al}_{1-x}\text{In}_x\text{As}$	0.52	1.483	0.075	0.57	0.085

The conduction band offset for (Ga,In)As/(Al,In)As heterostructures is assumed to be 70% of the energy-gap difference and the valence band offset is assumed to be 30%.[38] The offset values used in the design of the ADQW samples are given in Table 2.2.

Table 2.2 Conduction and valence band offset data

ΔE_g (eV)	ΔE_c (eV)	ΔE_v (eV)
0.747	0.523	0.224

The parameters in Tables 2.1 and 2.2 were used to calculate the bound state energies and wavefunctions using the formalism described above. Figure 2-3 shows the dependence of the first two electron bound state energies on tunnel barrier width for an ADQW system with a 40 Å NW and 60 Å WW. The energy separation, ΔE , of the first

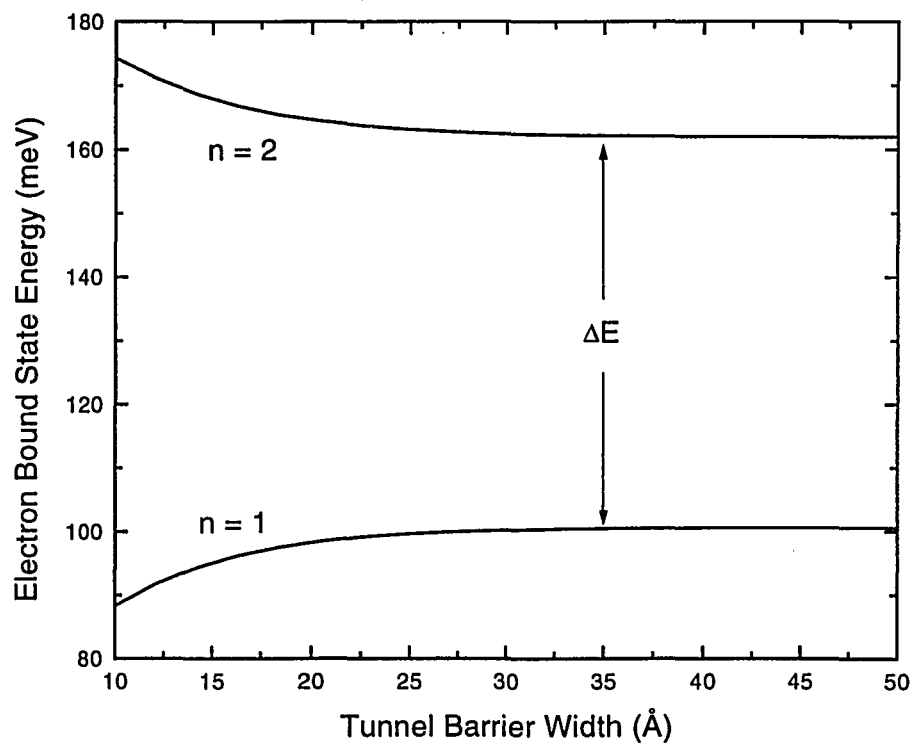


Figure 2-3 Tunnel barrier width dependence of the first two electron bound state energies of the 40/ L_b /60 (Ga,In)As/(Al,In)As ADQW structure.

two bound state energies is particularly important in the study of electron tunneling in ADQW structures. For fast tunneling to occur, i.e. tunneling times on picosecond time-scales, ΔE must be greater than the longitudinal optical (LO) phonon energy of the material.[10] In the case of $\text{Ga}_{0.47}\text{In}_{0.53}\text{As}$, the LO-phonon energy is 33.2 meV.[38] As clearly seen in Fig. 2-3, ΔE is greater than 33.2 meV for all the barrier widths considered. Hence, using the WW and NW widths of 60 and 40 Å, respectively, picosecond electron tunneling should be readily observable. Of course, for any electronic transition to occur, there must be significant overlap between the wavefunctions of the states involved in the transition.

The wavefunctions of the first and second electron bound states of the ADQW structure considered with a tunnel barrier width of 25 Å are shown in Fig. 2-4. The wavefunctions are delocalized over both the WW and NW, and as a result, there is significant overlap of the first and second bound state wavefunctions. The overlap of the $n = 1$ and $n = 2$ wavefunctions is a strong function of the barrier width and decreases with increasing tunnel barrier width. This result is consistent with what would be expected if the wells were considered independently of each other, i.e. at infinite separation the overlap would approach zero.

The heavy- and light-hole bound state energies and wavefunctions were calculated in a similar manner. It must be noted that since $\vec{k} \cdot \vec{p}$ mixing between electron subbands is negligible, the conduction band dispersion can be approximated by parabolic bands over

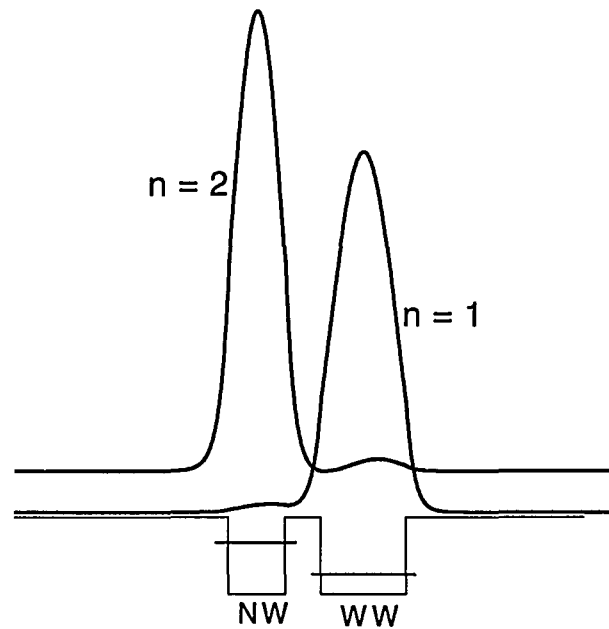


Figure 2-4 Probability densities, $\chi^*(z)\cdot\chi(z)$, of the first two electron bound states for the 40/25/60 (Ga,In)As/(Al,In)As ADQW structure. The distributions are offset for clarity.

the momentum and energy ranges of interest in this work. Additionally, the electron wavefunctions calculated above are valid for all energies within the corresponding subband. For holes, however, this is not the case. Since band-mixing and spin-coupling cannot be neglected in the valence band, the wavefunctions calculated using the above formalism are only valid at the Γ -point of momentum space, i.e. at zero in-plane momentum. The effects of band-mixing and spin-orbit coupling on the valence band

dispersion will be the topic of the next chapter. In any event, the Γ -point hole wavefunctions (both heavy and light) form a convenient basis in which to perform band-structure calculations.

The bound state energies of both the heavy-holes (solid lines) and light-holes (dashed lines) are shown in Fig. 2-5. It is interesting to note that the separation of the heavy-hole energies at the Γ -point is less than the LO-phonon energy. Thus, LO-phonon assisted tunneling is not allowed for heavy-holes which relax to the Γ -point. The Γ -point hole wavefunctions for the first two heavy-hole states (solid lines) and first two light-hole

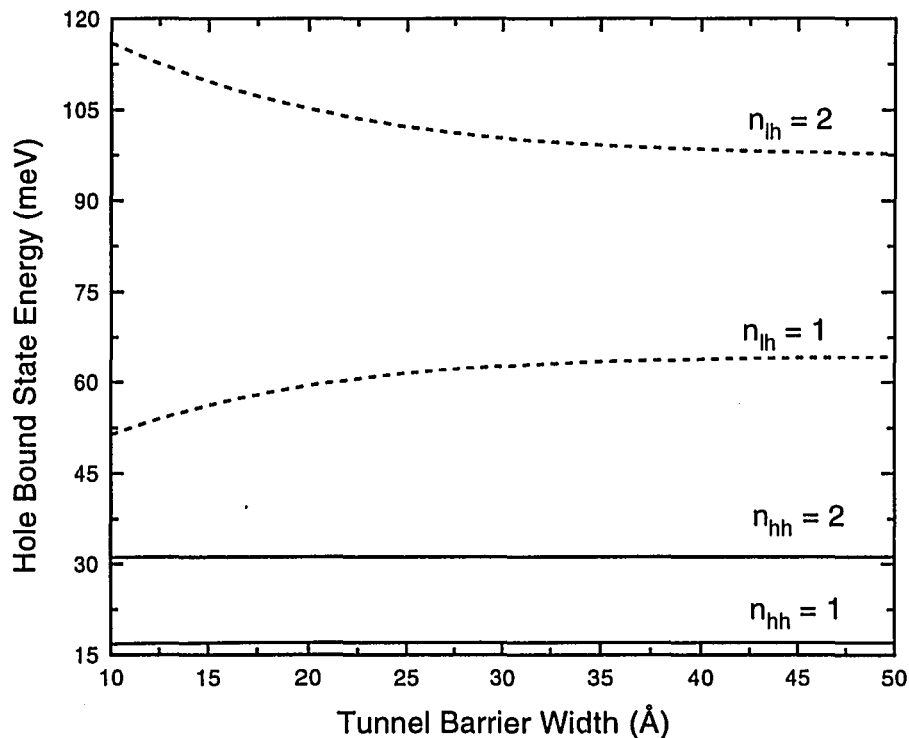


Figure 2-5 Tunnel barrier width dependence of the first two heavy-hole (solid lines) and light-hole (dashed lines) bound state energies of the 40/ L_b /60 (Ga,In)As/(Al,In)As ADQW structure.

states (dashed lines) are shown in Fig. 2-6. As expected, the heavy-hole wavefunctions are highly localized in their respective wells due to their high effective mass. The light-hole wavefunctions, on the other hand, are highly delocalized over both the WW and NW. The relatively low light-hole effective mass combined with the low valence band offset result in increased penetration of the wavefunctions into the adjacent wells. The processes of interest for ultrafast device applications are shown in Fig. 2-1. Since electrons and holes can be generated at the Γ -point of the NW in short times by a

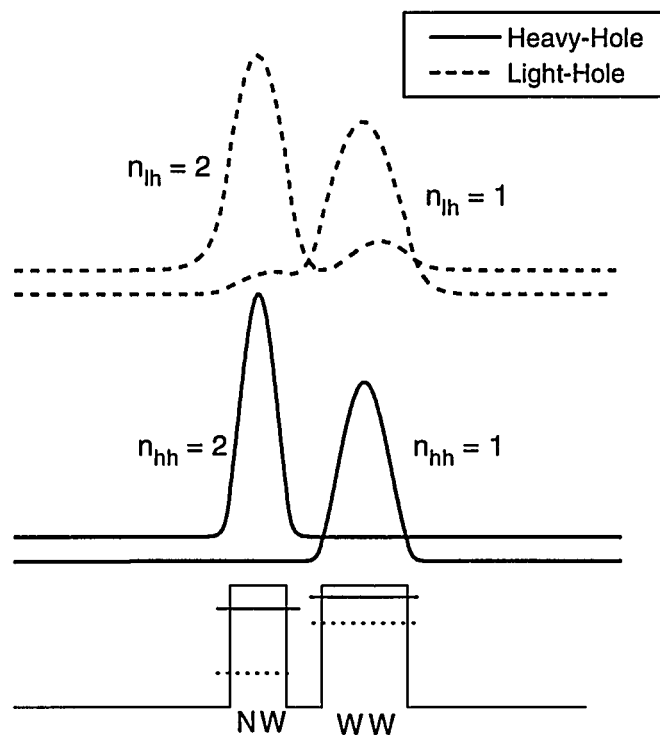


Figure 2-6 Probability densities, $\chi^*(z)\chi(z)$, of the first two heavy-hole (solid lines) and light-hole (dashed lines) bound states for the 40/25/60 (Ga,In)As/(Al,In)As ADQW structure. The distributions are offset for clarity.

femtosecond optical pulse, i.e. on the order of the pulse width, the remaining challenge is to remove the carriers from the NW on picosecond time-scales. As shown in Fig. 2-1 and discussed previously, electrons can transfer from the NW to WW on picosecond time scales through LO-phonon assisted tunneling. The holes also transfer from the NW to WW, but the experimentally observed hole tunneling times in GaAs/(Ga,Al)As ADQW structures have been shown to vary by two orders-of-magnitude depending on experimental and sample conditions.[15-17] As we shall see in the remainder of this chapter and the next, hole tunneling can even occur on time-scales which are shorter than electron tunneling times.

2.2 Sample fabrication and characterization

The formalism discussed above was used to design eight ADQW samples for this study. The ADQW samples consisted of the following structure: 40 Å Ga_{0.47}In_{0.53}As well/ L_b Å Al_{0.48}In_{0.52}As tunnel barrier/ 60 Å Ga_{0.47}In_{0.53}As well/ 100 Å Al_{0.48}In_{0.52}As barrier, where L_b is the thickness of the tunnel barrier. Different samples will be denoted as 40/L_b/60. These structures were grown by solid-source molecular beam epitaxy on semi-insulating (100) InP substrates. The eight samples were grown in two sets: the first set consisted of 60 period structures with tunnel barrier widths L_b = 100, 45, 37, and 27 Å, and the second set consisted of 30 period structures with tunnel barrier widths L_b =

70, 55, 37, and 27 Å. Samples from the first set will be denoted as 40/L_b/60¹. The optical quality of the samples was investigated using low temperature linear absorption and photoluminescence spectroscopy.

The linear absorption system was constructed in a standard transmissive geometry using a tungsten light source and 1/4-meter spectrometer. The samples were mounted in a liquid nitrogen cryostat and cooled to 77 K. The absorbance spectra for the eight ADQW samples are shown in Fig. 2-7. The first set of samples correspond to the bottom four spectra. As expected, samples 40/100/60 and 40/45/60 show two sets of heavy- and light-hole exciton absorption resonances corresponding to the NW and WW, respectively. Samples 40/37/60¹ and 40/27/60¹, however, do not show any excitonic features in their spectra. The quality of the samples was further investigated using low-temperature PL spectroscopy. The first two samples showed typical PL spectra corresponding to the radiative decay of free excitons. The last two samples, however, generated no PL signal from either the NW or WW. After further investigation of sample surface quality, it was determined that lattice-mismatch caused by flux-sag during the MBE growth series was responsible for the poor quality of samples 40/37/60¹ and 40/27/60¹. The problem was alleviated by calibrating the gallium and indium fluxes before the growth of each sample in a series.[39] The absorbance spectra for the second set of samples correspond to the top four spectra in Fig. 2-7. All four samples show well resolved heavy- and light-hole excitonic features, except sample 40/55/60 which lacked

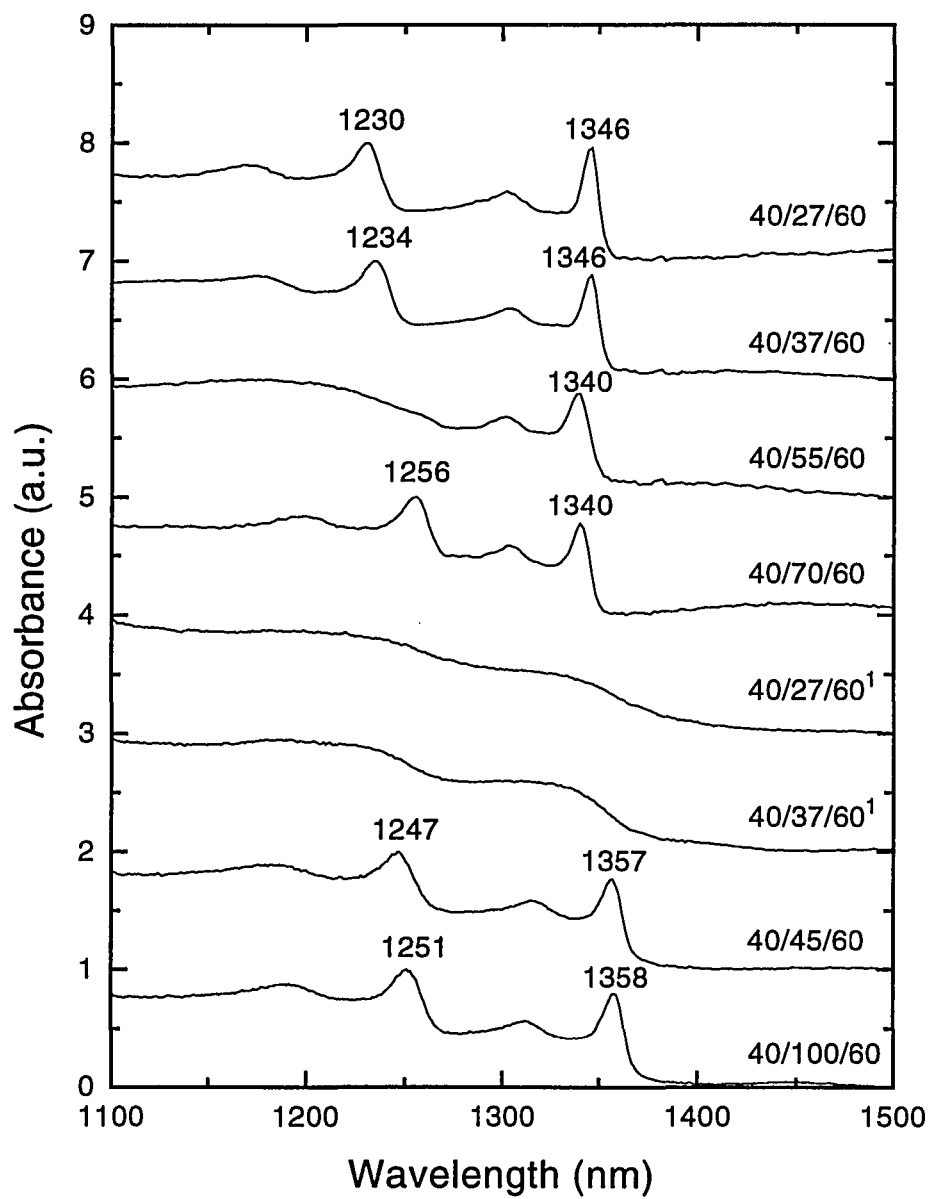


Figure 2-7 Measured 77 K absorbance spectra of the eight ADQW samples. The curves are offset for clarity.

any excitonic features from the NW. The gallium and indium fluxes were not calibrated before the growth of this sample (second in the series of four). As a result, the sample was of poor optical and mechanical quality.

Since the carrier dynamics are of interest, the samples were also characterized using time-integrated photoluminescence (PL) spectroscopy. The samples were again cooled to 77 K in a liquid nitrogen cryostat and pumped by a femtosecond Ti:Sapphire laser (described in the next section). The pump wavelength was 850 nm and was tuned to generate electrons and holes in the wells only (at low temperature the bandedge of the $\text{Al}_{0.48}\text{In}_{0.52}\text{As}$ barrier material occurs at a wavelength of 812 nm [38]). The pump-induced PL was dispersed using an 1/4-meter spectrometer. The pump beam was chopped by a mechanical chopper and the PL was detected using an InGaAs photodetector and lock-in amplifier. It is important to note that the pump laser used in these PL measurements is the same pump source used in the time-resolved measurements to follow. The PL spectra of samples 40/100/60, 40/70/60, 40/37/60, and 40/27/60 are shown in Fig. 2-8. The effects of tunneling are readily observed in these data. For sample 40/100/60, two PL peaks are clearly observed which corresponds to the radiative decay of free excitons in the NW (shorter wavelength peak) and WW (longer wavelength peak). For sample 40/70/60, the strength of the NW PL shows a considerable decrease in magnitude and indicates the steady-state electron population is decreasing as L_b decreases. The NW PL is absent for samples 40/37/60 and 40/27/60. If we assume that the magnitude of the PL peak

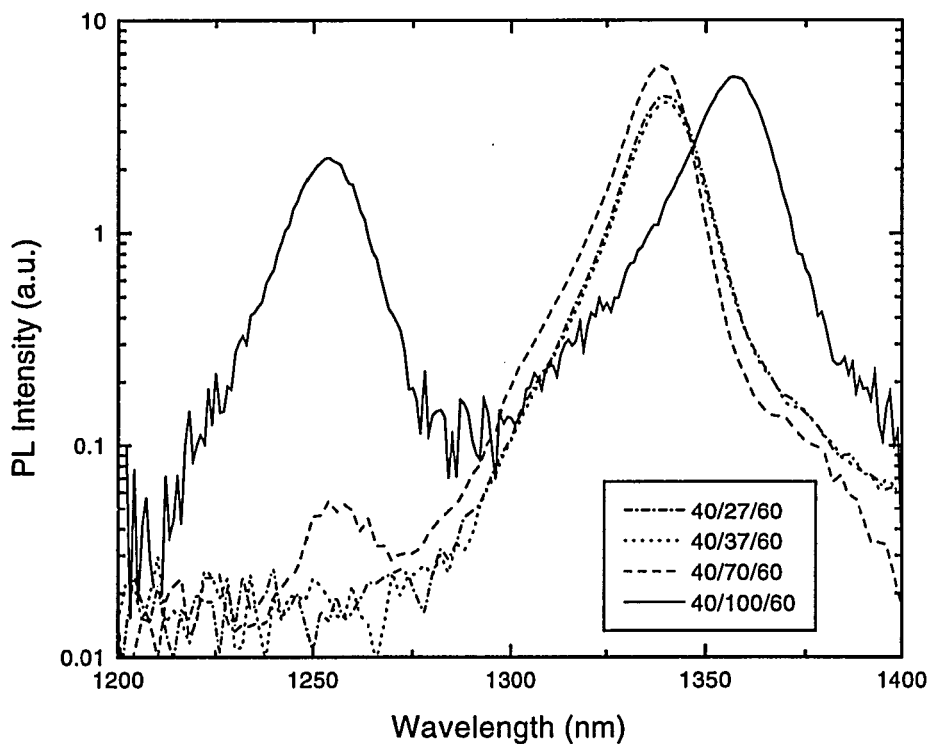


Figure 2-8 Measured 77 K PL spectra of ADQW samples 40/100/60, 40/70/60, 40/37/60, and 40/27/60.

is proportional to the carrier lifetime, we can obtain an estimate of the electron tunneling times. For conventional GaInAs/AlInAs multiple quantum wells, the carrier lifetime is approximately 5 ns.[3] From Fig. 2-8 it is clear that the NW PL strength for samples 40/27/60 and 40/37/60 is at least 250 times lower (below the noise floor of our measurement system) than the WW PL strength. Hence, we can assume that the electron lifetime in the NW is approximately 20 ps or less in these two samples. We believe that this suggests efficient tunneling of electrons from the NW to the WW.

2.3 Time-Resolved Measurement System

To study the carrier dynamics in the GaInAs/AlInAs ADQWs, subpicosecond time-resolution in the spectral region of 1250 nm is required. However, femtosecond lasers which operate at these wavelengths are still in the developmental stage. As a result, we have developed a novel non-degenerate, time-resolved pump/probe transmission system which utilizes a femtosecond Kerr lens modelocked Ti:Sapphire (TiS) laser and a continuous wave (CW) Cr:Forsterite laser.

A schematic of the TiS laser is shown in Fig. 2-9. The laser consists of a standard, astigmatically-compensated Z-cavity with an intra-cavity SF-14 prism pair to

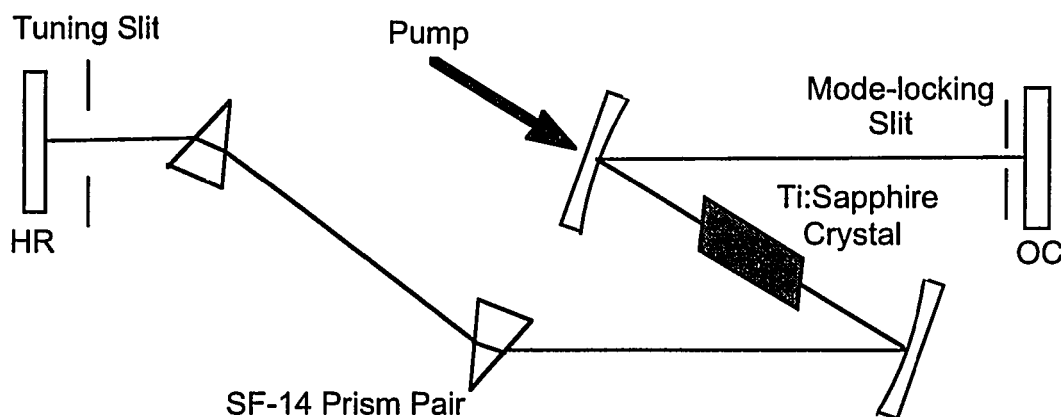


Figure 2-9 Schematic diagram of the femtosecond Ti:Sapphire laser used as the pump in the time-resolved pump/probe measurement system. OC: Output coupler, HR: High reflector.

compensate for intra-cavity group-velocity-dispersion. The TiS crystal, obtained from Union Carbide, Inc., was a 20 mm long Brewster cut cylinder with a 5 mm diameter. This laser was pumped by a 6 W continuous wave argon-ion laser (all lines) and produced as much as 450 mW of output power at 850 nm. The wavelength of the modelocked output was tuned using a wide slit placed near the high reflector. An additional slit was used near the output coupler to stabilize the Kerr lens modelocking. The laser routinely produced 100 fs, transform-limited pulses at a repetition rate of 90 MHz. The mode-locking was stable for hours unless interrupted by a strong mechanical perturbation.

The CW Chromium-doped Forsterite ($\text{Cr:Mg}_2\text{SiO}_4$) laser used in the measurement system is shown in Fig. 2-10.

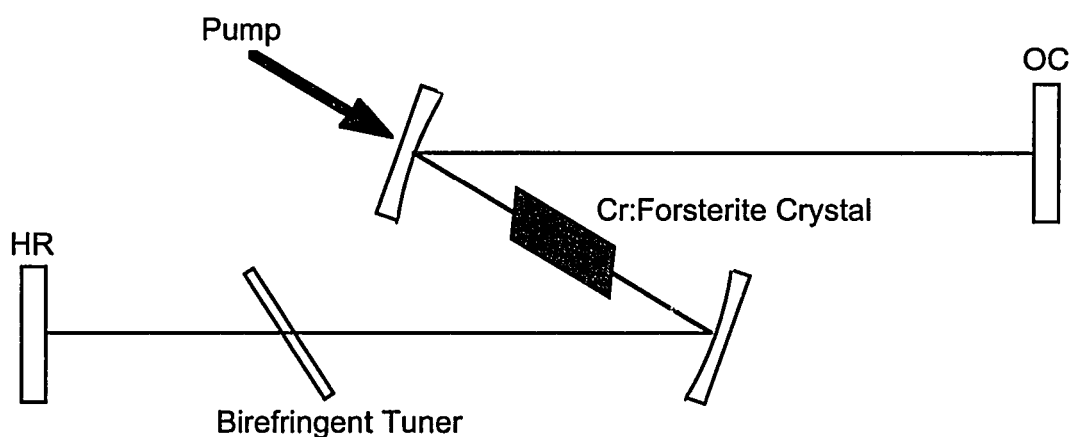


Figure 2-10 Schematic diagram of the CW Cr:Forsterite laser used as the probe in the time-resolved pump/probe measurement system.

This laser consists of a standard, astigmatically-compensated Z-cavity with an intra-cavity birefringent plate to provide wavelength tuning. The Cr:Forsterite crystal, obtained from Mitsui Mining and Smelting Co., was a Brewster-cut parallel-piped 10 mm long and $5 \times 5 \text{ mm}^2$ in cross-section. Since the Forsterite host crystal has a relatively low thermal conductivity, the laser crystal was clamped between brass plates and actively cooled to 3°C by a thermo-electric cooler. The crystal was pumped by as much as 8 W from a $1.064 \text{ }\mu\text{m}$ Nd:YAG laser and produced as much as 350 mW of output power at the peak in the tuning curve. The tuning range of the laser extends from 1210 to 1320 nm.

The experimental system used to measure the carrier dynamics utilized a novel time-resolved transmission/upconversion technique. In most previous studies of carrier dynamics in ADQWs time-resolved PL was utilized.[5-11] In time-resolved PL, the product $f_c(E_c, T_c)f_h(E_h, T_h)$ is measured, where $f_c(E_c, T_c)$ and $f_h(E_h, T_h)$ are the Fermi distributions of the electrons and holes, E_c and E_h are the electron and hole energies, and T_c and T_h are the electron and hole temperatures, respectively. Hence, if one type of carrier is absent the total PL signal is zero despite the existence of the other carrier. On the other hand, transmission techniques measure $1 - f_c(E_c, T_c) - f_h(E_h, T_h)$. Therefore, the dynamics of the individual carriers change the transmission signal independently.

A schematic diagram of the transmission/upconversion measurement system is shown in Fig. 2-11. In our approach, the 100 fs pulses at 850 nm from the KLM TiS laser were split using a half-wave plate/polarizing beamsplitter combination. One beam

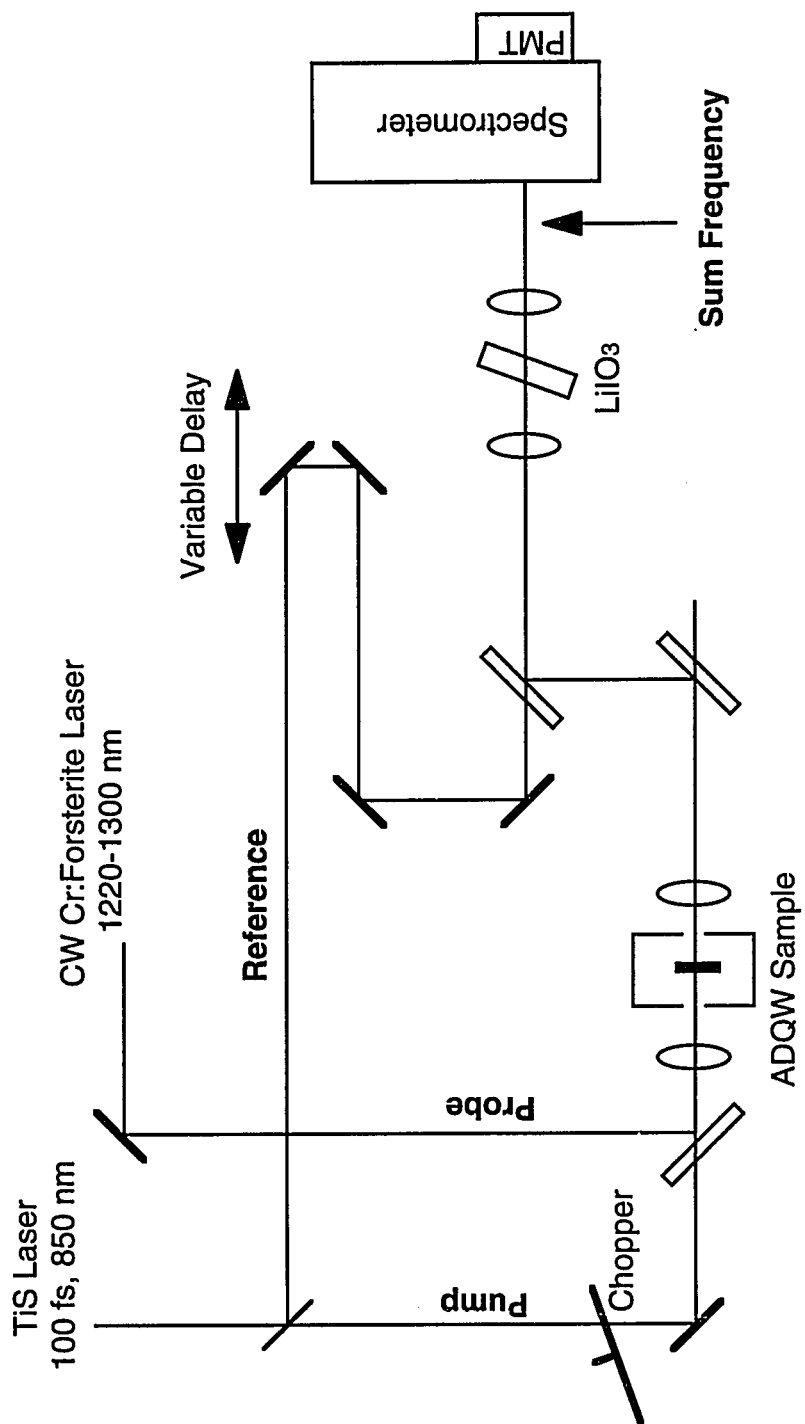


Figure 2-11 Schematic diagram of the upconversion pump/probe system.

was used to pump the samples and the other beam was used to provide reference pulses for the upconversion process. Both the pump and probe beams were colinearly incident on the ADQW samples. The transmitted probe was then colinearly combined with the reference pulses and then focused into a 2 mm thick LiIO_3 crystal. The nonlinear crystal was cut for type-I sum-frequency generation between the Ti:S reference laser and the Cr:Forsterite probe laser. The upconverted photons were then spectrally filtered by a 0.275 meter spectrometer (a 600 line/mm grating blazed at 500 nm was used) and detected by an uncooled photomultiplier tube. The pump was chopped to measure the pump-induced changes in the transmitted probe using lock-in detection.

The basic idea of how frequency mixing is used to obtain femtosecond time resolution is shown in Fig. 2-12. The reference pulse is delayed by the variable delay stage to overlap the pump-induced probe transmission changes of interest. Sum frequency photons are generated only during the time the reference pulse is present at the nonlinear crystal. As a result, sum-frequency mixing acts as a light gate and produces a signal proportional to the probe intensity present at the time of gating. The time evolution of the probe transmission changes can be obtained by varying the delay of the reference pulse at the crystal. Of course for the up-conversion process to be efficient, the condition for phase matching must be satisfied. The LiIO_3 crystal was cut with the optic-axis at an angle of 30° with respect to the crystal surface normal. To phase-match the pump and probe beams, the required angle is approximately 31.5° . This angle was

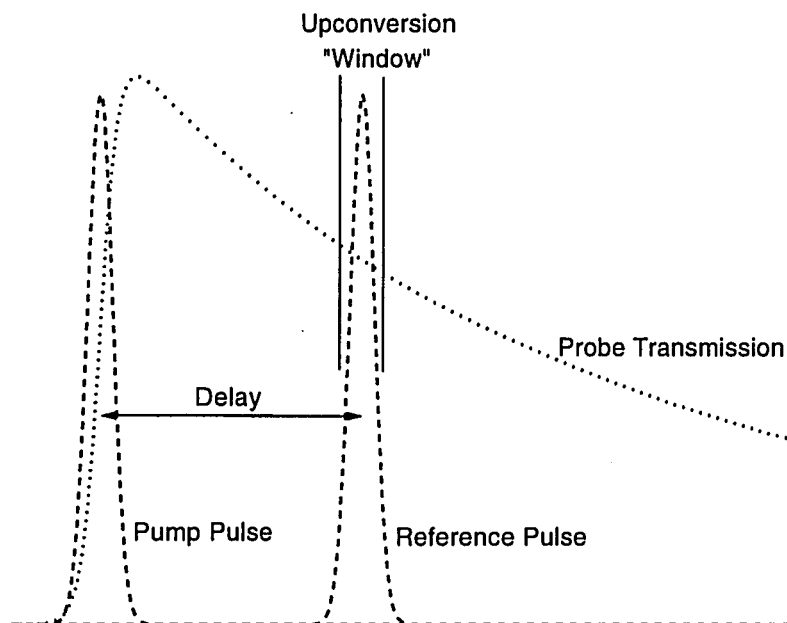


Figure 2-12 Schematic diagram of how sum-frequency generation is used to temporally resolve probe transmission changes.

experimentally achieved by angle tuning the crystal to maximize the observed sum-frequency signal.

The resolution of the system is limited by the width of the reference pulse in the absence of group-velocity-dispersion in the nonlinear crystal. In these experiments, however, the group velocity mismatch between the pump (850 nm) and the probe (1230 nm) is quite large for the 2 mm thick LiIO_3 crystal used. For type-I up-conversion ($\text{O} + \text{O} \rightarrow \text{E}$ where O and E refer to the ordinary and extraordinary waves, respectively), J.

Shah has developed the following expression for the broadening of the system response introduced by group velocity mismatch[40]

$$\Delta t(s) = L(\text{cm}) \left[\gamma_{\text{ref}}(\text{s/cm}) - \gamma_{\text{probe}}(\text{s/cm}) \right] \quad (2.4)$$

where γ_{ref} and γ_{probe} are given by

$$\gamma_{\text{ref}} = \frac{1}{c} \left[n_{\text{o,ref}} - \lambda_{\text{ref}} \left. \frac{\partial n_{\text{o,ref}}}{\partial \lambda} \right|_{\lambda=\lambda_{\text{ref}}} \right] \quad (2.5)$$

and

$$\gamma_{\text{probe}} = \frac{1}{c} \left[n_{\text{o,probe}} - \lambda_{\text{probe}} \left. \frac{\partial n_{\text{o,probe}}}{\partial \lambda} \right|_{\lambda=\lambda_{\text{probe}}} \right] \quad (2.6)$$

and L is the thickness of the LiIO_3 crystal used. In Eqs. 2.5 and 2.6, $n_{\text{o},i}$ is the wavelength dependent ordinary refractive index of LiIO_3 . Using the following dispersion relation for the ordinary refractive index of LiIO_3 given in Reference 40:

$$n_{\text{o}}^2(\lambda) = 3.40109 + \frac{0.0525}{\lambda^2 - 0.021865} \quad (2.7)$$

and reference and probe wavelengths of 0.85 and 1.23 μm , respectively, the system resolution due to the group velocity mismatch between the reference and probe was found to be 220 fs, approximately twice the reference pulse width.

For all of the time-resolved measurements discussed in this chapter, the ADQW samples were held at 77K in a liquid nitrogen cryostat. Figure 2-13 illustrates the carrier tunneling processes investigated using the non-degenerate pump and probe technique. The photon energy of the pump was tuned to generate carriers only in the wells, not in

the barriers, with most of the excess energy carried by the electrons. This avoids complications introduced by carrier capture when interpreting the experimental data. Finally, the Cr:Forsterite probe laser was tuned to the lowest energy, heavy-hole exciton absorption resonance of the NW for all measurements discussed. The dynamics of the carriers as they reach the Γ -point of the lowest electron and hole subbands in the NW are then monitored by measuring the temporal changes in the heavy-hole exciton absorption strength. It should be noted that there is an additional bound state ($n=3$) associated with the WW. Electron tunneling from this $n = 3$, WW state to the $n = 2$, NW state is also allowed. However, no tunneling from the WW to the NW should be observed since

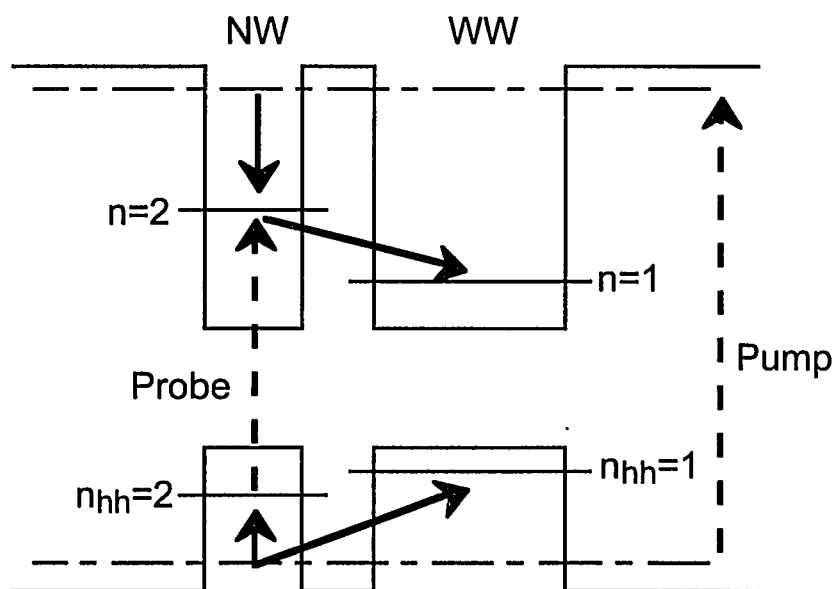


Figure 2-13 Illustration of the electron and hole tunneling processes investigated using the non-degenerate pump/probe system. The dashed lines represent optical transitions, and the solid lines represent transitions involved in the relaxation and tunneling of electrons and holes.

scattering to the $n = 1$, WW state dominates the electron relaxation process from the $n = 3$ level.

2.4 Experimental Results

The time-resolved differential transmission data, i.e. $[T(P)-T(P=0)]/T(P=0)$ where P is the pump intensity, for sample 40/27/60 is shown in Fig. 2-14 for carrier densities of 1.4×10^{11} , 5.6×10^{11} , 1.1×10^{12} , and $2.3 \times 10^{12} \text{ cm}^{-2}$. The carrier densities were estimated using the formula $(1-R)\alpha(\lambda_p)LT_pP_p/A_p\hbar\omega_p$, where $R = 0.3$ is the reflectance of the air-semiconductor interface, $\alpha(\lambda_p) = 1 \times 10^4 \text{ cm}^{-1}$ is the absorption coefficient at the pump wavelength, $T_p = 11 \text{ ns}$ is the pump pulse period, P_p is the pump average power, $A_p = 3.142 \times 10^{-6} \text{ cm}^2$ is the area of the pump spot on the sample, $\hbar\omega_p = 2.34 \times 10^{-19} \text{ J}$ is the pump photon energy, and L is the thickness of the quantum well system. The initial rise shows the relaxation of carriers to the Γ -point of the lowest energy NW subband. The subsequent decay is due to tunneling of carriers from the NW to the WW. There are two striking features in these data. The first is the fast and full recovery of the transmission at the lowest two carrier densities. At the lowest carrier density, the decay was fitted to a *single* exponential decay constant of 2.4 ps. The transmission fully recovers with a single time constant despite the fact that the probe wavelength was tuned to the heavy-hole exciton absorption peak of the NW.

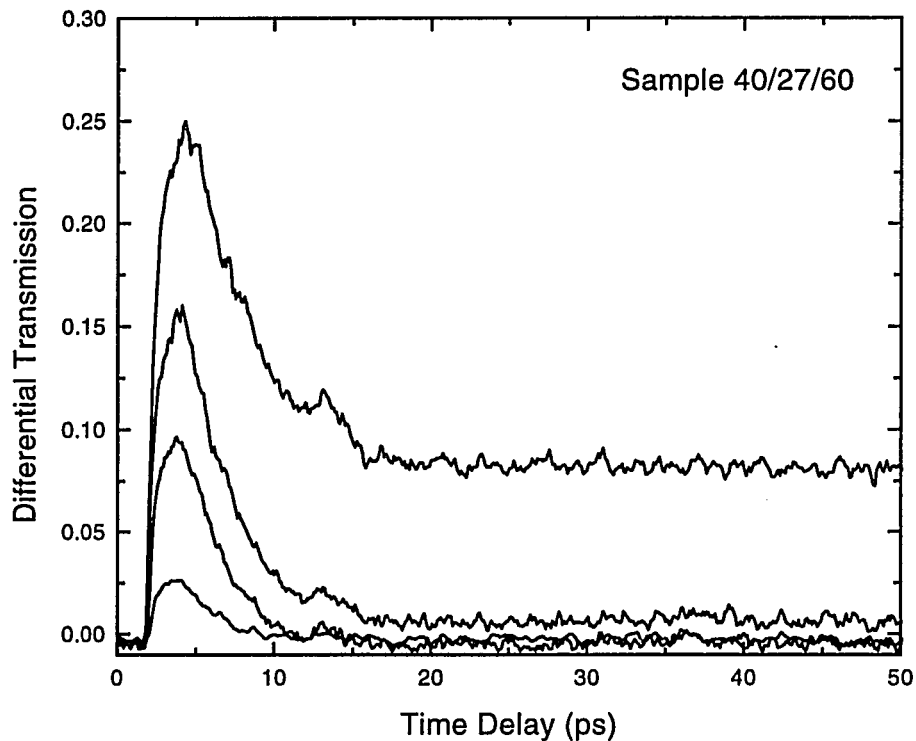


Figure 2-14 Time-resolved differential transmission data for sample 40/27/60 at carrier densities of 1.4×10^{11} , 5.6×10^{11} , 1.1×10^{12} , and 2.3×10^{12} cm^{-2} , respectively. The probe wavelength was 1230 nm.

As mentioned previously, fast hole tunneling was not expected since the energy separation of the first two heavy-hole bound states is less than the LO-phonon energy. However, since the upconversion technique measures $1 - f_c(E_c, T_c) - f_h(E_h, T_h)$, full recovery indicates the absence of both electron and hole populations. The second striking feature is the appearance of a long-lasting component at high carrier densities. To verify that the fast component of the decay was associated with the tunneling of carriers from the NW to the WW, the same measurements were performed using sample 40/37/60.

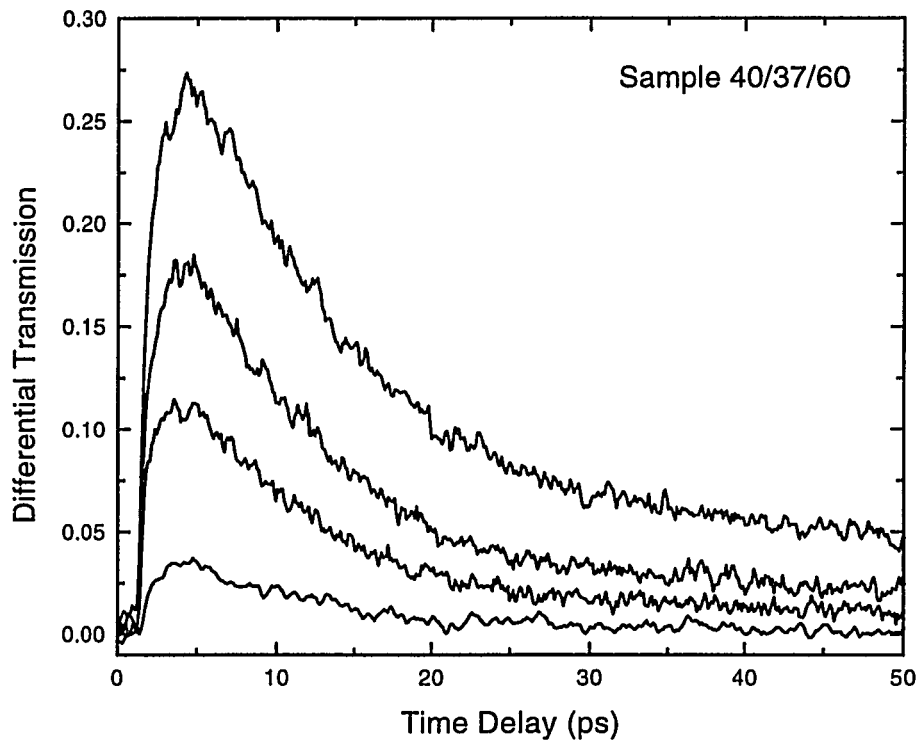


Figure 2-15 Time-resolved differential transmission data for sample 40/37/60 at carrier densities of 1.4×10^{11} , 5.6×10^{11} , 1.1×10^{12} , and 2.3×10^{12} cm^{-2} , respectively. The probe wavelength was 1234 nm.

The measured data are shown in Fig. 2-15. The time-constant associated with the decay at low carrier density was 11.5 ps. The results are consistent with tunneling phenomena, *i.e.* for a thicker barrier the time-constant of the fast component becomes longer. Sample 40/100/60 showed no recovery over our delay range of 50 ps as shown Fig. 2-16, consistent with an essentially decoupled pair of wells.

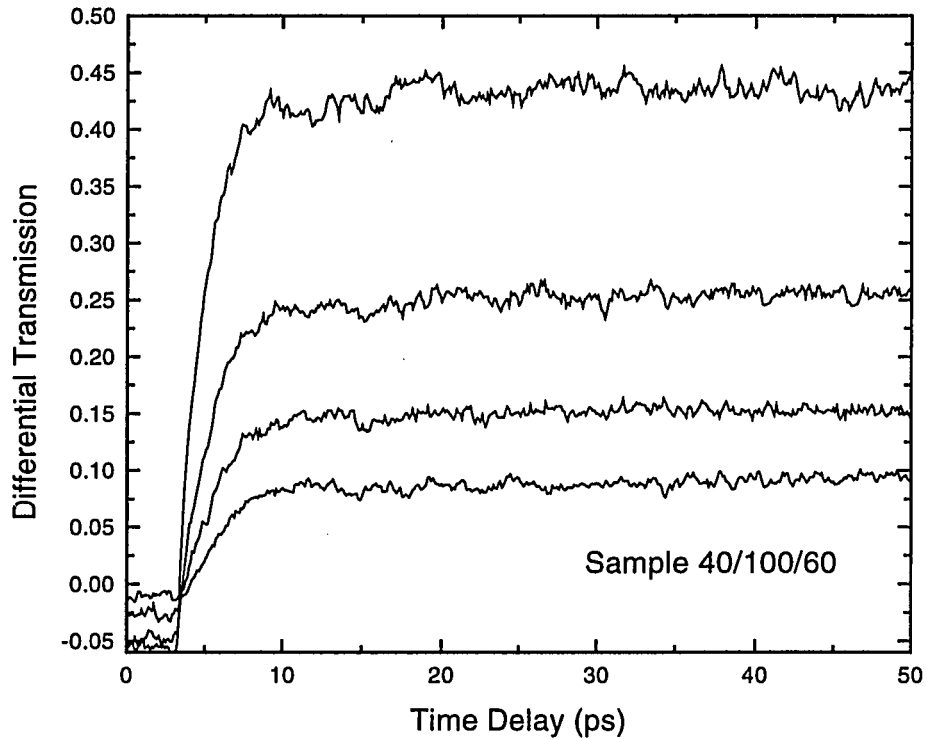


Figure 2-16 Time-resolved differential transmission data for sample 40/100/60 at carrier densities of 1.4×10^{11} , 5.6×10^{11} , 1.1×10^{12} , and 2.3×10^{12} cm^{-2} , respectively. The probe wavelength was 1251 nm.

2.5 Discussion

To understand the dynamics observed in this work, we considered the electron behavior independently of the holes. Since the inter-well dynamics are not significantly affected by excitonic effects [12], we have neglected the coulomb attraction between electrons and holes in the following tunneling rate calculations. Additionally, at the carrier

densities considered, the induced excitonic absorption charges are produced primarily by free-particle, phase-space effects.[3] It has been discussed previously that the inter-well electron dynamics in ADQW systems are dominated by LO-phonon emission when the energy separation between the first two electron subbands is greater than the LO-phonon energy.

To treat the electron/LO-phonon interaction in quantum confined structures we use the following form of Fermi's Golden Rule (see Appendix A for a derivation of this expression):

$$\frac{1}{\tau} = \frac{S}{\hbar} \left[\frac{k'}{d\varepsilon_{k'}/dk'} \right] \frac{1}{2\pi} \int_0^{2\pi} d\theta \left| \langle \varphi_{k'}(\vec{r}) | V_{LO}(\vec{r}, \vec{q}) | \varphi_k(\vec{r}) \rangle \right|^2 \quad (2.8)$$

and assume the following electron/LO-phonon interaction potential:

$$V_{LO}(\vec{r}, \vec{q}) = C(\vec{q}) a^+ \exp(-i\vec{q} \cdot \vec{r}) + C^*(\vec{q}) a^- \exp(+i\vec{q} \cdot \vec{r}) \quad (2.9)$$

where a^+ and a^- are the creation and annihilation operators for a phonon in the mode \vec{q} , and $|C(\vec{q})|^2$ in the Fröhlich coupling constant and is defined as

$$|C(\vec{q})|^2 = \frac{2\pi e^2 \hbar \omega_{LO}}{\Omega q^2} \left(\frac{1}{\kappa_{\infty}} - \frac{1}{\kappa_0} \right) \quad (2.10)$$

where ω_{LO} is the angular frequency of the LO-phonon, e is the electronic charge, κ_0 and κ_{∞} are the static and dynamic dielectric constants of the crystal, respectively, and $\Omega = SL$ is the volume of the sample. Equation 2.9 treats the phonon as a bulk mode and neglects any effects of the heterostructure on the phonon dispersion. Equations 2.8 - 2.10 were

used to derive (see Appendix B) the following expression for LO-phonon assisted electron tunneling:

$$\left(\frac{1}{\tau}\right)_{\text{LO}} = \frac{e^2 \omega_{\text{LO}}}{\kappa_p} \left\{ k' / |d\epsilon_{k'} / dk'| \right\} \frac{1}{2\pi} \int_0^{2\pi} [(N+1)I(Q^-) + NI(Q^+)] d\theta \quad (2.11)$$

where

$$I(Q^\pm) = \frac{\pi}{Q^\pm} \iint \chi_k(z) \chi_{k'}(z) \exp(-Q^\pm |z - z'|) \chi_k(z') \chi_{k'}(z') dz' dz \quad (2.12)$$

In Eq. 2.12, Q^\pm is the magnitude of the in-plane momentum change, $\kappa_p^{-1} = \kappa_\infty^{-1} - \kappa_0^{-1}$, and $\chi_k(z)$ and $\chi_{k'}(z)$ are the initial and final state electron envelope wavefunctions (see Fig. 2-4), respectively. The effects of bandfilling on the electron tunneling times have been included by replacing the ordinary density of final states in the wide well, m^*/\hbar^2 , by $[1 - f_{\text{ww}}(E, T_c)] m^*/\hbar^2$ where $f_{\text{ww}}(E_c, T_c)$ is the Fermi distribution of electrons in the wide well, E_c is the electron energy relative to the bottom of the bulk GaInAs conduction band, and T_c is the electron temperature. Figure 2-17 illustrates the conduction band processes considered. At a sample temperature of 77 K the phonon occupation number (Eq. B.24), N , is equal to 0.0067. As a result, the tunneling process will be dominated by spontaneous LO-phonon emission. A further simplification is made by only considering initial electron states with zero in-plane momentum, i.e. $k = 0$.

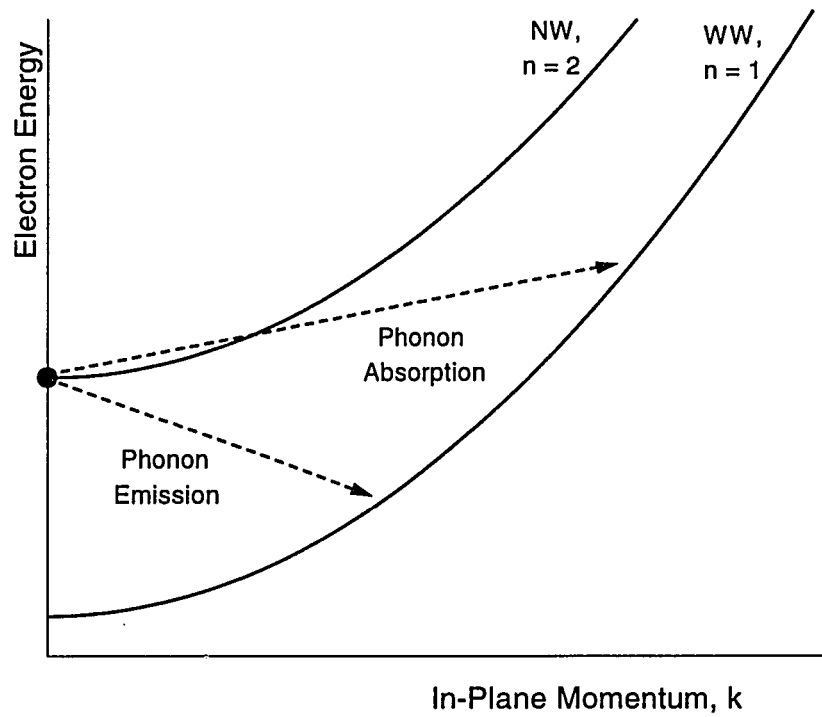


Figure 2-17 Schematic diagram of the phonon assisted electron processes considered in the calculation of the electron tunneling times.

The electron tunneling rate becomes

$$\left(\frac{1}{\tau}\right)_{LO} = \frac{m^* e^2 \omega_{LO}}{\kappa_p \hbar^2} [1 - f_{ww}(E_e, T_e)] I(Q) \quad (2.13)$$

The parameters used in the calculation of the LO-phonon assisted tunneling times are listed in Table 2.3.

Table 2.3 Parameters used in the LO-phonon assisted electron tunneling time calculations. Material parameters are for $\text{Ga}_{0.47}\text{In}_{0.53}\text{As}$.

ω_{LO} (1/s)	e (esu)	m_0 (g)	\hbar (erg-s)	κ_0	κ_∞
5.0417×10^{13}	4.803×10^{-10}	9.11×10^{-28}	1.055×10^{-27}	13.87	11.35

The ADQW samples were designed such that the energy separation between the lowest energy levels in the WW and NW was approximately 61 meV as shown in Fig. 2-2 (the separation increased slightly as the barrier width was decreased). A large separation between the levels was chosen for two reasons: first, for energy separations less than 50 meV the calculated tunneling times were sub-picosecond making the pump induced transmission changes difficult to observe experimentally; and second, the separation between the levels is far from being in resonance with the LO-phonon energy hence avoiding any significant change in the electron tunneling time due to space-charge induced level shifts. The affect of alloy scattering on electron tunneling was also considered theoretically, however, the calculated tunneling times were two orders of magnitude longer than the LO-phonon assisted tunneling times.

The calculated barrier width dependence of the electron tunneling times at low carrier densities is shown in Fig. 2-18. Also shown in the figure are the measured low-density time-constants for samples 40/27/60 and 40/37/60. The measured times are in good agreement with the calculated LO-phonon assisted electron tunneling times. Thus, the transmission *fully recovers* with a time constant equal to the electron tunneling time.

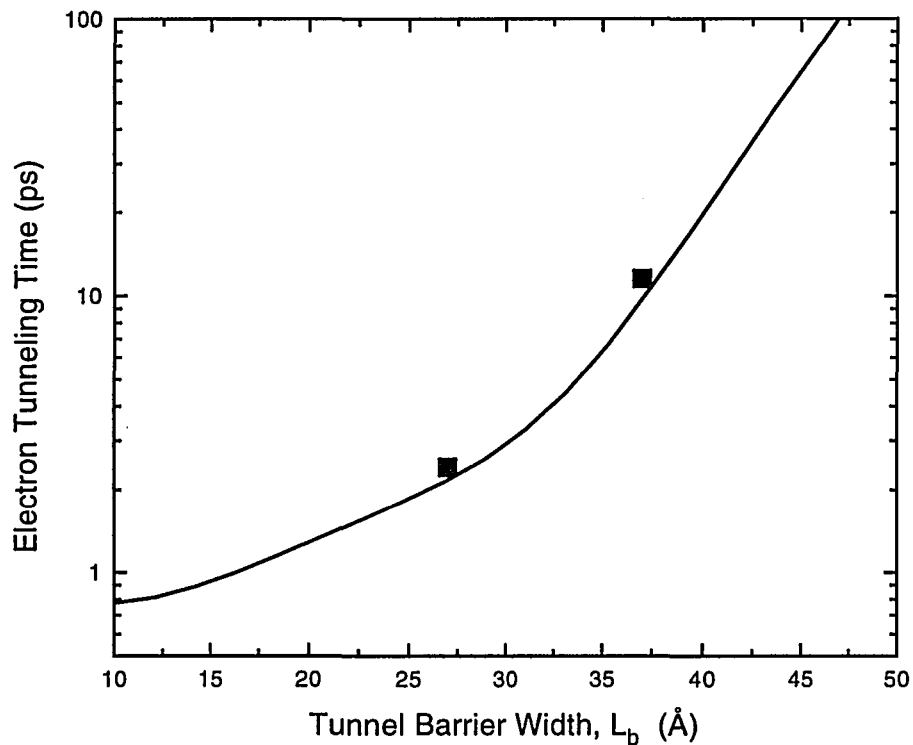


Figure 2-18 Tunnel barrier width dependence of the fast recovery component at low carrier densities (squares) and the calculated electron tunneling time (solid line).

To verify that the fast decay component in the data is associated with electron tunneling, the carrier density dependence of the fast component time-constant was measured. Figure 2-19 shows the measured carrier density dependence of the fast recovery component for sample 40/27/60 and the calculated carrier density dependence of the electron tunneling time (solid line). The tunneling times increase as the carrier density is increased, consistent with bandfilling in the WW acting as a blocking mechanism to tunneling electrons. To obtain the fit to the experimental data, only the electron temperature in Eq. 2.13 was adjusted. The theoretical carrier densities used in the model

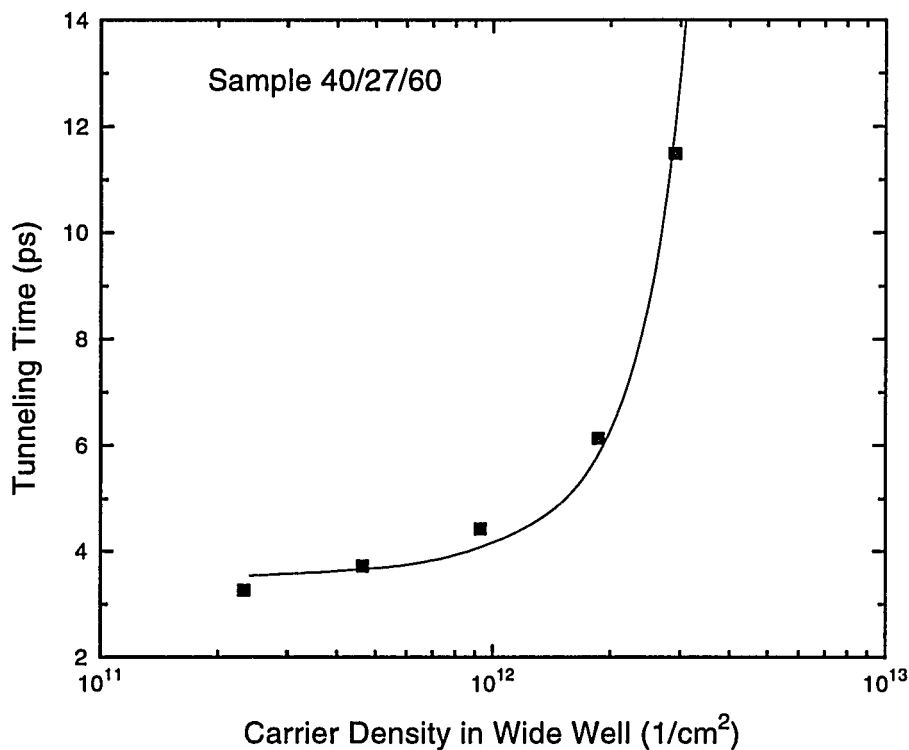


Figure 2-19 Carrier density dependence of the fast recovery component for sample 40/27/60 (squares) and the calculated electron tunneling time (solid line).

were multiplied by a factor of four with respect to the experimental carrier densities to fit the measured tunneling times. In all likelihood, the carrier densities derived from the experimental conditions are over-estimated.[41] It has been shown previously that in undoped samples, photogenerated carriers cool to the lattice temperature on timescales of 100 to 200 ps.[11] Hence, the electron temperature was assumed to be constant over the time-scales considered here. The calculated tunneling times fit the measured data best using a carrier temperature of 150 K, indicating that the electron distributions are still hot during the tunneling process.

2.6 Summary of Experimental Results

The good agreement between the observed fast recovery and the calculated electron tunneling times provides strong evidence that at low carrier densities the observed transmission changes are due to only electrons arriving at the Γ -point. In previous transmission studies of carrier dynamics in GaAs/(Ga,Al)As ADQWs, a long lasting component was observed for all carrier densities considered and was attributed to the relatively long time heavy-holes spend in the NW due to their highly localized wavefunctions at the Γ -point.[19,20] In both of these reports, however, the experiments used degenerate or nearly degenerate pump/probe techniques. Hence, holes are generated at or near the Γ -point of the lowest heavy-hole subband of the NW. Our experimental technique is highly non-degenerate, and as a result, carriers are generated in the bands of interest with significant excess energy and in-plane momenta by the pump pulse, i.e. at $k \approx 0.05 \text{ \AA}^{-1}$. Thus, it is possible for holes generated in the NW to tunnel to the WW before reaching the Γ -point of the NW. To gain further understanding of hole dynamics under the experimental conditions considered in this chapter, the next chapter presents a detailed theoretical investigation of hole tunneling in ADQW structures. A discussion of the high carrier density time-resolved data will be presented in the next chapter, since they depend on both electron and hole tunneling.

CHAPTER 3

ULTRAFAST HOLE TUNNELING THEORY

Hole tunneling in asymmetric double quantum wells (ADQWs) has been the topic of considerable research interest recently. In this chapter we present a theoretical study of hole tunneling in ternary ADQWs. In particular, the experimental results presented in Chapter 2 indicate that holes generated with nonzero in-plane momenta can tunnel as fast or faster than electrons. Hence, the hole dynamics investigated in this chapter are concerned with the inter-well hole transfer at momentum values away from the Brillouin zone center. Previous studies have indicated that efficient hole tunneling between the narrow well (NW) and wide well (WW) occurs when there are resonances between hole subbands due to the presence of an applied field [14,16,17] or due to valence band mixing between NW and WW subbands.[18] The results presented here indicate, however, that at low carrier densities subpicosecond hole tunneling can occur even in the absence of resonances between hole states.

3.1 Valence Band Structure Calculations

In all III-V materials the top of the valence band occurs at the center of the Brillouin zone, i.e. the Γ -point. Since the three valence band edges originate from bonding

p orbitals, the total angular momentum $|\bar{J}| = |\bar{L} + \bar{S}|$ is either $3/2$ or $1/2$, where $|\bar{L}| = 1$ and $|\bar{S}| = 1/2$ are the orbital and spin angular momenta, respectively. In the absence of spin-orbit coupling, the three valence bands are degenerate at the zone center. However, spin-orbit coupling lifts this degeneracy at the Γ -point giving rise to a quadruplet which corresponds to $\bar{J} = 3/2$ and a doublet which corresponds to $\bar{J} = 1/2$ (at the Γ -point the $\bar{J} = 3/2$ bands are four-fold degenerate corresponding to $J_z = 3/2, 1/2, -1/2,$ and $-3/2$, where J_z is the projection of \bar{J} on the z -axis, and the $\bar{J} = 1/2$ bands are two-fold degenerate corresponding to $J_z = 1/2$ and $-1/2$). In bulk III-V materials, the $\bar{J} = 3/2$ bands form the heavy-hole ($J_z = \pm 3/2$) and light-hole ($J_z = \pm 1/2$) bands and the $\bar{J} = 1/2$ bands form the split-off band ($J_z = \pm 1/2$). For an accurate description of the valence band structure near the Γ -point, the Kane model can be employed.[42] This model requires the diagonalization of an 8×8 matrix which includes $\bar{k} \cdot \bar{p}$ coupling within the Γ_6 (conduction band) Γ_7 (split-off band) Γ_8 (heavy- and light-hole bands) subspace.

For the ADQW band structure calculations presented in this chapter, we assume that the energy gap and split-off energy at the Γ -point of the bulk well material are large enough to approximate the Γ_8 dispersion by parabolic bands. The 4×4 Luttinger Hamiltonian can then be utilized where the effect of all remote bands, including the conduction and split-off bands, is treated using perturbation theory and is accounted for by the Luttinger parameters.[43,44]

The 4x4 valence band Hamiltonian used to calculate the heavy- and light-hole dispersion in semiconductor heterostructures is given as[42]

$$H_{\Gamma_8} = \begin{matrix} \langle 3/2, 3/2 | \\ \langle 3/2, -1/2 | \\ \langle 3/2, 1/2 | \\ \langle 3/2, -3/2 | \end{matrix} \begin{bmatrix} H_{hh} & c & b & 0 \\ c^* & H_{lh} & 0 & -b \\ b^* & 0 & H_{lh} & c \\ 0 & -b^* & c^* & H_{hh} \end{bmatrix} \quad (3.1)$$

where

$$H_{hh} = -\frac{1}{2m_0} p_z (\gamma_1 - 2\gamma_2) p_z + V_p(z) - \frac{\hbar^2 k^2}{2m_0} (\gamma_1 + \gamma_2) \quad (3.2)$$

$$H_{lh} = -\frac{1}{2m_0} p_z (\gamma_1 + 2\gamma_2) p_z + V_p(z) - \frac{\hbar^2 k^2}{2m_0} (\gamma_1 - \gamma_2) \quad (3.3)$$

$$c(\vec{k}) = \frac{\hbar^2}{m_0} \frac{\sqrt{3}}{2} [\gamma_2 (k_x^2 - k_y^2) - 2i\gamma_3 k_x k_y] \quad (3.4)$$

$$b(\vec{k}, pz) = \frac{\sqrt{3}}{2} \frac{\hbar}{m_0} (k_x - ik_y) (\gamma_3 p_z + p_z \gamma_3) \quad (3.5)$$

In Eqs. 3.2 - 3.5 the γ 's are the Luttinger parameters, p_z is the momentum operator in the z-direction, $V_p(z)$ is the potential distribution in the z-direction, and $\vec{k} = k_x \hat{x} + k_y \hat{y}$ is the in-plane wavevector. To simplify the band structure calculations we assume the in-plane motion is isotropic and make the axial approximation

$$\gamma_2 = \gamma_3 \rightarrow \frac{(\gamma_2 + \gamma_3)}{2} \equiv \bar{\gamma} \quad (3.6)$$

With Eq. 3.6 in mind, we assume $k_x = 0$ and $k_y = k$, thus Eqs. 3.2 - 3.5 become

$$H_{hh} = -\frac{\hbar^2}{2m_0}(\gamma_1 - 2\bar{\gamma})\frac{\partial^2}{\partial z^2} + V_p(z) - \frac{\hbar^2 k^2}{2m_0}(\gamma_1 + \bar{\gamma}) \equiv H_{hh}^0 - \frac{\hbar^2 k^2}{2m_0}(\gamma_1 + \bar{\gamma}) \quad (3.7)$$

$$H_{lh} = -\frac{\hbar^2}{2m_0}(\gamma_1 + 2\bar{\gamma})\frac{\partial^2}{\partial z^2} + V_p(z) - \frac{\hbar^2 k^2}{2m_0}(\gamma_1 - \bar{\gamma}) \equiv H_{lh}^0 - \frac{\hbar^2 k^2}{2m_0}(\gamma_1 - \bar{\gamma}) \quad (3.8)$$

$$c(k) = -\frac{\hbar^2}{m_0} \frac{\sqrt{3}}{2} \bar{\gamma} k^2 \quad (3.9)$$

$$b(k) = -\frac{\hbar}{m_0} \frac{\sqrt{3}}{2} \bar{\gamma} k \frac{\partial}{\partial z} \quad (3.10)$$

Equations 3.7 and 3.8 are the conventional Hamiltonians for the motion of the heavy- and light-holes in the absence of band-mixing and spin-orbit coupling and contain the so-called mass-reversal effect for the valence subbands, namely the $J_z = \pm 3/2$ ($\pm 1/2$) states are heavy (light) for the z motion but light (heavy) for the in-plane motion. It is interesting to note that in the diagonal approximation, i.e the $b(k)$ and $c(k)$ terms are zero, the $J_z = \pm 3/2$ and $J_z = \pm 1/2$ subbands should cross. However, such crossings are suppressed by the $b(k)$ and $c(k)$ terms and replaced by anticrossings.

To find the valence band dispersion the following eigenvalue equation must be solved

$$H_{\Gamma_8} |\bar{\Psi}\rangle = E |\bar{\Psi}\rangle \quad (3.11)$$

To simplify the solution of Eq. 3.11 the Hamiltonian H_{Γ_8} was written as

$$H_{\Gamma_8} = H^0 + W(k) \quad (3.12)$$

where

$$H^o = \begin{bmatrix} H_{hh}^o & 0 & 0 & 0 \\ 0 & H_{lh}^o & 0 & 0 \\ 0 & 0 & H_{lh}^o & 0 \\ 0 & 0 & 0 & H_{hh}^o \end{bmatrix} \quad (3.13)$$

and

$$W(k) = \begin{bmatrix} -\frac{\hbar^2 k^2}{2m_o}(\gamma_1 + \bar{\gamma}) & c & b & 0 \\ c & -\frac{\hbar^2 k^2}{2m_o}(\gamma_1 - \bar{\gamma}) & 0 & -b \\ b^* & 0 & -\frac{\hbar^2 k^2}{2m_o}(\gamma_1 - \bar{\gamma}) & c \\ 0 & -b^* & c & -\frac{\hbar^2 k^2}{2m_o}(\gamma_1 + \bar{\gamma}) \end{bmatrix} \quad (3.14)$$

The wavefunction $|\bar{\Psi}\rangle$ is a four component vector given by

$$|\bar{\Psi}\rangle = \begin{pmatrix} \Psi_h^+ \\ \Psi_l^- \\ \Psi_l^+ \\ \Psi_h^- \end{pmatrix} \quad (3.15)$$

where +/- denote spin-up or spin-down, and the subscripts h and l denote heavy- and light-hole components, respectively. With these definitions the following eigenvalue equation can be constructed

$$[H^o + W(k)]|\bar{\Psi}\rangle = EI|\bar{\Psi}\rangle \quad (3.16)$$

where I is the 4x4 identity matrix. Since $[J_z, H^o] = 0$, we expand the components of $|\bar{\Psi}\rangle$ in an eigenbasis of H^o parallel to the growth axis, i.e. the $k = 0$ bound state heavy- and light-hole wavefunctions. These wavefunctions form an orthonormal basis and are easily

found using the transfer matrix formalism discussed in Chapter 2. The vector given by Eq. 3.15 becomes

$$|\bar{\Psi}\rangle = \begin{pmatrix} \sum_{m=1}^M \alpha_m^+ \xi_m(z) \\ \sum_{n=1}^N \beta_n^- \varphi_n(z) \\ \sum_{n=1}^N \beta_n^+ \varphi_n(z) \\ \sum_{m=1}^M \alpha_m^- \xi_m(z) \end{pmatrix} \quad (3.17)$$

where

$\xi_m(z)$, $E_{hm}^0 \rightarrow M$ bound heavy-hole states

$\varphi_n(z)$, $E_{ln}^0 \rightarrow N$ bound light-hole states

and α_m^\pm and β_n^\pm are the corresponding expansion coefficients, respectively. Rearranging

Eq. 3.16 results in the following equation

$$(E^0 - IE)|\bar{\Psi}\rangle + W(k)|\bar{\Psi}\rangle = 0 \quad (3.18)$$

where it has been noted that $H^0|\bar{\Psi}\rangle = E^0|\bar{\Psi}\rangle$ and is equal to

$$E^0|\bar{\Psi}\rangle = \begin{bmatrix} \alpha_1^+ E_{h1}^0 \xi_1(z) + \dots & 0 & 0 & 0 \\ +\alpha_M^+ E_{hM}^0 \xi_M(z) & \beta_1^- E_{l1}^0 \varphi_1(z) + \dots & 0 & 0 \\ 0 & +\beta_N^- E_{lN}^0 \varphi_N(z) & & \\ 0 & 0 & \beta_1^+ E_{l1}^0 \varphi_1(z) + \dots & 0 \\ & & +\beta_N^+ E_{lN}^0 \varphi_N(z) & \\ 0 & 0 & 0 & \alpha_1^- E_{h1}^0 \xi_1(z) + \dots \\ & & & +\alpha_M^- E_{hM}^0 \xi_M(z) \end{bmatrix}$$

Equation 3.18 results in a four component vector whose components are four simultaneous equations and $2(M+N)$ unknowns, namely the expansion coefficients α_m^\pm and β_n^\pm . To solve these four simultaneous equations, the inner product of Eq. 3.18 and each basis component is formed, i.e.

$$\langle \Omega | [E^0 - IE + W(k)] | \bar{\Psi} \rangle = 0 \quad (3.19)$$

where $|\Omega\rangle$ is equal to one of the following $2(M+N)$ vectors

$$|\Omega\rangle = \begin{pmatrix} \xi_m(z) \\ 0 \\ 0 \\ 0 \end{pmatrix} \quad \text{or} \quad \begin{pmatrix} 0 \\ \varphi_n(z) \\ 0 \\ 0 \end{pmatrix} \quad \text{or} \quad \begin{pmatrix} 0 \\ 0 \\ \varphi_n(z) \\ 0 \end{pmatrix} \quad \text{or} \quad \begin{pmatrix} 0 \\ 0 \\ 0 \\ \xi_m(z) \end{pmatrix}$$

The result of performing these inner products is to generate $2(M+N)$ equations and $2(M+N)$ unknowns. These equations can be cast into matrix form, i.e.

$$\left[\begin{array}{c} 2(M+N) \\ \times \\ 2(M+N) \\ \equiv P \end{array} \right] \begin{pmatrix} \alpha_1^+ \\ \vdots \\ \alpha_M^+ \\ \beta_1^- \\ \vdots \\ \beta_N^- \\ \beta_1^+ \\ \vdots \\ \beta_N^+ \\ \alpha_1^- \\ \vdots \\ \alpha_M^- \end{pmatrix} = 0 \quad (3.20)$$

Remembering that P is dependent on the in-plane momentum, diagonalization of this matrix yields the k -dependent eigenvalues and eigenvectors. The wavevector dependence of the eigenvalues is the valence band structure of the heterostructure system. The eigenvectors correspond to the expansion coefficients required to diagonalize P , and thus, the hole wavefunction in a given band can also be found as a function of in-plane wavevector by using the corresponding eigenvector and Eq. 3.17.

Since the matrix P in Eq. 3.20 is a real symmetric matrix, it was diagonalized using Jacobi transformations. The code to build and diagonalize the matrix was written in Microsoft Quick C (version 2.51) and the Jacobi transformation routine was taken from Reference 45. The code was executed on a 66 MHz, 486 desktop PC.

As an example, the valence band structure of a 80 Å GaAs/Ga_{0.7}Al_{0.3}As single quantum well was calculated. The valence band dispersion is shown in Fig. 3-1. The bands are labeled by their character at the Γ -point. As expected, in the diagonal approximation (dashed curves) the bands are parabolic and cross at various in-plane wavevectors. The off-diagonal elements of Eq. 3.1 effectively mix the $k \neq 0$ solutions and, as a result, the crossings are replaced by anticrossings (solid curves). The mixing between the subbands is very strong, resulting in highly non-parabolic dispersions. In particular the subband labeled LH1 in Fig. 3-1 originates from a light-hole level. However, near $k = 0$, the subband displays an *electron-like* curvature. This is due to the strong

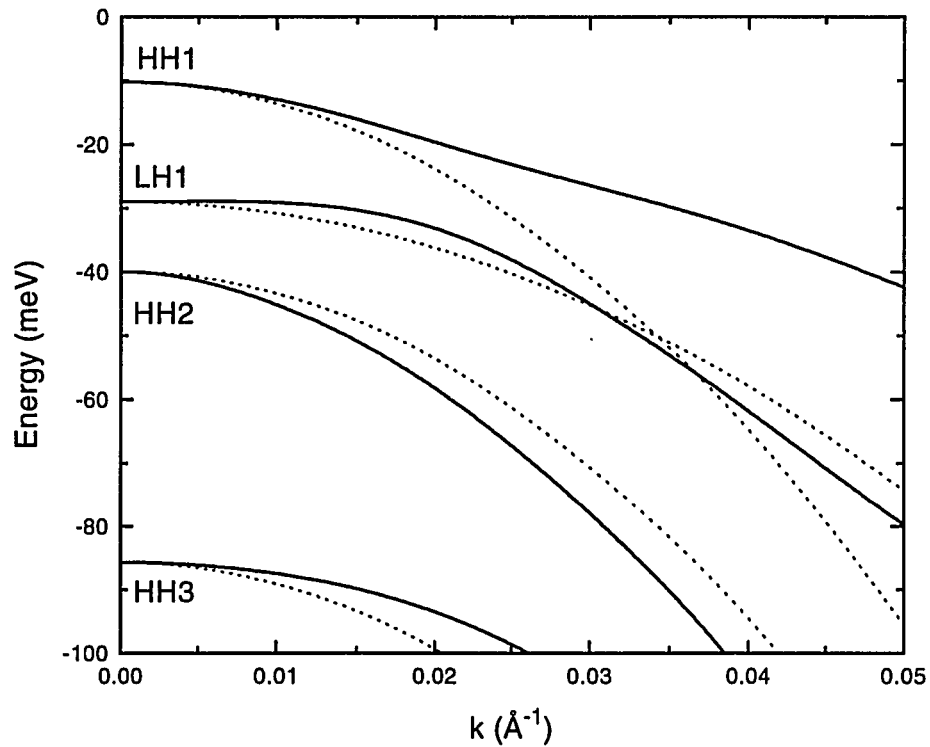


Figure 3-1 Calculated valence band structure of a 80 Å GaAs/Ga_{0.7}Al_{0.3}As single quantum well. The parameters used are $|V_p| = 117$ meV, $\gamma_1 = 6.85$, $\gamma_2 = 2.1$, and $\gamma_3 = 2.9$.^[46] The dashed lines represent the dispersion under the diagonal approximation.

coupling between LH1 and the subbands at lower energies over the repulsive coupling between LH1 and HH1. It is clear from these results that bandmixing cannot be neglected in the study of hole dynamics at nonzero in-plane wavevectors. The next section presents the band structure calculations for the ADQW structures investigated in Chapter 2.

3.2 ADQW Valence Band Dispersion

The formalism described in the previous section was used to calculate the hole band structure of the $\text{Ga}_{0.47}\text{In}_{0.53}\text{As}/\text{Al}_{0.48}\text{In}_{0.52}\text{As}$ 40/27/60 ADQW structure investigated in the Chapter 2. The Luttinger parameters used in the band structure calculations were estimated from

$$\gamma_1 = \frac{1}{2} \left(\frac{1}{m_l^*} + \frac{1}{m_h^*} \right) \quad (3.21a,b)$$

$$\bar{\gamma} = \frac{1}{4} \left(\frac{1}{m_l^*} - \frac{1}{m_h^*} \right)$$

where m_l^* and m_h^* are the light- and heavy-hole effective mass coefficients of the well material, respectively, and are listed in Table 2.1. The resulting values of γ_1 and $\bar{\gamma}$ are 11.02 and 4.18, respectively. The valence band offset was assumed to be 224 meV (see Table 2.2). The hole dispersion of the first four subbands of the 40/27/60 ADQW structure is shown in Fig. 3-2. The bands are labeled by their character at the Γ -point. The Kramer's degeneracy of each subband is lifted since the ADQW structure lacks inversion symmetry. The dispersion relations for the isolated single 40 and 60 Å quantum wells are shown as dashed lines. In the time-resolved experiments, the probe wavelength was tuned to the Γ -point of the first hole subband of the NW, labeled HH^N_1 . Hence, we are interested in the transfer of holes from this subband to the neighboring

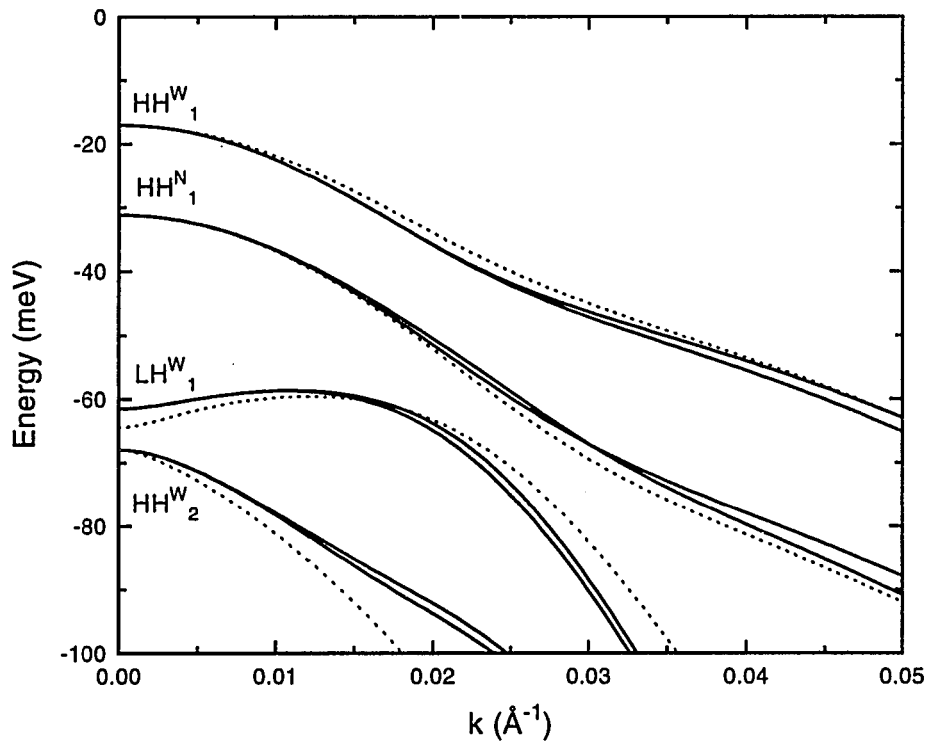


Figure 3-2 Valence band dispersion for the first four subbands of the 40/27/60 ADQW structure (solid lines). The valence band dispersion of the isolated 40 and 60 \AA quantum wells is also shown (dashed lines). The labels at $k = 0$ indicate the character of the bands at the Γ -point.

subbands, HH^W_1 and LH^W_1 . Immediately obvious is the absence of any crossings between subbands of the isolated quantum wells. Hence, holes created with large in-plane momenta (experimentally, the initial in-plane momentum was $k \approx 0.05 \text{ \AA}^{-1}$) do not have a resonant mechanism for fast hole tunneling from the NW to the WW. The band structure of the second (HH^N_1) and third (LH^W_1) subbands shows two very interesting features in the region of $k \approx 0.02 \text{ \AA}^{-1}$. The hole wavefunctions of both bands are strongly delocalized

in this momentum region and have no definite parity as found by Goldoni and Fasolino;[47] and the third subband, LH^W_1 , has a local maximum at $k \approx 0.01 \text{ \AA}^{-1}$. Hence, the density of states there is expected to be very large (in principle infinite).

The hole wavefunction of subband HH^N_1 (upper branch) at various in-plane momenta are shown in Fig. 3-3. All four components of the wavefunction given by Eq. 3.15 are shown. As expected at $k = 0$ the wavefunction is strictly heavy-hole in character and highly localized in the NW. However, as k is increased the wavefunction gains more light-hole character. As the in-plane momentum increases to $k = 0.02 \text{ \AA}^{-1}$ the amplitude of the

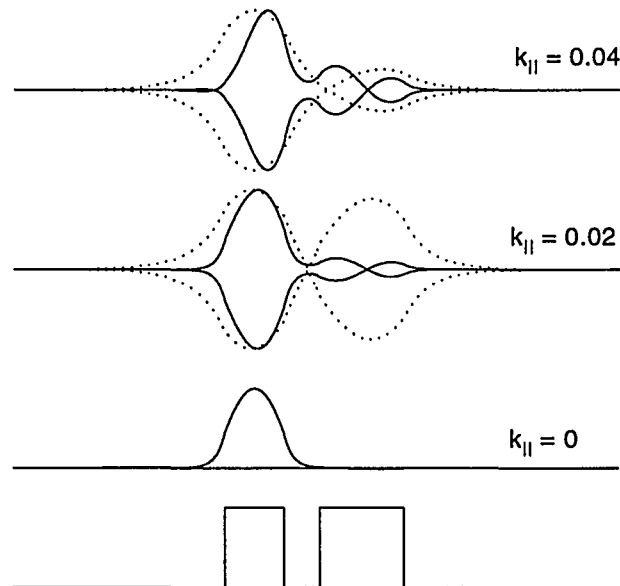


Figure 3-3 Hole wavefunction of the HH^N_1 subband (upper branch) at various in-plane momenta. The +/- heavy-hole (solid lines) and +/- light-hole (dashed lines) components are shown (where + and - indicate spin-up and spin-down, respectively).

heavy- and light-hole components become almost equal and both components are strongly delocalized over both the NW and WW. As the in-plane momentum increases further, the wavefunction retains the strong mix of heavy- and light-hole components but becomes more localized in the NW.

The enhanced delocalization of the hole wavefunctions is due to spin-coupling between the various subbands of the ADQW structure. To verify this, the band structure and hole wavefunctions were calculated without spin-coupling, i.e. the b terms in Eq. 3.1 were set equal to zero. The calculated band structure is shown

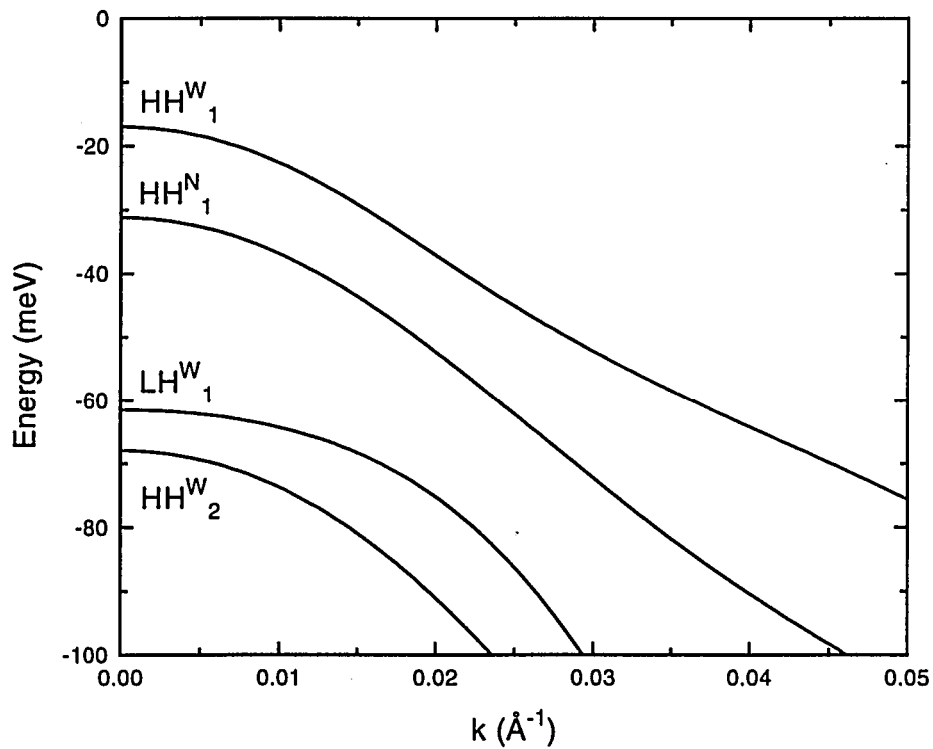


Figure 3-4 Valence band dispersion for the first four subbands of the 40/27/60 ADQW structure in the absence of spin-coupling.

in Fig. 3-4. As expected the spin-splitting of the subbands is suppressed in the absence of spin-coupling. The hole wavefunction of the HH^{N}_1 subband at various in-plane momenta is shown in Fig. 3-5. There is no enhanced delocalization of the heavy- and light-hole components at $k = 0.02 \text{ \AA}^{-1}$. Thus, spin-coupling results in a spin-dependent delocalization of the hole wavefunctions, and as will be shown in the next section can lead to subpicosecond hole tunneling times despite the absence of resonances between NW and WW hole subbands.

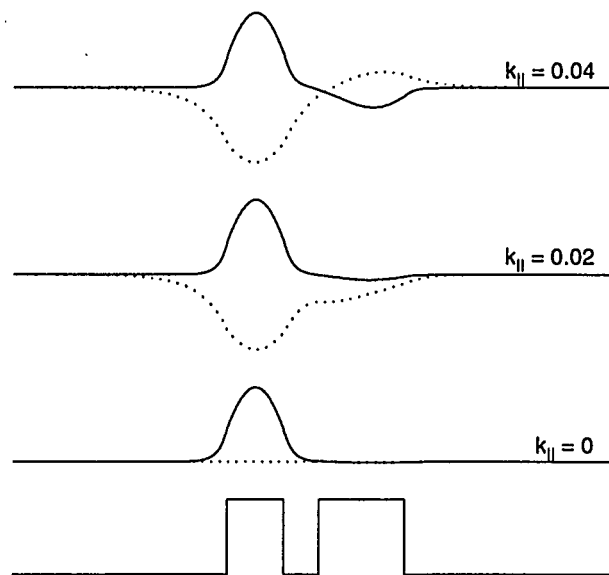


Figure 3-5 Hole wavefunction of the HH^{N}_1 subband at various in-plane momenta in the absence of spin-coupling. The +/- heavy-hole (solid lines) and +/- light-hole (dashed lines) components are shown (where + and - indicate spin-up and spin-down, respectively).

3.3 Hole Tunneling Times

To elucidate the contribution of the ADQW band structure to the hole tunneling process, the tunneling rates were estimated under the Born approximation by using the Fermi golden rule. After summing over all possible final states the Fermi rule becomes (see Appendix A),

$$\frac{1}{\tau} = \frac{S}{\hbar} \left[\frac{dk'}{d\varepsilon_{k'}} \right] \frac{1}{2\pi} \int_0^{2\pi} d\theta \left| \langle \varphi_{k'}(\vec{r}) | IV(\vec{r}) | \varphi_k(\vec{r}) \rangle \right|^2 \quad (3.22)$$

where $\varphi_k(\vec{r})$ and $\varphi_{k'}(\vec{r})$ denote the initial and final state 4x1 spinors in the growth direction, $V(\vec{r})$ is a general scattering potential, I is the 4x4 identity matrix, and S is the sample area. The inclusion of the identity matrix in Eq. 3.22 restricts the following treatment to spin-conserving transitions.

For disordered ternary semiconductors, i.e. $A_xB_{1-x}C$, one of the constituting atoms (C) occupies the sites of one of the face-centered cubic lattices of the zinc blende crystal. The other atoms (A and B) are randomly distributed on the sites of the second face-centered cubic lattice. While the underlying lattice is periodic, the crystal potential is not periodic. As a result, there are no Bloch waves, dispersion relations, etc. To treat disordered alloys, the virtual crystal approximation is used.[42] In this approximation, a periodic potential composed of an ‘‘average’’ atom is assumed for band structure calculations. The difference between the actual and virtual potentials acts as a strong scattering mechanism in semiconductor alloys, i.e. alloy scattering. As a result, for

disordered alloys such as $\text{Ga}_x\text{In}_{1-x}\text{As}$ and $\text{Al}_x\text{In}_{1-x}\text{As}$ intersubband transitions will be dominated by alloy scattering.[46] Hence, the scattering potential in Eq. 3.22 becomes

$$V_{\text{alloy}}(\vec{r}) = \Omega_0 \delta V \left[\sum_{\vec{R}_B} x \delta(\vec{r} - \vec{R}_B) - \sum_{\vec{R}_A} (1-x) \delta(\vec{r} - \vec{R}_A) \right] \quad (3.23)$$

where Ω_0 is the volume of the alloy unit cell, δV is the spatial average of the fluctuating alloy potential over the alloy unit cell, x is the A mole fraction in the ternary alloy $\text{A}_x\text{B}_{1-x}\text{C}$, and \vec{R}_i ($i = \text{A or B}$) is the spatial position of the scattering site.

Residual charged impurities in the lattice are a source of Coulombic scattering and are an efficient scattering mechanism in III-V semiconductors. The ionized impurity potential is proportional to $1/|\vec{r} - \vec{R}_i|$ where \vec{R}_i is the location of the charged impurity in the lattice. The potential can be Fourier analyzed and written in the form [42]

$$V_{\text{imp}}(\vec{r}) = \frac{2\pi e^2}{\kappa_0 S} \sum_{\vec{R}_i} \sum_{\vec{Q}} \left(\frac{1}{Q} \right) \exp[i\vec{Q} \cdot (\vec{\rho} - \vec{\rho}_i) - Q|z - z_i|] \quad (3.24)$$

where $\vec{R}_i = \vec{\rho}_i + z_i \hat{z}$, e is the electronic charge, and κ_0 is the static dielectric constant of the well material. By inserting Eq. 3.23 and 3.24 into Eq. 3.22 we obtain the following two expressions (see Appendix B for the derivation of these equations),

$$\left(\frac{1}{\tau} \right)_{\text{alloy}} = \frac{\Omega_0}{\hbar} [\delta V]^2 x(1-x) \{k'/|d\epsilon_{k'}/dk'\} \int |\chi_{k'}(z)|^2 |\chi_k(z)|^2 dz \quad (3.25)$$

and

$$\left(\frac{1}{\tau} \right)_{\text{imp}} = \frac{2\pi}{\hbar} \left(\frac{e^2}{\kappa_0} \right)^2 N_{\text{imp}} \{k'/|d\epsilon_{k'}/dk'\} \int_0^{2\pi} \frac{|I(Q, z_j)|^2}{Q^2} d\theta \quad (3.26)$$

where in Eq. 3.26

$$I(Q, z_j) = \int dz \chi_{k'}^*(z) \exp(-Q|z - z_j|) \chi_k(z) \quad (3.27)$$

$Q^2 = k^2 + k'^2 - 2kk' \cos\theta$, and θ is the angle in k -space. It should be noted that k and k' are fixed by the energy conserving delta function in Eq. A.1. The randomness of the alloy potential has been accounted for in Eq. 3.25 by averaging the squared modulus of the matrix element over the volume of the disordered alloy. Equation 3.25 is independent of Q due to the short range nature of $V_{\text{alloy}}(\mathbf{r})$, thus the alloy scattering assisted tunneling rate is directly proportional to the overlap integral of the probability densities in the growth direction and the density of final states. For $\text{Ga}_{0.47}\text{In}_{0.53}\text{As}/\text{Al}_{0.48}\text{In}_{0.52}\text{As}$ heterostructures we assumed $x = 0.47$, $d = 5.8688 \text{ \AA}$ ($\Omega_0 = d^3/4$), and $\delta V = 1.3 \text{ eV}$. [48] In Eq. 3.26, N_{imp} is the areal impurity concentration and was assumed to be 10^{10} cm^{-2} . The impurities are assumed to lie in a plane located at the NW/tunnel barrier interface.

The spin-conserving impurity-assisted tunneling times as a function of initial-state in-plane momentum k are shown in Fig. 3-6 for transitions from HH^{N}_1 to HH^{W}_1 and LH^{W}_1 . The dominant feature seen in Fig. 3-6 is the strong dependence of tunneling time on the initial state momentum, i.e. upon band mixing. As expected from Eq. 3.26, the tunneling times from HH^{N}_1 to LH^{W}_1 approach zero (infinite rate) as the initial state energy approaches the energy at which LH^{W}_1 goes through a local maximum. The tunneling times are, however, greater than 10 ps over the range of momentum values considered.

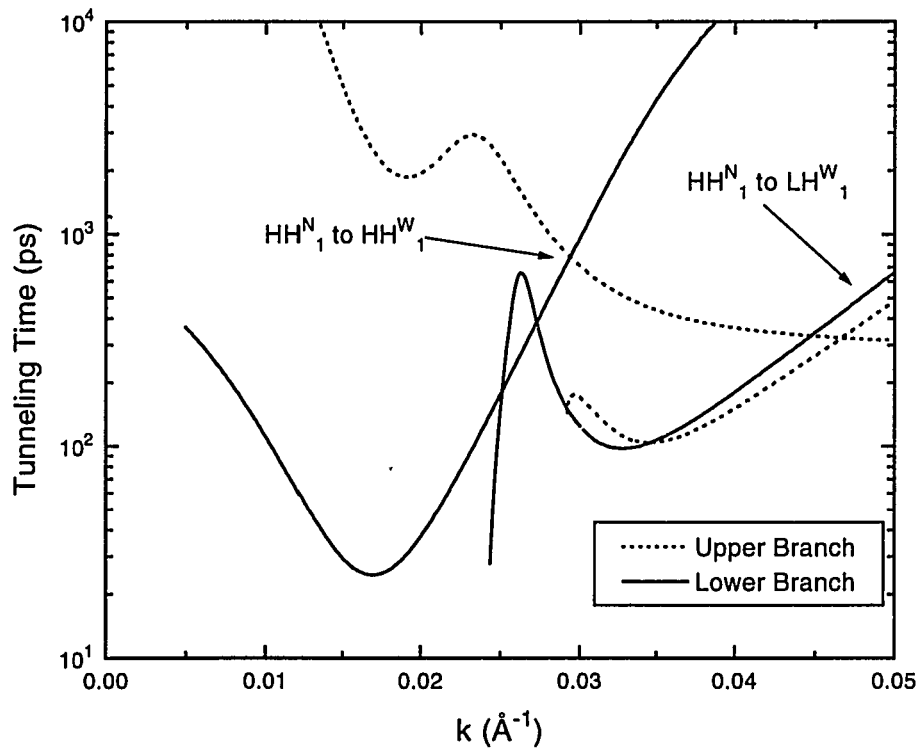


Figure 3-6 Calculated dependence of the impurity-assisted tunneling time on initial-state in-plane momentum.

Figure 3-7 shows the dependence of the spin-conserving alloy-assisted tunneling times on initial-state momentum for the same transitions as in the previous figure. The tunneling time is again strongly dependent on the initial state momentum and band mixing. In this case, however, the tunneling times are subpicosecond over a wide range of k . The tunneling times from HH^N_1 to LH^W_1 approach zero (infinite rate) as the initial state energy approaches the energy at which LH^W_1 goes through a local maximum. The

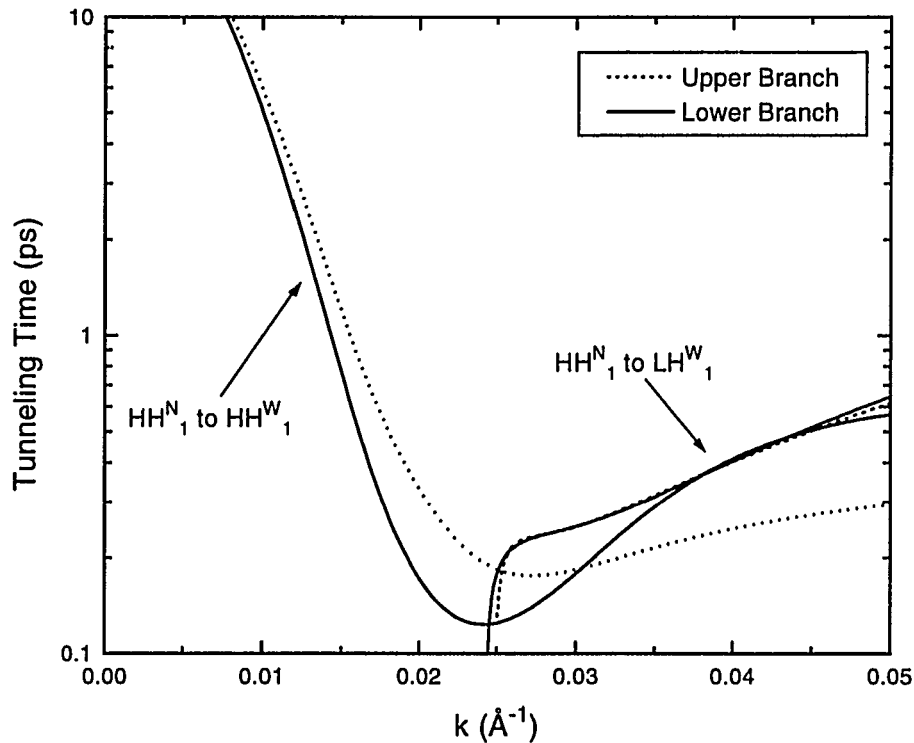


Figure 3-7 Calculated dependence of the alloy-assisted tunneling time on initial-state in-plane momentum.

tunneling times from HH^N_1 to HH^W_1 are also short in the region of $k \approx 0.025 \text{ \AA}^{-1}$. The delocalization of the hole wavefunction is enhanced in this momentum region due to spin-orbit coupling and band mixing. The overlap of the probability densities of HH^N_1 and HH^W_1 is therefore greatly increased, and hence, leads to subpicosecond tunneling times.

It is interesting to note that the impurity-assisted times are dependent on the overlap integral of the *probability amplitudes* in Eq. 3.27. The alloy-assisted times, on the other hand, are the result of the overlap integral of the *probability densities* in Eq. 3.25.

The different nature of the two processes can be seen in Figs. 3-6 and 3-7. The impurity-assisted times are much more sensitive to changes in the initial-state momentum. Since both of the scattering mechanisms considered are elastic processes, the final-state momenta and density of final-states are the same in each case. The drastic difference in the shape of the curves can only arise from the fact that interference between the initial- and final-state wavefunctions is important for the impurity-assisted case but is not important in the alloy-assisted case. Finally, these results prove that holes with finite k can tunnel from the NW to the WW on subpicosecond timescales.

3.4 Discussion

The results of the preceding analysis can be used to qualitatively explain the time-resolved data shown in Fig. 2-14. In the case of low carrier densities the transmission fully recovers with a time constant equal to the electron tunneling time implying that both the electrons and the holes tunnel with at least picosecond speeds. However, the hole tunneling time at the Γ -point (see Figs. 3-6 and 3-7) is at least an order of magnitude larger than the experimentally observed times. Hence, at low carrier densities the holes must tunnel from the NW to the WW *before* relaxing to the bottom of HH^{N}_1 , consistent with the theoretical results obtained in the previous section. On the other hand, at high carrier densities the hole states at the bottom of HH^{W}_1 become filled and block tunneling holes.

The rates of tunneling to the WW and relaxation in the NW become comparable in this case, and as a result, holes are scattered to the bottom of HH^N_1 generating the long-lasting component of the differential transmission signal in Fig. 2-14. This indicates that high injected carrier densities do generate a finite hole population at the Γ -point of HH^N_1 .

A point of caution is necessary: the band structure calculations presented in the first two sections of this chapter assumed flat-band conditions and are only accurate for low injected carrier densities. At high carrier densities the electrons and holes generated in the NW can become separated (holes in the WW and electrons in the NW) due to their different tunneling rates. The spatial separation of charge leads to the generation of an internal electric field which shifts the relative positions of the NW and WW levels (both electron and hole) with respect to each other. The resultant change in the potential can lead to significant changes in the valence band structure. Hence, the band structure and tunneling time results considered here are only valid for low injected carrier densities in the NW, i.e. $<10^{10} \text{ cm}^{-2}$. Experimentally, the lowest carrier density considered was $1.4 \times 10^{11} \text{ cm}^{-2}$. Of these carriers approximately $3.5 \times 10^{10} \text{ cm}^{-2}$ were generated in the NW with the remaining $1.05 \times 10^{11} \text{ cm}^{-2}$ being generated in the WW. The difference in carrier densities between the two wells stems from the larger WW width (1.5 times larger than the NW) and the existence of two allowed WW interband transitions at the pump energy as opposed to one in the NW. Hence, considering that our experimental carrier densities

seem to be slightly over-estimated, the flat-band assumption under which our band structure calculations were performed is justified.

3.5 Conclusions

The first experimental and theoretical evidence for ultrafast electron *and* hole tunneling in ADQWs has been presented. In particular, it was shown in this chapter that alloy scattering due to random alloy disorder in ternary semiconductors leads to highly efficient hole tunneling during the relaxation process to the Γ -point. Other studies of hole tunneling exclusively utilized GaAs/(Ga,Al)As ADQW structures. However, since GaAs is a binary compound, alloy disorder does not play a significant role in the tunneling and relaxation dynamics (the (Ga,Al)As tunnel barrier is disordered, but the overlap of the wavefunctions is small in this region). Efficient hole tunneling mechanisms in the binary materials such as impurity scattering were shown to be much less efficient than alloy scattering in ternary materials. Indeed, the results presented here show that alloy-assisted tunneling times are at least two orders of magnitude faster than impurity-assisted times. Finally, these results indicate that (Ga,In)As/(Al,In)As ADQW materials may have the potential to offer wavelength compatibility with optical-fiber based applications and the high operating speeds compatible with future optical interconnect systems.

CHAPTER 4

ELECTROABSORPTION IN ASYMMETRIC DOUBLE QUANTUM WELLS

Electro-optic nonlinearities in semiconductor heterostructures[1] have become an important means of transducing electronic data onto optical signals for communications systems.[2] The most common nonlinearity employed to produce electroabsorption and refraction in semiconductor quantum wells is the quantum confined Stark effect (QCSE).[49] In this chapter, the QCSE is reviewed and experimental results demonstrating electroabsorption in (Ga,In)As/(Al,In)As asymmetric double quantum well (ADQW) structures is presented. Additionally, novel field-dependent excitonic effects in ADQWs will also be discussed.

4.1 The Quantum Confined Stark Effect

The effect of a static external electric field on the energy levels of a semiconductor quantum well can be treated using the formalism of time-independent perturbation theory. The results of perturbation theory are accurate as long as the perturbation, i.e. the external field, is small compared to the energies involved in the unperturbed system. More concisely, the total Hamiltonian of the system can be written as $H = H^0 + H^1$ where H^0 is the Hamiltonian for the quantum well system in the absence of an applied field and H^1 is

the perturbing Hamiltonian and equals $-eFz$ where F is the applied field, e is the electronic charge, and z is the coordinate along the growth axis of the quantum well structure.

To solve the time-independent Schrödinger equation we assume that to every eigenket $|n^0\rangle$ of H^0 with eigen-energy E_n^0 , there is an eigenket $|n\rangle$ of H with eigen-energy E_n . The eigenkets and eigen-energy of H^0 for a quantum well system are easily found using the matrix formalism described in Chapter 2. We then expand the eigenkets and eigenvalues of H in a perturbation series:

$$|n\rangle = |n^0\rangle + |n^1\rangle + |n^2\rangle + \dots \quad (4.1)$$

$$E_n = E_n^0 + E_n^1 + E_n^2 + \dots \quad (4.2)$$

The superscript denotes the j th-order term in the perturbation expansion. To find expressions for $|n\rangle$ and E_n the eigenvalue equation $H|n\rangle = E_n|n\rangle$ is solved to the desired order. The solution of this equation to 2nd order can be found in most quantum mechanics texts.[50] Thus, we proceed to the important results, namely, the expressions for $|n\rangle$ and E_n . To first order, i.e. $j = 1$, the n th eigenket of H is given by

$$|n\rangle = |n^0\rangle + \sum_{m \neq n} \frac{|m^0\rangle \langle m^0 | H^1 | n^0 \rangle}{E_n^0 - E_m^0} \quad (4.3)$$

To second-order, the n th eigen-energy is

$$E_n = E_n^0 + \langle n^0 | H^1 | n^0 \rangle + \sum_{m \neq n} \frac{|\langle n^0 | H^1 | m^0 \rangle|^2}{E_n^0 - E_m^0} \quad (4.4)$$

Equation 4.4 has been expanded to second-order since for quantum well structures which are symmetric about some origin the first-order term $\langle n^0 | H^1 | n^0 \rangle$ will be zero. For structures that are not symmetric about an origin, this term corresponds to a linear shift in the eigen-energies with applied field.

A necessary condition for the perturbation to be small is given by the following inequality:

$$\left| \frac{\langle m^0 | H^1 | n^0 \rangle}{E_n^0 - E_m^0} \right| \ll 1 \quad (4.5)$$

Thus, the condition depends on the magnitude of H^1 , the matrix elements of H^1 between unperturbed states, and the energy difference between the unperturbed levels.

To illustrate the effect of a static external field on the $n = 1$ eigen-energy of a quantum well system, consider the infinite potential well shown in Fig. 4-1. The eigenkets and eigen-energies of the infinite potential well system are given by [51]

$$|n^0\rangle = \sqrt{\frac{2}{L}} \sin\left(\frac{n\pi}{L}z\right) \quad (4.6)$$

and

$$E_n^0 = \frac{n^2 \pi^2 \hbar^2}{2m^* L^2} \quad (4.7)$$

where L is the well width, m^* is the particle effective mass, and \hbar is Planck's constant divided by 2π . Substituting eigenkets given by Eq. 4.6 into the first term of Eq. 4.4

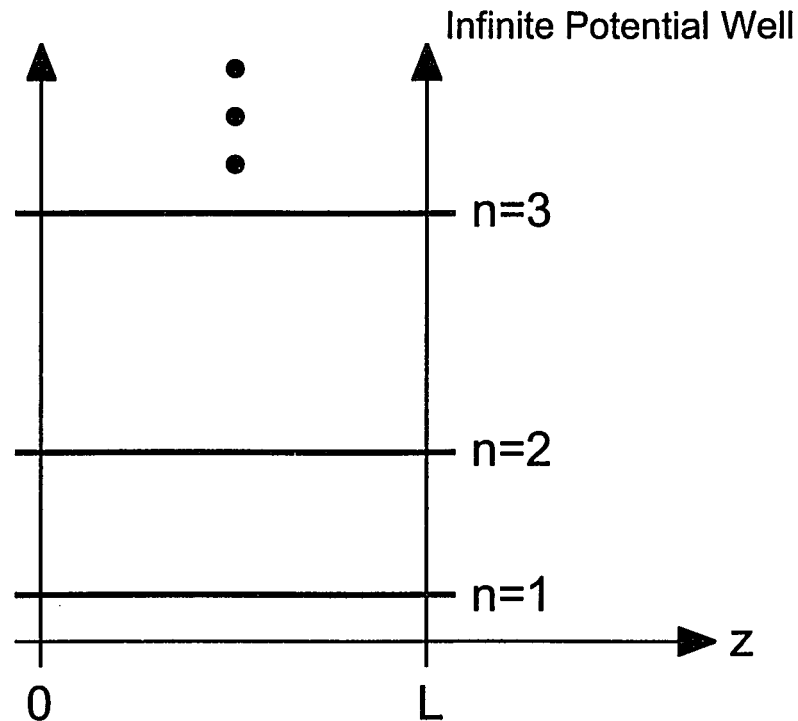


Figure 4-1 Schematic diagram of an infinite potential quantum well of width L . The bound states are labeled by their respective quantum number, n .

yields $\langle n^0 | H^1 | n^0 \rangle = -eFL/2$ and as expected is a linear function of applied field. The matrix element of the second term in Eq. 4.4 is equal to

$$\langle 1^0 | H^1 | m^0 \rangle = eF \frac{L}{\pi^2} \frac{8m}{(m-1)^2(m+1)^2} \quad (4.8)$$

and the energy difference in the denominator becomes

$$E_1^0 - E_m^0 = -\frac{\pi^2 \hbar^2}{2m^* L^2} (m^2 - 1) \quad (4.9)$$

Substituting Eqs. 4.8 and 4.9 into Eq. 4.4 gives the following expression for the $n = 1$ eigen-energy of an infinite potential quantum well system in the presence of a static external field:

$$E_1 = E_1^0 - \frac{1}{2}eFL - \frac{2m^*e^2F^2L^4}{\pi^6\hbar^2} \sum_{m>1} \frac{64m^2}{(m^2-1)(m-1)^4(m+1)^4} \quad (4.10)$$

For m greater than five, the summation is equal to 1.0727. Thus, Eq. 4.10 can be rewritten simply as

$$E_1 = E_1^0 - \frac{1}{2}eLF - \frac{2m^*e^2L^4F^2}{\pi^6\hbar^2} \Lambda \quad (4.11)$$

where

$$\Lambda = \sum_{m>1} \frac{64m^2}{(m^2-1)(m-1)^4(m+1)^4} = 1.0727 \quad (4.12)$$

Assuming Eq. 4.11 is for electrons in the conduction band, a similar expression can be derived for holes in the valence band:

$$E_1^h = -E_1^{0,h} - \frac{1}{2}eLF + \frac{2m_h^*e^2L^4F^2}{\pi^6\hbar^2} \Lambda \quad (4.13)$$

where the zero in energy is taken as the top of the valence band, i.e. increasing hole energy is negative. The minimum optical transition energy, neglecting excitonic effects, is given by $\hbar\omega_1 = E_g + E_1^e - E_1^h$ where E_g is the bulk well material bandgap energy. Expressing the optical transition energy in terms of Eqs. 4.13 and 4.11 results in

$$\hbar\omega_1 = E_g + E_1^{0,e} + E_1^{0,h} - \frac{2e^2L^4F^2}{\pi^6\hbar^2} \Lambda(m_c^* + m_h^*) \quad (4.14)$$

Equation 4.14 illustrates the important effect of a static external field on the optical absorption edge of a quantum well system. The bandgap energy decreases quadratically as the field increases. In this regime, i.e. low fields, the effect is called the quadratic Stark shift. More importantly for device applications is the dependence on well width. The shift of the absorption edge depends on the 4th power of the well width. Hence, wide wells will exhibit a much larger Stark shift than narrow wells. Figure 4-2 illustrates these properties for 40 and 70 Å infinite potential quantum wells. As expected the shift is quadratic with increasing field. However, the shift for the 70 Å well is much larger than the shift for the 40 Å well due to the strong dependence of the Stark shift on well width.

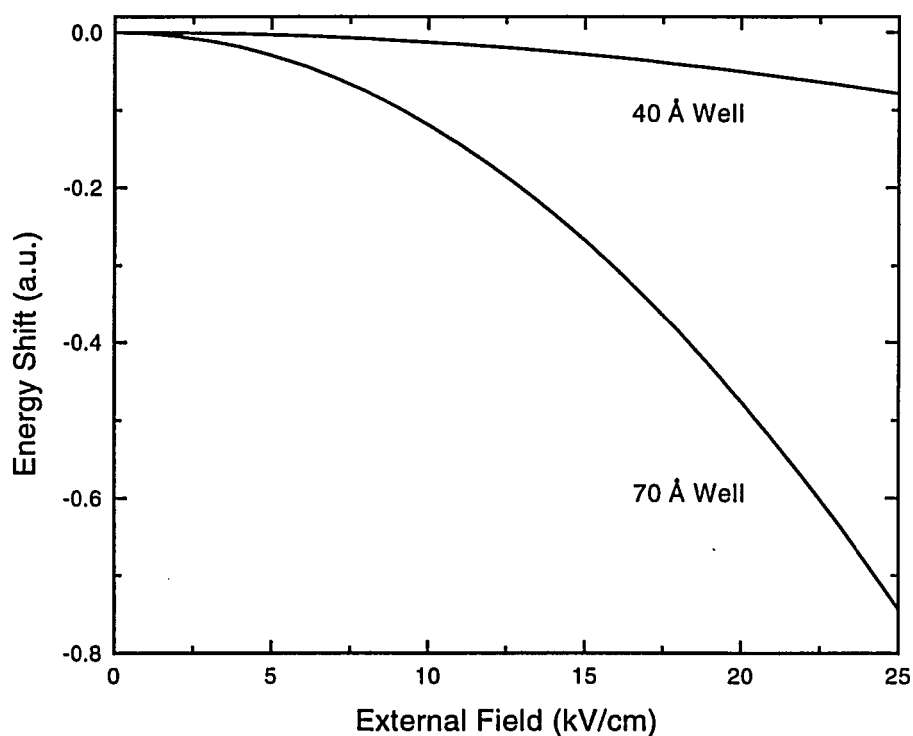


Figure 4-2 Well width dependence of the Stark shift for the lowest energy optical transition of an infinite potential quantum well.

At high fields, the perturbative approach is no longer valid since H^1 becomes comparable to the energy difference between the quantum well bound levels. In this case, the time-independent Schrödinger Equation $(H^0+H^1)|\phi\rangle = E|\phi\rangle$ must be solved exactly. The solutions to the Schrödinger Equation are Airy functions and can be found by matrix techniques as described by Austin and Jaros.[52] The bound-states shift sub-quadratically at high fields, i.e. $\Delta E_1 \propto F^\beta$ $\beta < 2$. [42] With the application of any field, the bound-states of the flat-band case become unbound and form Stark resonances, implying that all energies are now allowed eigenstates of the system. As illustrated in Fig. 4-3, a conduction band electron has a high probability of tunneling through the triangular potential barrier at high enough fields. Thus, the resonances correspond to lifetime broadening of the bound levels, $\Delta E\Delta T \geq \hbar/2$, due to field-induced ionization of the quantum well.

To demonstrate the effects described above, the electroabsorption properties of a (Ga,In)As/(Al,In)As ADQW structure have been studied. The sample was grown by molecular beam epitaxy on an *n*-type (100) InP substrate. The electrical bias was applied via a *p-i-n* mesa diode consisting of a 0.35 μm layer of *n*-type $\text{Al}_{0.48}\text{In}_{0.52}\text{As}$ (Si, $2 \times 10^{18} \text{ cm}^{-3}$) followed by a 1.035 μm intrinsic region and capped with a 0.2 μm layer of *p*-type $\text{Al}_{0.48}\text{In}_{0.52}\text{As}$ (Be, $2 \times 10^{18} \text{ cm}^{-3}$) and a 200 \AA *p+* $\text{Ga}_{0.47}\text{In}_{0.53}\text{As}$ contact layer. The intrinsic region consisted of 30 periods of 100 \AA $\text{Al}_{0.48}\text{In}_{0.52}\text{As}$ barrier/ 70 \AA $\text{Ga}_{0.47}\text{In}_{0.53}\text{As}$ wide well/ 35 \AA $\text{Al}_{0.48}\text{In}_{0.52}\text{As}$ tunnel barrier/ 40 \AA $\text{Ga}_{0.47}\text{In}_{0.53}\text{As}$ narrow well all between

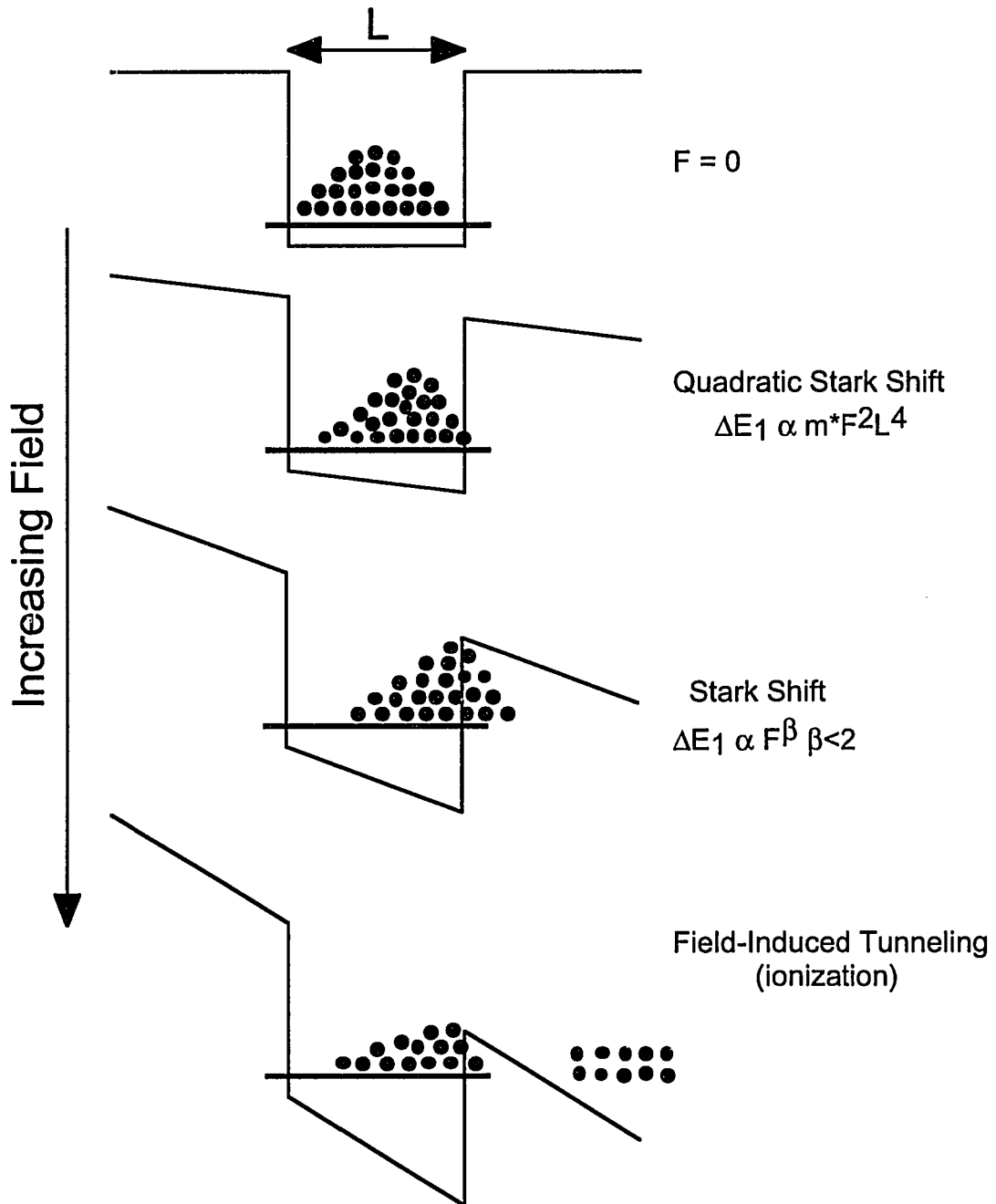


Figure 4-3 Evolution of the $n = 1$ bound state of a finite-potential quantum well as a function of increasing external field.

two layers of 0.15 μm undoped $\text{Al}_{0.48}\text{In}_{0.52}\text{As}$. The wafer was processed into 200 μm diameter mesa diodes with ring top contacts to allow optical transmission experiments. The field dependent transmission spectra were measured in a standard white-light spectroscopy system. The *p-i-n* diodes were illuminated with chopped light from a tungsten lamp. The transmitted light was dispersed and detected using a 1/4-meter spectrometer and Ge photodiode/lock-in amplifier, respectively. The transmitted light was normalized to the detected tungsten lamp spectrum to account for the spectral dependence of the spectrometer throughput and detector responsivity. The absorbance spectra, i.e. $\alpha(\lambda)L$, were then calculated from the transmittance data using Beer's Law.

The measured room temperature absorbance spectra are shown in Fig. 4-4. The long wavelength set of light- and heavy-hole exciton absorption resonances are associated with the 70 \AA wide well (WW) and the short wavelength set is associated with the 40 \AA narrow well (NW). As expected from the preceding discussion, the WW heavy-hole exciton resonance Stark shifts much faster with increasing field than the NW resonance due to the well width dependence of the Stark effect. Since the electrons and holes are oppositely charged particles, the external field separates the electrons and holes (their wavefunctions shift to opposite sides of the well) creating a static dipole. The static dipole results in a decrease of the envelope wavefunction overlap and hence a decrease of the interband absorption strength as observed in the spectra shown in Fig. 4-4. The separation of the wavefunctions is also dependent on the well width, i.e. the wider the

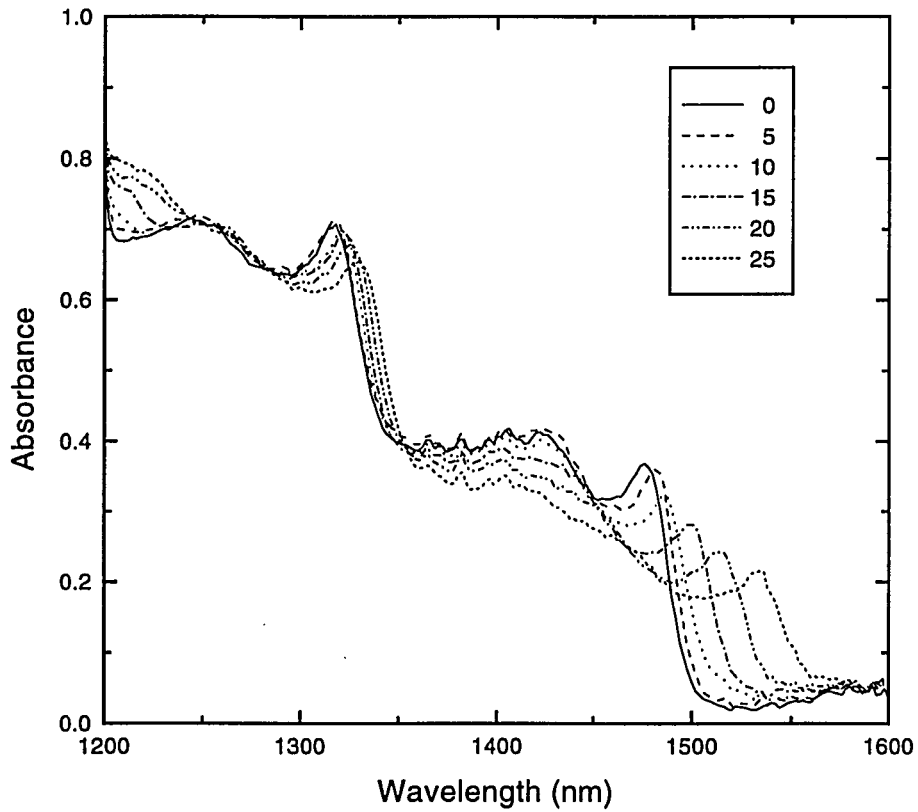


Figure 4-4 Room temperature optical absorbance spectra of a 40/35/70 ADQW structure for applied voltages of 0, 5, 10, 15, 20, and 25 V, respectively. The built-in potential of the p - i - n diode at room temperature was estimated to be 0.95 V.[63]

well the larger the separation. Another feature apparent in Fig. 4-4 is the broadening of the heavy-hole exciton resonance as the applied field is increased. The broadening is related to the field-ionization of the confined exciton system and again corresponds to lifetime broadening of the excitonic absorption resonance. In bulk semiconductors, the heavy-hole exciton resonance becomes field-ionized at relatively low field strengths. However, the additional confinement provided by the quantum well structure dramatically increases the field required to ionize the exciton. The combination of all the

field dependent effects discussed, i.e. the shift of the absorption edge, decreased oscillator strength, and increase in the excitonic ionization field strength, is called the quantum confined Stark effect (QCSE).[49]

4.2 Field-Dependent Excitonic Effects in ADQWs

The effects of coupling between the narrow well and wide well of an ADQW structure can be observed by examining the field dependence of the NW or WW excitonic absorption features. As illustrated in Fig. 4-5 the NW level shifts faster with increasing field due to the first term in Eq. 4.4. Hence, when the external field is large enough, i.e. $F = F_R$, the lowest two electron energy levels shift into resonance. At resonance, the wavefunctions of the two states are delocalized over the entire ADQW structure and the single exciton absorption resonance transforms into a doublet. Although the system lacks inversion symmetry, the lower state has symmetric character while the upper state has anti-symmetric character. At fields greater than F_R , the wavefunctions become localized again in their respective wells. It is important to note that the levels do not cross. The degeneracy of the two levels at the resonance field is replaced by an anti-crossing. Figure 4-6 illustrates the anti-crossing behavior of the first two ($n = 1$ and $n = 2$) electron levels of a 70/30/100 ADQW structure.[53] At fields lower than F_R , the $n = 1$ ($n = 2$) energy state is characterized by a wavefunction which is highly

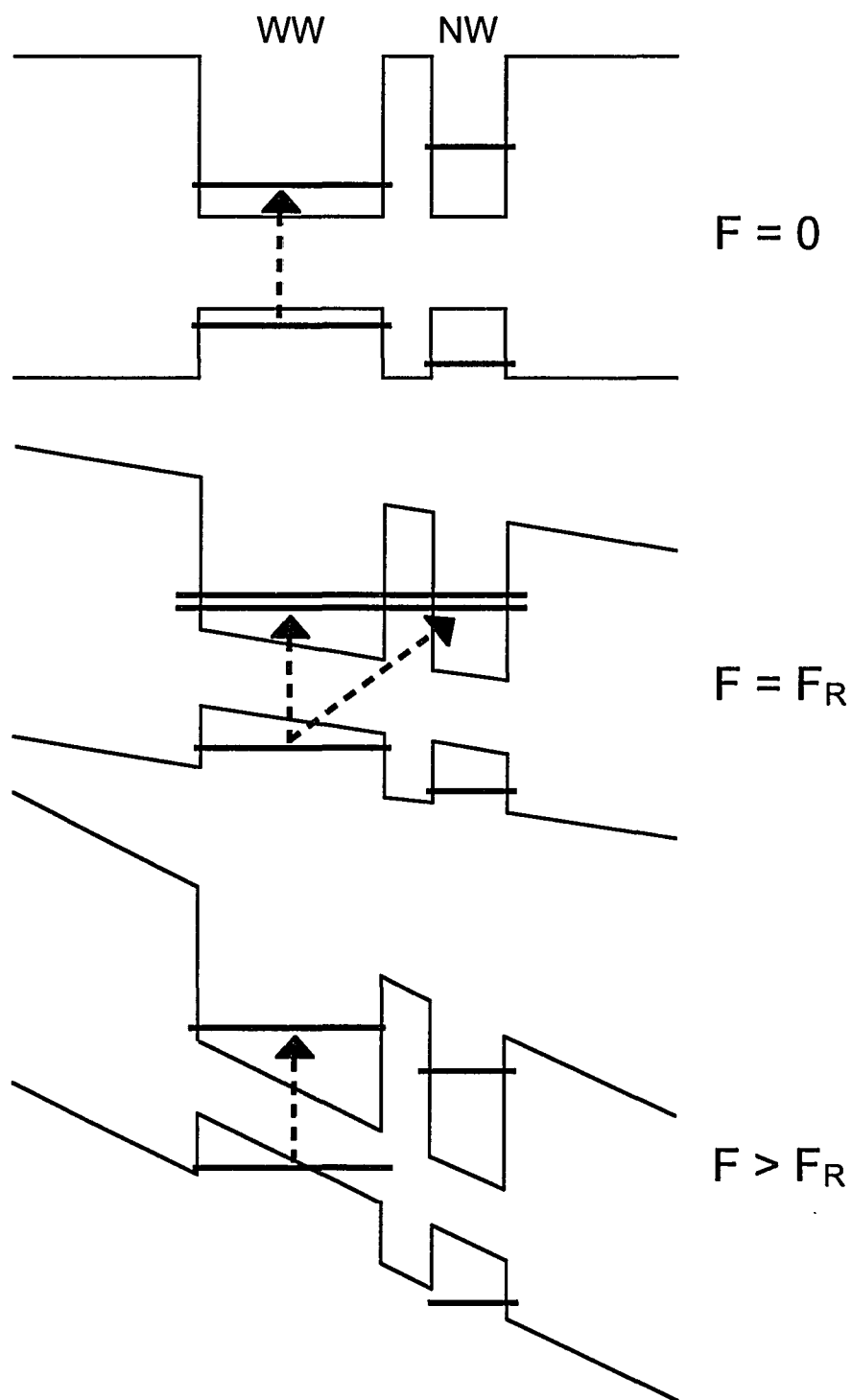


Figure 4-5 Schematic diagram of the ADQW structure with the applied field equal to zero, the resonance field, and some value beyond resonance.

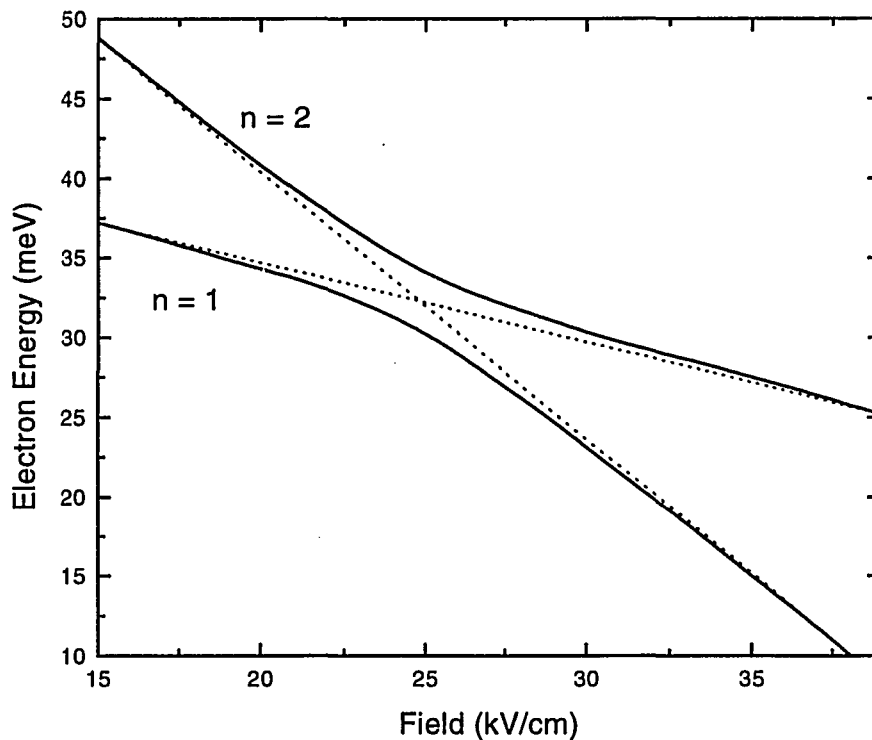


Figure 4-6 Anti-crossing behavior of the $n = 1$ and $n = 2$ electron levels of a 70/30/100 ADQW structure. The dashed lines show the shifts of the levels for isolated 70 and 100 Å single quantum wells.

localized in the WW (NW). At resonance the $n = 1$ ($n = 2$) wavefunction becomes delocalized over both wells. Past resonance, however, the $n = 1$ ($n = 2$) state takes on the character of the low field $n = 2$ ($n = 1$) state and becomes localized in the NW (WW).

To experimentally investigate the anti-crossing behavior of electron levels in ADQW structures, the field dependent absorption properties of the (Ga,In)As/(Al,In)As ADQW structure described in the last section was studied at low temperature. The measurement system is the same as described previously except the ADQW sample was

mounted in a closed-cycle helium cryostat and held at a temperature of 50 K. The electron level crossing was investigated by monitoring the field-dependence of the NW heavy-hole excitonic absorption spectrum. The measured optical spectra are shown in Fig. 4-7. In the figure, each successively higher spectrum corresponds to a higher external field. The resonance occurs for an applied voltage of approximately -8.5 V. As expected at low fields, only one excitonic resonance is observed. As the field is increased, a lower

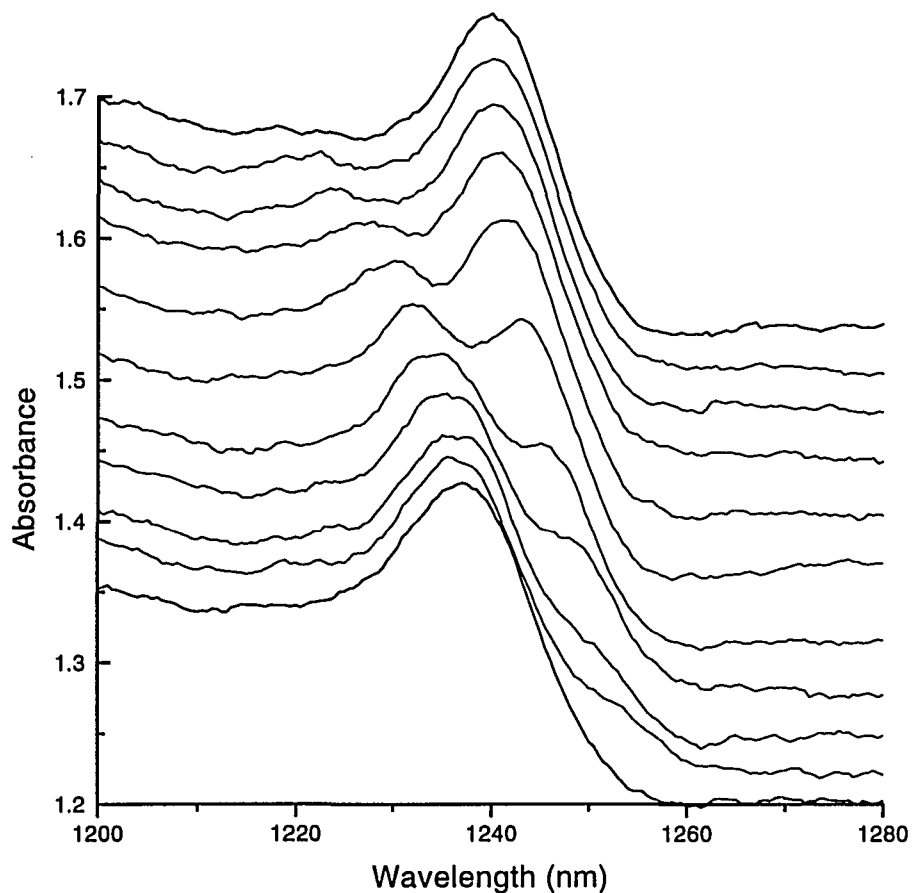


Figure 4-7 Measured NW heavy-hole excitonic absorbance spectra at fields near the resonance value. The spectra are offset for clarity with increasing field corresponding to successively higher curves. The applied biases range from -7.0 to -10.0 V.

energy peak begins to gain strength. This peak corresponds to the formation of the doublet state as the field approaches the resonance value. The strength of the low energy resonance increases as the wavefunction initially localized in the WW becomes delocalized over both wells while the strength of the primary peak decreases as the wavefunction initially localized in the NW becomes delocalized over both wells. As expected, the peaks do not cross at resonance. For fields beyond the resonance value, the strength of the primary peak continues to diminish as the associated wavefunction becomes highly localized in the WW. The low energy peak, on the other hand, continues to gain strength and becomes the dominant feature in the excitonic spectrum at fields beyond resonance. At resonance, the two eigenstates forming the doublet can be simultaneously excited by a broadband optical source. The evolution of the superposition of the two eigenstates forms an electron wavepacket which oscillates between the two wells. The existence of the oscillating wavepacket has been demonstrated by four-wave-mixing spectroscopy and terahertz radiation experiments.[54,55]

From the illustration of Fig. 4-5, the WW and NW heavy-hole exciton resonances are expected to split at the same field. Figure 4-8 shows the measured optical spectra over a wavelength range encompassing both the WW and NW excitonic transitions. Each successively higher spectrum in the figure corresponds to a higher external field. At the lowest bias, the NW heavy-hole exciton resonance is developing the weak low energy peak discussed above. The WW resonance does not show any indication of splitting at

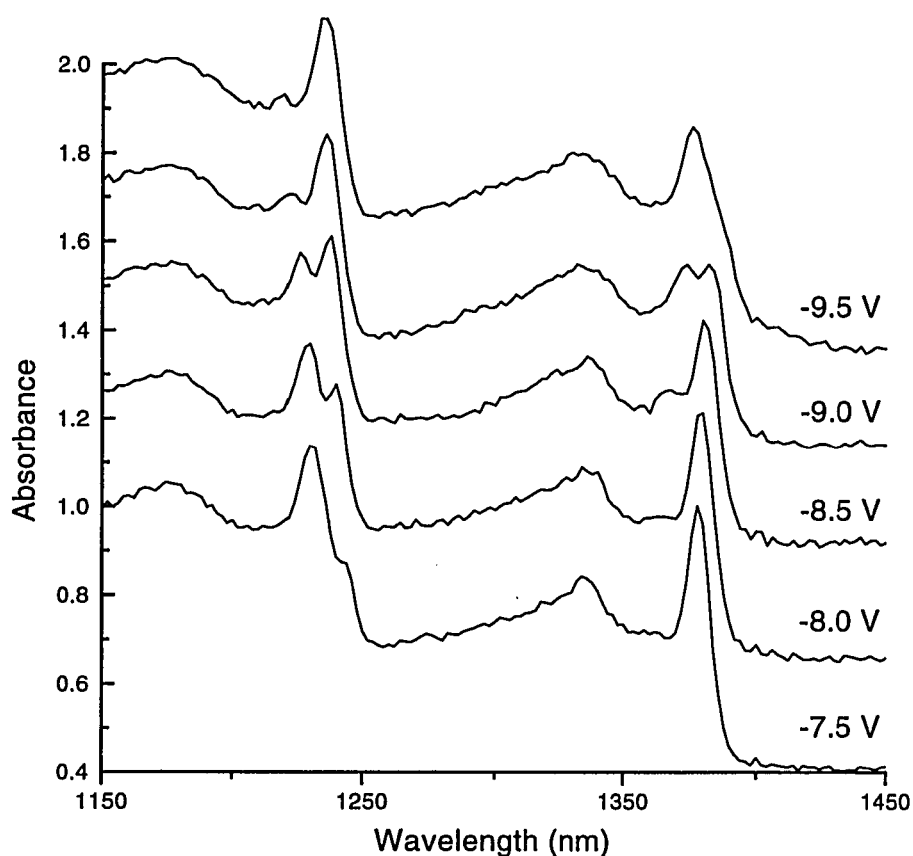


Figure 4-8 Measured absorbance spectra at fields near the resonance value over a wavelength range encompassing both the NW and WW excitonic transitions. The spectra are offset for clarity.

this bias. The NW exciton resonance splits at a bias voltage of -8.5 V. However, the WW resonance is just beginning to develop a weak high energy peak. As the bias is increased to -9.0 V the WW exciton splits into a doublet while the NW transition has already shifted through resonance. Hence, we have observed that the NW and WW heavy-hole excitonic transitions do not shift into resonance at the same external field. Fox, et al. has

shown that the binding energy of a spatially indirect exciton is smaller than the binding energy of a spatially direct transition.[25] As shown in Fig. 4-9, the different binding energies decreases the required field for the minimum splitting of the NW transitions with respect to the resonance of the “bare” electron levels, but increases the field required for the minimum splitting of the WW transitions. Hence, the measured exciton splitting observed in the previous two figures does not correspond to the “bare” electron level splitting as illustrated in Fig. 4-5.

4.3 Discussion

The theoretical and experimental results presented in the first section of this chapter demonstrate a fundamental problem: the wavelength requirements of optical fiber based applications restricts the required well widths to 40 and 85 Å when the (Ga,In)As/(Al,In)As system is used. The narrow well widths required result in a relatively small QCSE and the need to use large bias voltages which are incompatible with standard electronics, i.e. TTL and ECL. Although quaternary materials with wider well widths could be used instead, crystal growth complications make their use less desirable. Lattice matched (Ga,Al,In)As crystal growth on InP is sensitive to small changes in alloy composition. Hence, the growth of quaternary material requires MBE equipment with two Al sources. Changing the Al concentration between layers with a single Al cell is

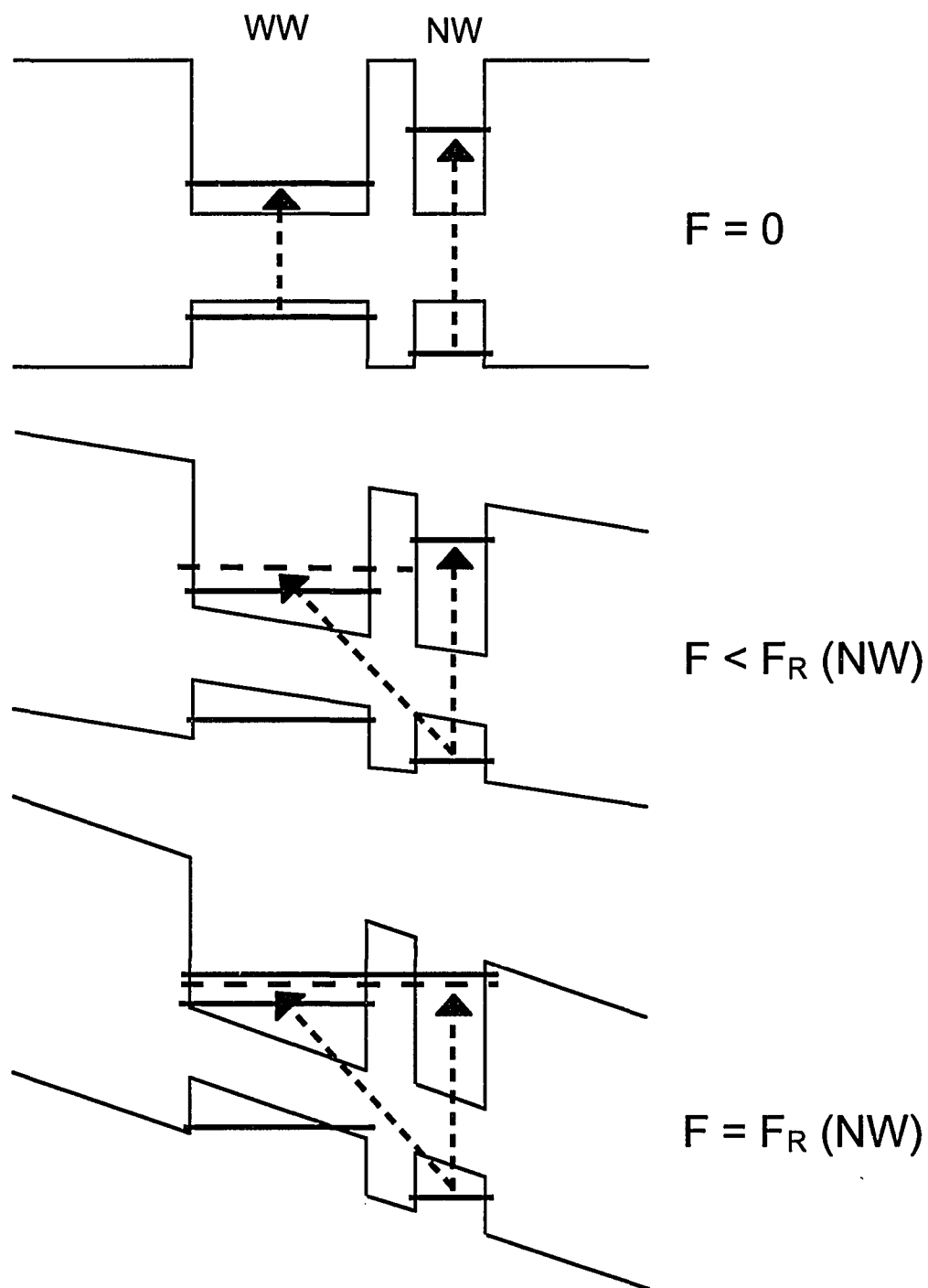


Figure 4-9 Schematic diagram showing the origin of the different resonance fields for the NW and WW exciton transitions due to the smaller binding energy of a spatially indirect transition. The dashed levels represent the first excited state of the spatially indirect excitonic transition.

impractical because of the long time required to ramp and stabilize the cell temperature to obtain high quality material. Thus, it is desirable to utilize ternary materials and a single Al source. In the next chapter, a novel method to enhance the electroabsorption properties of (Ga,In)As/(Al,In)As ADQWs based on real-space transfer of excess electrons will be presented.

CHAPTER 5

ENHANCED ELECTROABSORPTION IN DOPED ASYMMETRIC DOUBLE QUANTUM WELLS

For material systems such as (Ga,In)As/(Al,In)As quantum wells lattice matched to InP which are compatible with the optical fiber transmission windows of 1.3 and 1.5 μm , the quantum confined Stark effect (QCSE) is small due to the relatively low electron and heavy-hole effective masses and the restriction on suitable well widths, i.e. 40 and 85 \AA , respectively. The use of electron transfer between a quaternary reservoir and single quantum well and the use of coupled quantum wells have been shown to be attractive alternatives for optical fiber compatible device applications.[24,28,31] Additionally, a large field-induced blue-shift of the heavy-hole exciton absorption resonance has been observed in narrow GaAs/(Al,Ga)As asymmetric coupled quantum wells near the heavy-hole resonance.[23] Although recent results utilizing the (Ga,Al,In)As/(Al,In)As on InP system have demonstrated improved material quality and device performance at these wavelengths[3,33,38], improvements in the electro-optic characteristics of these materials is still required. In this chapter, a novel electroabsorption mechanism based on selective doping of (Ga,In)As/(Al,In)As asymmetric double quantum wells (ADQWs) is demonstrated.[36] The modulator utilizes real space transfer of excess electrons to

provide efficient absorption modulation. The results are compared to absorption changes in an undoped ADQW structure which utilizes the QCSE.

5.1 Real-Space Electron Transfer in ADQWs

To study the real-space transfer of electrons in (Ga,In)As/(Al,In)As ADQWs, the sample described in Section 4.1 was used. This ADQW structure is ideal for studying charge transfer since the ADQWs were designed to have the narrow well (NW) closer to the *n*-doped side of the *p-i-n* diode. The wide well (WW), on the other hand, is closer to the *p*-doped side of the diode. The orientation of the ADQWs allows electrons initially generated in the WW to transfer to the NW as a reverse bias is applied to the diode. The application of a reverse bias is critical for eliminating unwanted current flow through the diode.

To study the steady-state electron transfer process in ADQWs, time-integrated photoluminescence (PL) spectroscopy was utilized. Although time-integrated PL is a common technique, the experimental arrangement used here is unique in the fact that we used a continuous-wave Cr:Forsterite laser (see Section 2.3 for a description of the Forsterite laser) as the pump source. The Forsterite laser offers the capability to pump samples in the 1.2 to 1.3 μm region. For the present study, the ability to pump only the WW and not the NW was imperative since this is how a charge density localized in the

WW was generated. The experimental setup was a standard PL arrangement. The ADQW sample was mounted in a closed-cycle helium cryostat and held at a constant temperature of 8.5 K throughout the steady-state measurements. The sample was pumped by tuning the Forsterite laser to 1275 nm. The pump wavelength is between the lowest allowed transition in the NW (1238 nm) and the lowest allowed transition in the WW (1370 nm). Hence, electrons and holes are only generated in the WW. The PL from the sample was then dispersed using a 1/4-meter spectrometer and detected using a calibrated InGaAs linear diode array/OMA combination.

The measured PL spectra at various applied bias voltages are shown in Fig. 5-1. At zero applied bias, only one PL peak is observed corresponding to the radiative decay of free heavy-hole excitons in the WW. As the reverse bias is increased, a small Stark shift of the PL peak to longer wavelengths is observed. When the reverse bias reaches a value of ≈ 8.0 V, the PL peak splits into two peaks. As discussed in Chapter 4, the splitting is due to the anti-crossing of electron levels, and it indicates that electrons which were highly localized in the WW at low biases are now delocalized over both the wide and narrow wells. Further evidence of the electron delocalization is seen as the reverse bias is increased. For reverse biases greater than 8.0 V, the second peak becomes clearly separated from the initial PL peak. In fact, as the bias is increased, the second peak shows a continuous shift to longer wavelengths. The long wavelength peak originates

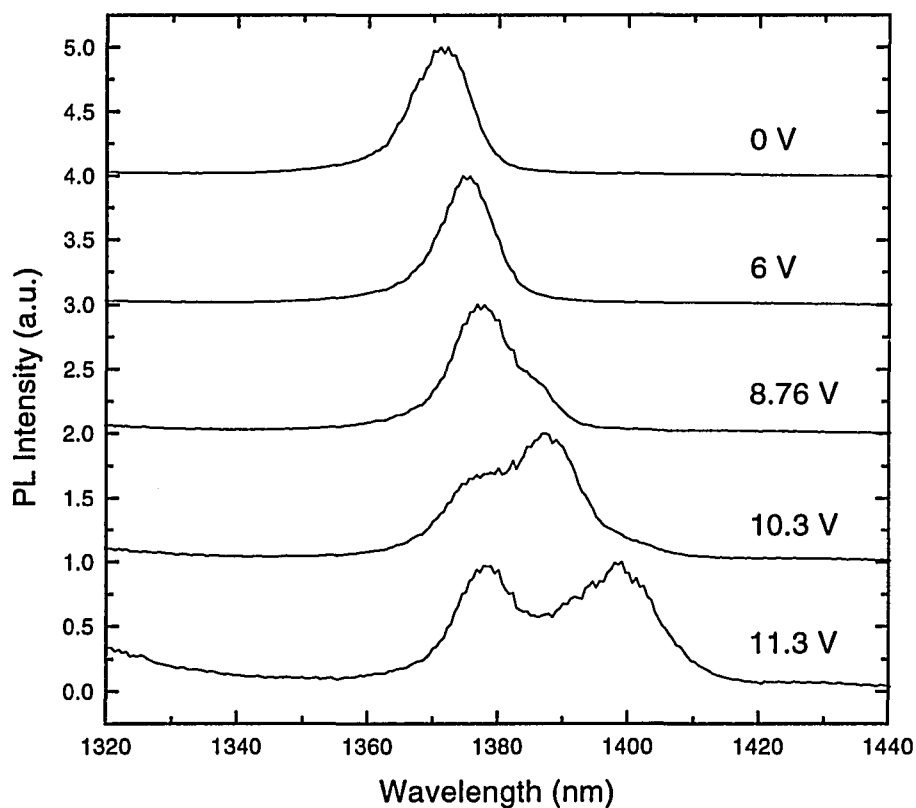


Figure 5-1 Time-integrated PL spectra at different applied reverse biases. The long wavelength PL peak appearing at biases greater than 8.0 V indicates strong transfer of electrons from the WW to NW.

from the spatially-indirect transition (cross-transition) between electrons localized in the NW and holes localized in the WW as shown in Fig. 5-2. It should be noted that the matrix element for the cross-transition is small due to the spatially localized envelope wavefunctions of the electrons and holes. Hence, the density of transferred electrons must be large in order for a relatively large PL signal at this transition energy to be present.

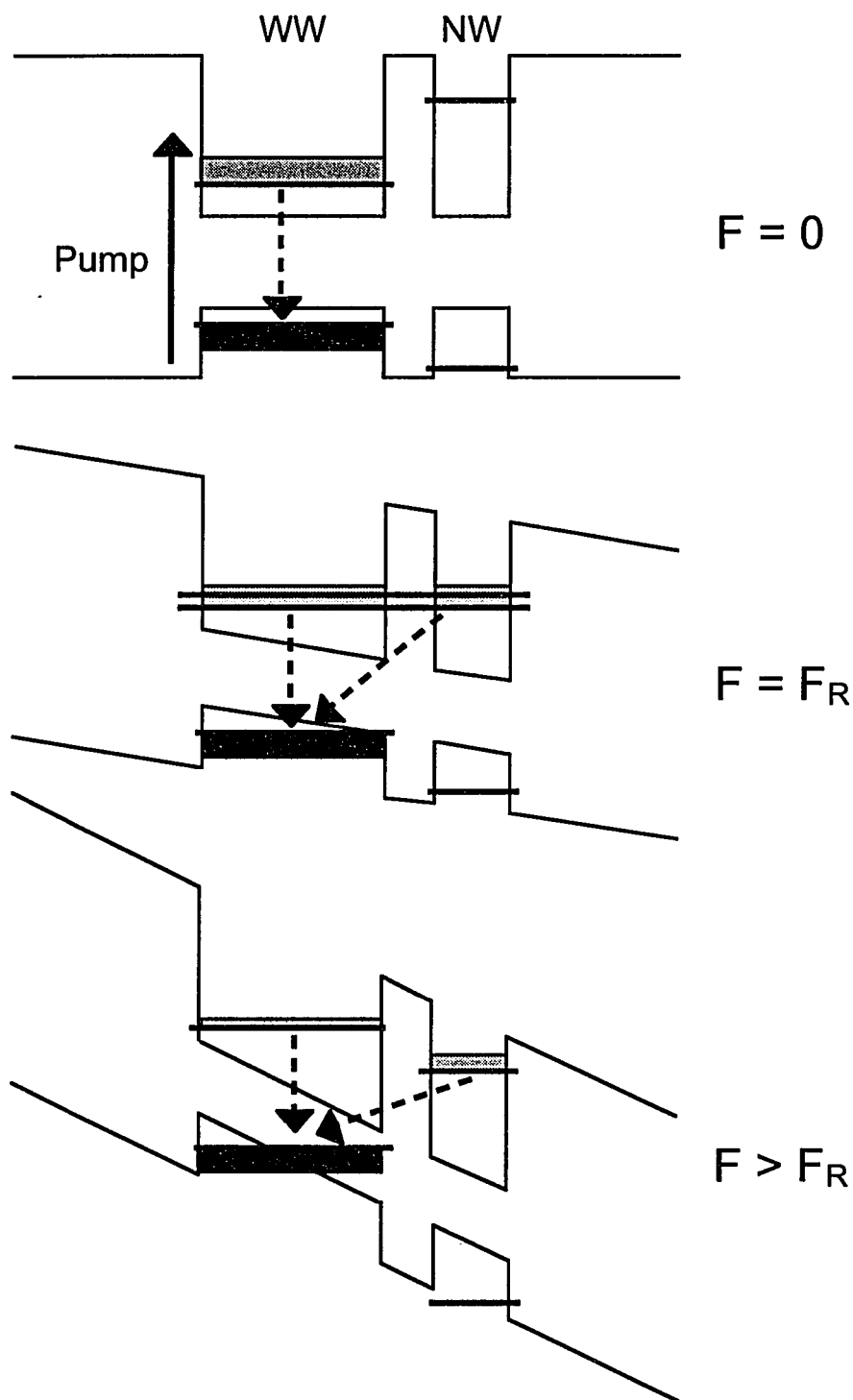


Figure 5-2 Schematic diagram of the ADQW structure illustrating the relevant optical transitions with the applied field equal to zero, the resonance value, and some value beyond resonance. The light (dark) regions indicate states occupied by electrons (holes).

Figure 5-3 shows the evolution of the PL peaks as a function of reverse bias for different pump powers. At the lowest pump power, the single peak splits into two peaks at a reverse bias of approximately 8.2 V. As expected, the long wavelength peak originating from the cross-transition continuously shifts to longer wavelengths as the applied bias increases. The energy of this transition is a linear function of the applied field since the relative shift between these two levels has a linear field dependence (see Eqs. 4.10 and 4.13). An interesting effect is observed as the pump power is increased.

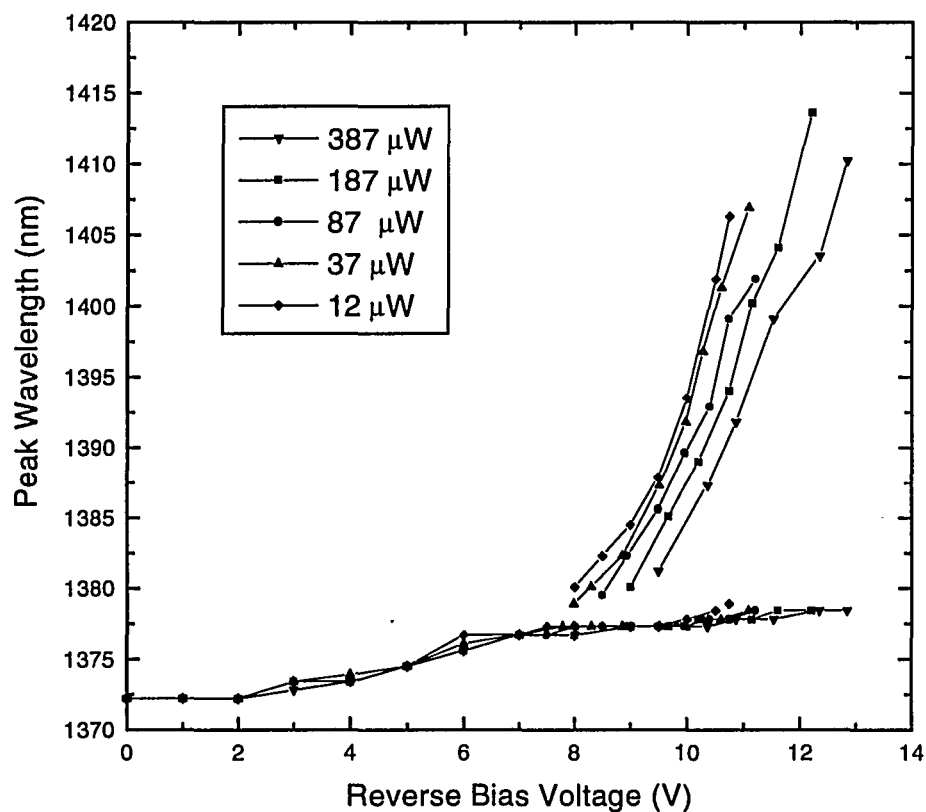


Figure 5-3 PL peak positions as a function of applied reverse bias for various pump intensities showing the effects of space-charge buildup.

For increased pump intensities, the bias voltage at which the cross-transition splits off increases due to the build-up of a space-charge field which screens the applied field. The space-charge field results from the spatial separation of electrons and holes localized in the narrow and wide wells, respectively.[56]

The results of the PL experiment demonstrate the ability to control the spatial location of photo-induced electrons in the (Ga,In)As/(Al,In)As ADQW structure through the use of an external bias. In the next section, an electro-optic modulator is described which takes advantage of the ability to control the spatial position of electrons to enhance the electro-optic properties of (Ga,In)As/(Al,In)As ADQWs at near-IR wavelengths.

5.2 Concept and Model

We designed an ADQW structure in which an excess conduction band electron density is intentionally formed by selectively doping the wide-well (WW) n-type as shown in Fig. 5-4(a). The presence of excess electrons bleaches the absorption near the bandedge of the WW. The lowest energy transition in the WW is thus given by

$$\hbar\omega = E_{\mu=0} + \mu_e(F) + E_1^v \quad (5.1)$$

where $E_{\mu=0}$ is the lowest energy WW transition in the absence of excess electrons, $\mu_e(F)$ is the field-dependent electron quasi-chemical potential with respect to the lowest allowed energy in the WW, and E_1^v is the in-plane hole energy required for momentum

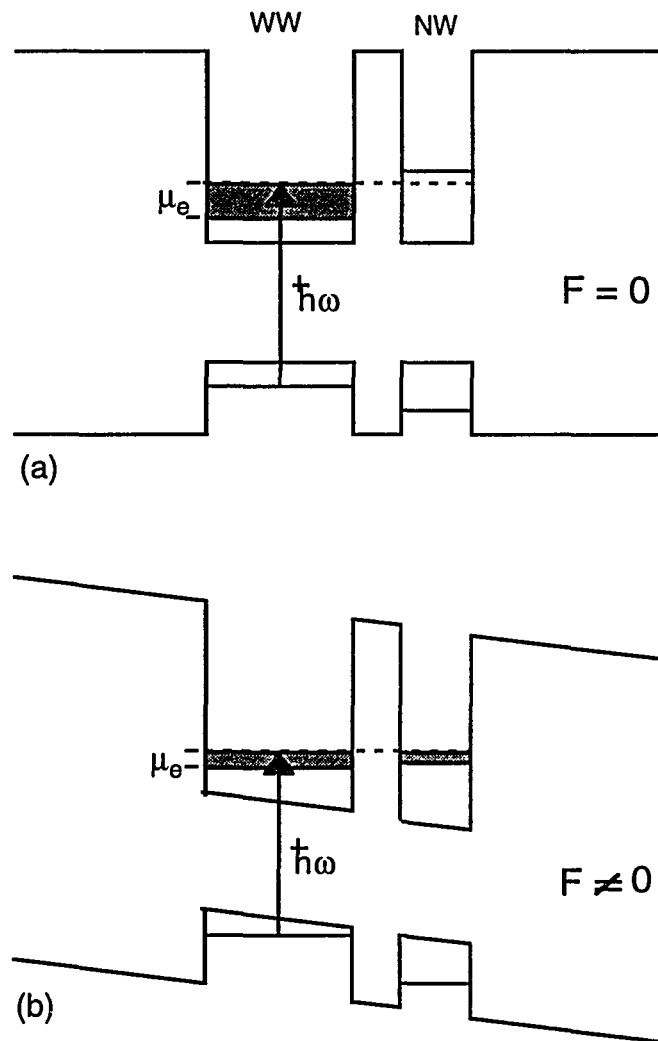


Figure 5-4 Conduction and valence band structure of the doped ADQW modulator in the (a) unbiased, $F = 0$ and (b) biased, $F \neq 0$ states. The shaded regions represent states occupied by excess electrons.

conservation. Hence, Eq. 5.1 indicates that the WW absorption edge will be blue-shifted with respect to the absorption edge in the absence of excess electrons, i.e. $\mu_e = 0$. An electric field applied perpendicular to the plane of the quantum wells will reduce the

energy separation between the lowest electron levels in the wide and narrow wells as shown in Fig. 5-4(b). As a result, the excess electrons localized in the WW can tunnel to the narrow well (NW) via real space electron transfer. The transfer of the electrons reduces μ_e resulting in the recovery of the absorption near the WW bandedge and causing an apparent red-shift of the WW absorption edge.

To investigate the effect of a one-component plasma on the absorption characteristics of an ADQW structure we calculated the field-dependent absorption coefficient near the band edge neglecting excitonic and renormalization effects. In the actual device (to be described in the next section), the WW was doped with Si to create the excess electron density. The presence of the ionized donors effectively inhibits the formation of any excitons. Additionally, bandgap renormalization is not expected to be dominant in these materials at the well widths used in this work.[3] Since the modulator uses the spatial transfer of doped electrons, the presence of the ionized donors must be included when calculating field dependent carrier densities in the wide and narrow wells. When the electrons transfer, a space-charge induced electric field is produced which screens the applied field as observed in the previous section. To model the space-charge effects in the doped ADQW structure, the space-charge was included in a simple self-consistent model. An accurate description must be derived from the self-consistent solution of the coupled Poisson and Schrödinger Equations. However, the simple model

presented here provides good insight into the electroabsorption performance of the doped ADQWs.

Upon the transfer of electrons, the resultant net charge distribution creates a space-charge induced potential shift between the first electron level in the WW and the first electron level in the NW. To obtain an estimate of the level shift, the charge distribution in each well (positive in the WW and negative in the NW) was assumed to be uniform. This assumption neglects the true distribution of electrons in the system given by the solution of Schrödinger's Equation. However, since the build-up of the space-charge induced potential relies on the integration of the charge distributions in each well as prescribed by Poisson's Equation, the assumption of uniform distributions in each well is justified. The net charge density in the WW and NW is

$$p = \frac{eN_{net}}{L_{ww}} \quad (5.2)$$

and

$$n = -\frac{eN_{net}}{L_{NW}} \quad (5.3)$$

respectively, where e is the electronic charge, N_{net} is the net charge density, and L_{WW} and L_{NW} are the wide and narrow well widths, respectively. After integrating the uniform charge distributions according to Poisson's Equation, the following expression for the space-charge induced level shift can be found:

$$\Delta E_{sc} = \frac{1}{2\kappa_o} (pL_{ww}^2 + nL_{NW}^2) + \frac{P}{\kappa_o} L_{ww} (L_{NW} + L_b) \quad (5.4)$$

where L_b is the barrier width separating the charge densities, and κ_o is the static dielectric constant of the material. The ordinary field-dependent energy levels of the wells were assumed to be of the form given by Eqs. 4.11 and 4.13. It is important to note that as the field is increased, the separation between the first levels of the WW and NW will decrease and electrons will transfer from the WW to the NW creating the space-charge distribution. The direction of the space-charge field screens the applied field since the positive charge is always present in the WW in the form of ionized donor atoms. As a result, the level separation is increased. Hence, the actual separation must be found self-consistently by including the “feedback” effect of the space-charge field.

The self-consistent computations followed a simple algorithm [57,58]:

- 1 Calculate the initial energy separation using Eq. 4.11
2. Allow the electron distribution of the system to equilibrate by distributing electrons between the wells such that the electron quasi-chemical potential in each well is the same at the given field and space-charge induced level shift.
3. Calculate the new induced level shift according to Eq. 5.4.
4. Calculate the new level separation according to

$$\Delta E = \omega \Delta E_{new} + (1 - \omega) \Delta E_{old}$$

where $\Delta E_{new} = \Delta E_{orig} + \Delta E_{sc}$, ω is the relaxation parameter for the feedback, and ΔE_{orig} is the separation found in step 1.

5. Repeat steps 2 through 4 until the separation, ΔE , stops changing to within the desired accuracy.

In a given subband of a quantum well structure, the density of states is constant, and thus, the electron quasi-chemical potential can be found by directly integrating

$$n = \frac{m^*}{\pi \hbar^2} \int_0^{\infty} \left[\frac{1}{1 + \exp\left(\frac{E - \mu_e}{kT}\right)} \right] dE \quad (5.5)$$

to obtain the following expression for the electron quasi-chemical potential relative to the system energy zero:

$$\mu_e = kT \ln \left[\exp\left(\frac{n\pi \hbar^2}{m^* kT}\right) - 1 \right] + E_n \quad (5.6)$$

where k is Boltzmann's constant, m^* is the electron effective mass, T is the temperature, n is the two dimensional electron density, E_n is the bound state energy of the electron level in question, and μ_e is the electron Fermi-level. Equation 5.6 was used in step 2 above to obtain an equilibrium electron distribution between the wells.

To demonstrate the calculations described, the field dependence of electron levels in a 40/35/70 ADQW structure were analyzed. This structure was used to demonstrate real-space electron transfer in the previous section. The field-dependent energy separation between the first energy levels in the WW and NW of the 40/35/70 ADQW structure is shown in Fig. 5-5 for various carrier densities. It is assumed that the holes (positive charge) stay in the WW at all fields. At carrier densities less than $1 \times 10^{10} \text{ cm}^{-2}$

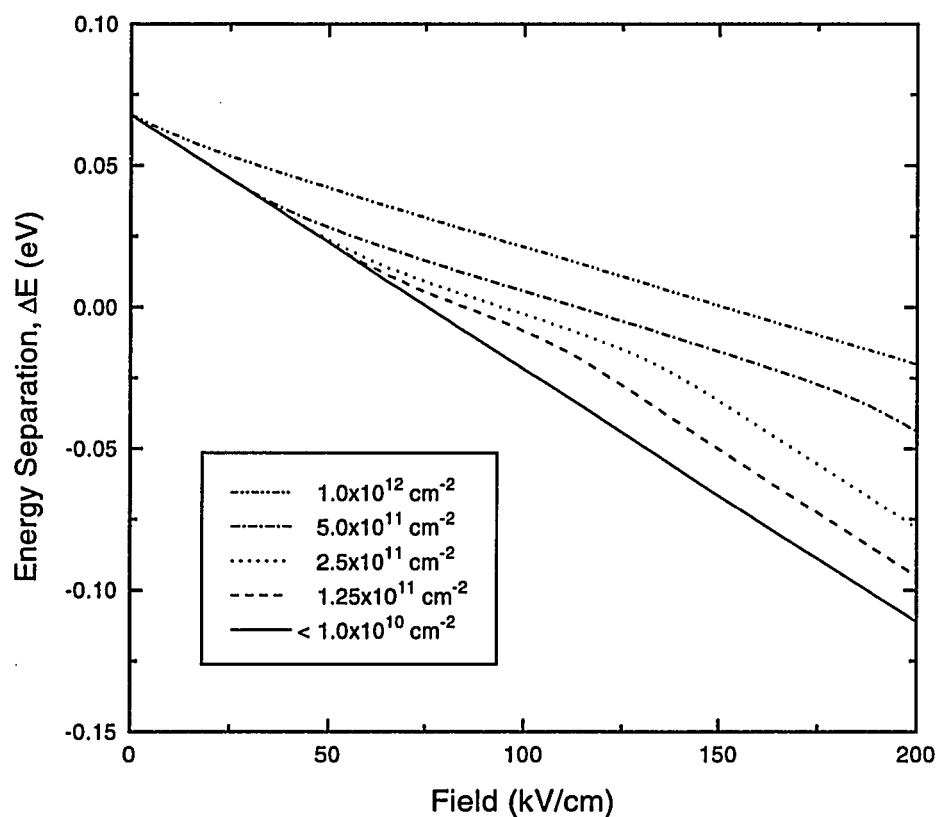


Figure 5-5 Field dependence of the energy separation between the first electron levels in the WW and NW for different carrier densities. The temperature is 50 K.

the separation is a linear function of the applied field. As the carrier density is increased, however, the rate at which the separation decreases is reduced. The range of field values over which the rate is reduced increases as the carrier density is increased. The reduction is due to the build-up of the space-charge field which screens the applied field. At a carrier density of $1 \times 10^{12} \text{ cm}^{-2}$ the rate is reduced over the entire range of fields considered.

Figure 5-5 illustrates the importance of including space-charge effects in the calculation of the field-dependent energy level positions. Figure 5-6 shows the field-dependence of

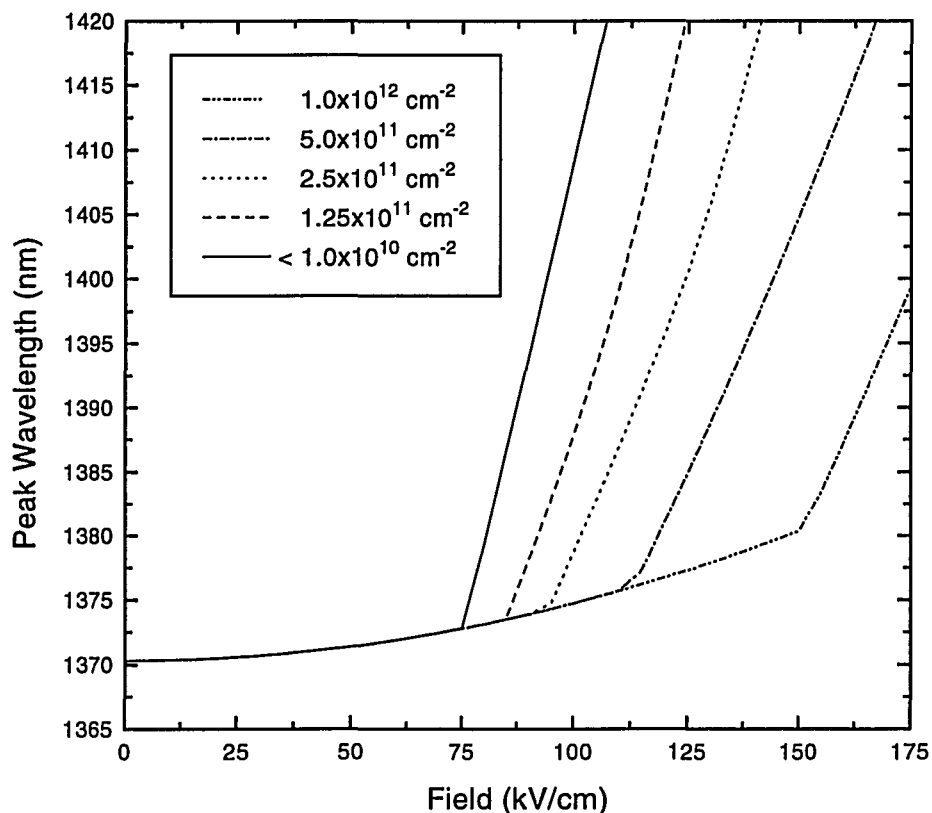


Figure 5-6 Minimum energy transition in the 40/35/70 ADQW structure as a function of applied field for various carrier densities. The temperature is 50 K.

the lowest energy transition in the 40/35/70 ADQW system. The data shown are equivalent to the experimental data presented in Fig. 5-3. As the field increases, the transition shifts to longer wavelengths. At the resonance field, the cross transition between the WW and NW becomes dominant resulting in a shift which is linear with applied field. The field at which the cross-transition splits-off is dependent on the carrier density induced screening of the applied field. The theoretical results presented in Fig. 5-6 are in good qualitative agreement with the experimental results shown in Fig. 5-3. The

results cannot be compared on a quantitative level due to the simplicity of the model used. The assumption of uniform distributions isolated in each well neglects the penetration of the respective wavefunctions into the adjacent wells as the field is increased. The delocalization will tend to decrease the magnitude of the space-charge induced field. As a result, the fields required to obtain resonance conditions are most likely over-estimated by the simple model used. Nonetheless, the model is useful for predicting the qualitative field-dependent behavior of ADQW systems in the presence of high carrier densities.

The above model was applied to a 50/35/70 ADQW structure to investigate the effect of an excess electron density on the band edge absorption as a function of applied field. The ADQW structure was assumed to have the WW doped with $1 \times 10^{12} \text{ cm}^{-2}$ ionized donors (Si atoms) and the system temperature was assumed to be 50 K. The electron densities in the WW (solid lines) and NW (dashed lines) as a function of applied field are shown in Fig. 5-7. At this donor density, the WW and NW electron densities are linearly dependent on the applied field. As the field is increased the electron density in the WW decreases while the electron density in the NW increases. These results are consistent with the transfer of excess electrons from the WW to the NW. For lower donor densities (as shown in the figure) complete charge transfer occurs over a smaller range of applied biases. Additionally, the field at which the WW and NW electron densities are equal occurs

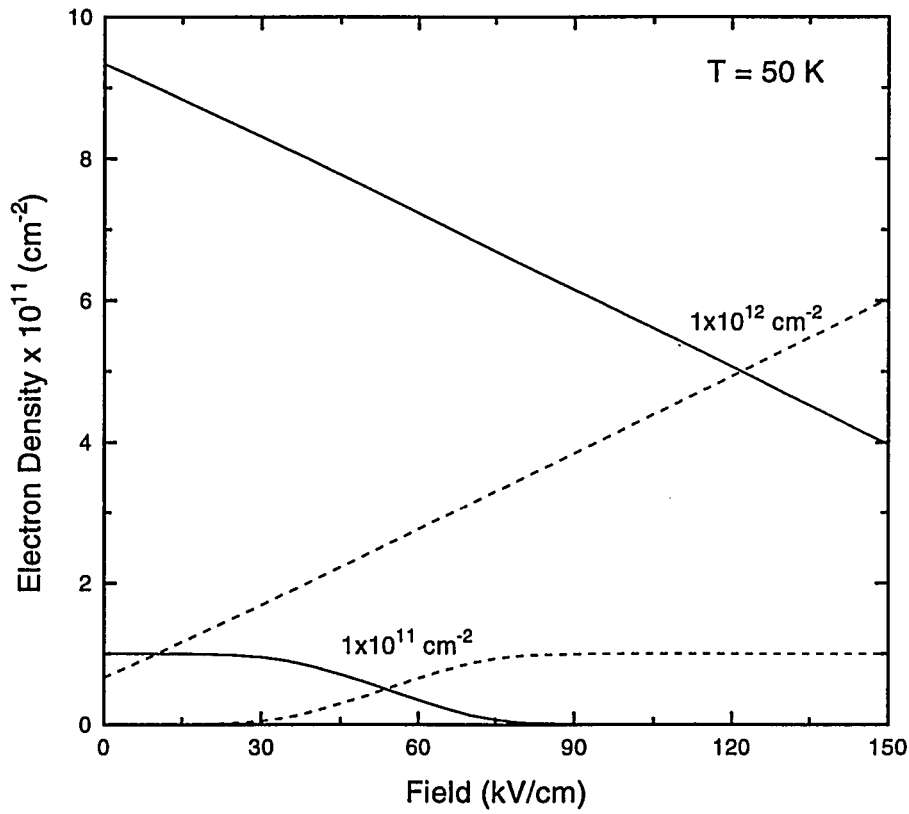


Figure 5-7 Electron density of the WW (solid lines) and NW (dashed lines) as a function of applied field at doping densities of 1×10^{12} and 1×10^{11} cm^{-2} . The temperature is 50 K.

at a much lower field than in the high density case, again illustrating the effects of space-charge build-up in ADQW structures.

The field-dependent electron densities were used to calculate the free-carrier absorption spectra at various applied fields. The ordinary bandfilling factor

$$A(\omega) = 1 - f_c(\omega, T) - f_h(\omega, T) \quad (5.6)$$

was replaced by a bandfilling factor which only included the electron term, i.e.

$$A'(\omega) = 1 - f_c(\omega, T) \quad (5.7)$$

The band edge spectrum was also convolved with a Lorentzian line shape to smooth the step-function band edge absorption spectrum of ideal free-carrier transitions in quantum well structures. The calculated absorption spectra of the 50/35/70 ADQW structure at several applied fields are shown in Fig. 5-8. At zero field, the WW absorption is completely bleached to wavelengths approaching the NW band edge. As the field is increased, the WW absorption recovers while the NW band edge becomes increasingly

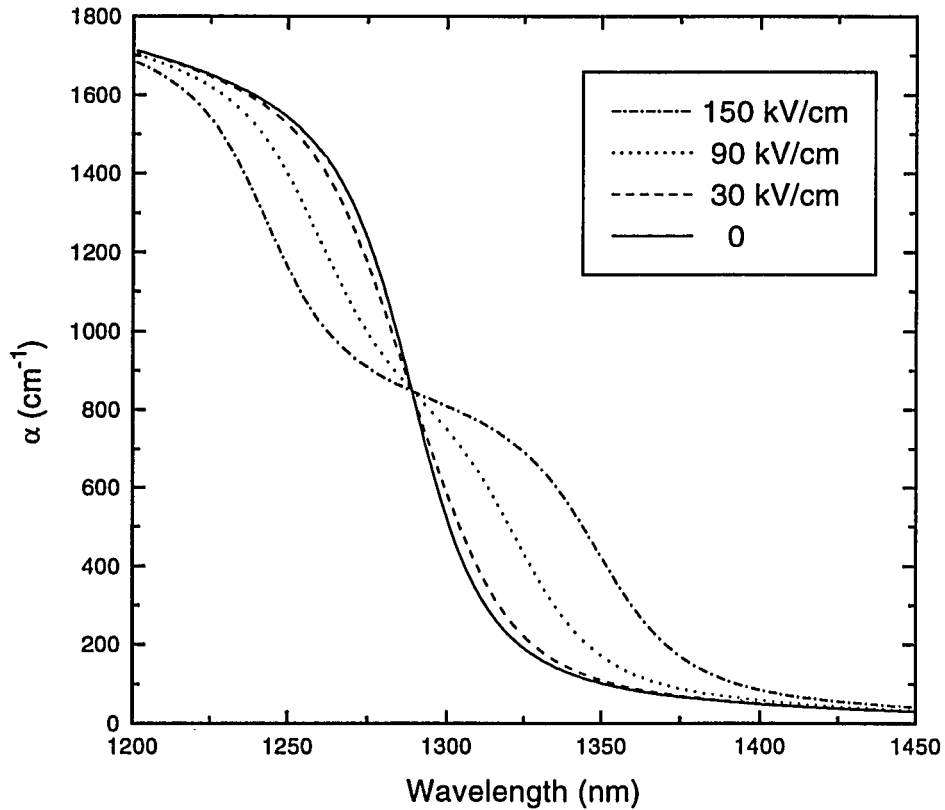


Figure 5-8 Calculated free-carrier absorption spectra of the 50/35/70 ADQW structure at various applied fields. The WW was assumed to be doped with $1 \times 10^{12} \text{ cm}^{-2}$ donors and the sample temperature was assumed to be 50 K.

bleached. At a field of 150 kV/cm large absorption changes have been achieved with only slightly more than half of the excess electrons transferred to the NW (see Fig. 5-7). The apparent shift of the WW band edge, taken as the shift in the peak of the $\Delta\alpha$ spectrum as a function of applied field, is shown in Fig. 5-9 (where $\Delta\alpha = \alpha(F) - \alpha(F = 0)$ and F is the applied field). Also shown in the figure is the shift of the band edge due to only the QCSE. The shift of the band edge for the doped structure is much larger with increasing field as a result of efficient electron transfer between the wells.

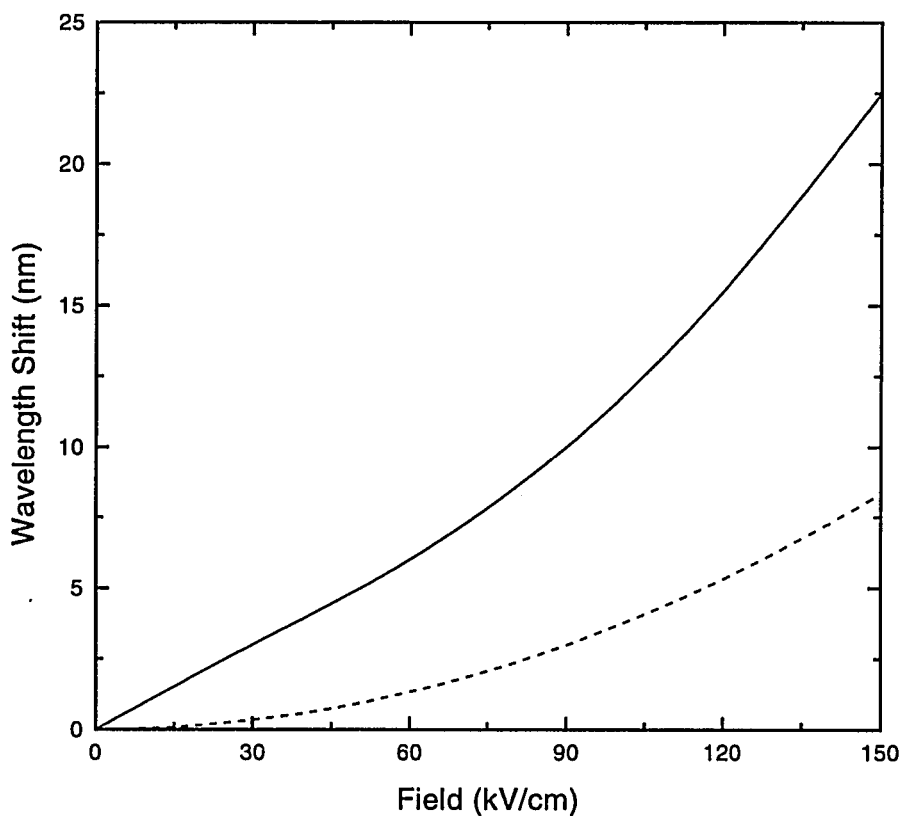


Figure 5-9 Apparent shift of the WW band edge for the doped 50/35/70 ADQW structure (solid line) as a function of applied field. The shift due to the QCSE is also shown (dashed line).

In summary, a simple self-consistent model of electron transfer in ADQW structures has been presented. The model was used to predict the electroabsorptive properties of an ADQW structure in which the WW was doped with excess electrons. The model showed that large field-dependent absorption changes can be achieved due to real-space transfer of excess electrons between the wide and narrow wells.

5.3 Low Temperature Results

To experimentally demonstrate the enhanced electroabsorption properties discussed in the last section, the doped 50/35/70 ADQW structure was grown by molecular beam epitaxy on n-type (100) InP substrates. The electrical bias was applied via an *n-i-n* diode consisting of a 0.35 μm layer of n-type $\text{Ga}_{0.3}\text{Al}_{0.18}\text{In}_{0.52}\text{As}$ (Si, $2 \times 10^{18} \text{ cm}^{-3}$) followed by a 0.865 μm intrinsic region and capped with a 0.2 μm layer of n-type $\text{Ga}_{0.3}\text{Al}_{0.18}\text{In}_{0.52}\text{As}$ (Si, $2 \times 10^{18} \text{ cm}^{-3}$). The intrinsic region consisted of 30 periods of 100 \AA $\text{Al}_{0.48}\text{In}_{0.52}\text{As}$ barrier/ 70 \AA $\text{Ga}_{0.47}\text{In}_{0.53}\text{As}$ wide well doped n-type over the central 40 \AA (Si, $1 \times 10^{12} \text{ cm}^{-2}$)/ 35 \AA $\text{Al}_{0.48}\text{In}_{0.52}\text{As}$ tunnel barrier/ 50 \AA $\text{Ga}_{0.47}\text{In}_{0.53}\text{As}$ narrow well all between two layers of 500 \AA undoped $\text{Al}_{0.48}\text{In}_{0.52}\text{As}$. The diodes were processed into 150 μm diameter mesa diodes with ring top contacts to allow optical transmission experiments (see Section 4.1 for a description of the transmission spectroscopy system).

The modulator sample was mounted in a closed-cycle helium cryostat and held at a temperature of 50 K.

The measured absorbance spectra at bias fields of 0 and 74 kV/cm, corresponding to applied voltages of 0 and 6.4 V, respectively, are shown in Fig 5-10. The peaks in the zero-field spectrum are the light- and heavy-hole excitonic absorption features associated with the lowest energy transition in the NW. The excitonic features associated with the WW, however, are completely bleached by the presence of the excess electron density. In fact, due to bandfilling in the first WW electron subband, the WW

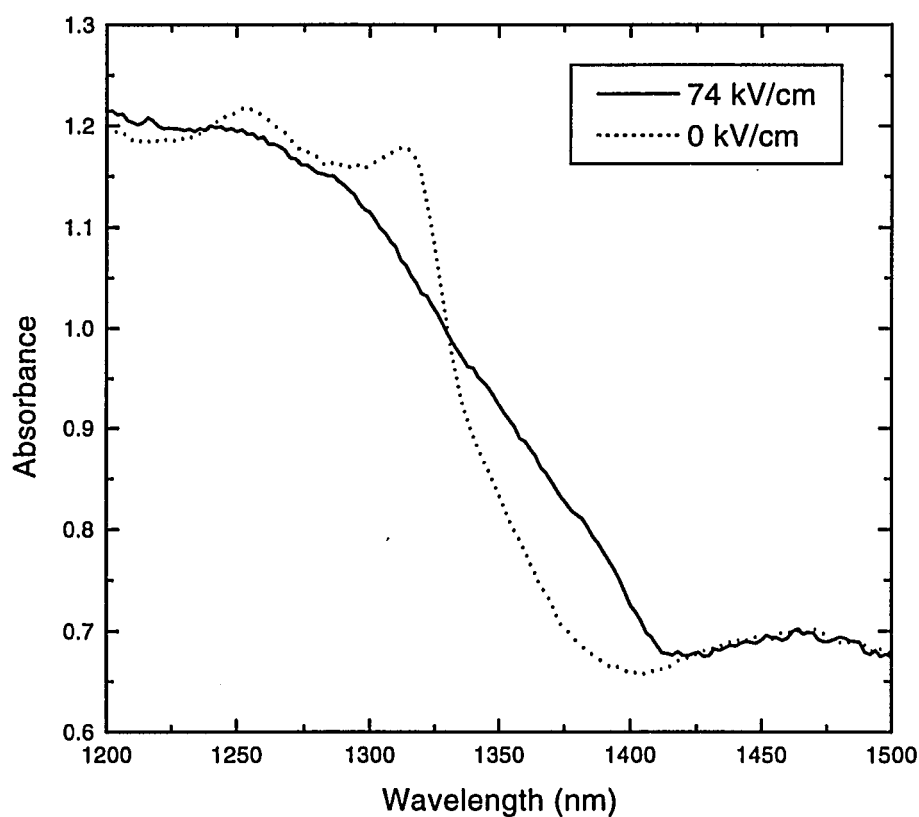


Figure 5-10 Measured absorbance spectra of the doped modulator for applied fields of 0 and 74 kV/cm.

absorption is bleached to wavelengths approaching the NW bandedge. With the applied field present, the absorption associated with the WW recovers while the absorption associated with the NW becomes bleached. It should be stressed that the observed changes are not due to the QCSE. In undoped (Ga,In)As/(Al,In)As coupled quantum well systems consisting of similar well widths, excitonic absorption features persist to much higher applied fields than those considered in this work.[24] Hence, the observed absorption changes can only arise from the real-space transfer of electrons from the WW to the NW.

To further investigate the electron densities in both the WW and NW, we measured the 50 K photoluminescence (PL) spectra at different applied fields (see Fig. 5-12). The sample was pumped by a continuous wave, 1.319 μm Nd:YAG laser. Since both the wide and narrow wells are excited, low pump power was used to avoid bandfilling effects in the NW. The maximum pump power incident on the sample surface was approximately 8 mW. At zero applied field the peak of the PL spectrum occurs at a wavelength of 1390 nm. The PL maximum is Stokes shifted by approximately 46.3 meV from the onset of WW absorption in the absence of applied field, corresponding to an electron density of $8.6 \times 10^{11} \text{ cm}^{-2}$ in the WW.[59] The observed shift indicates that an excess electron density of approximately $1.4 \times 10^{11} \text{ cm}^{-2}$ resides in the NW at zero bias, consistent with the weak and broadened NW excitonic features shown in Fig. 5-10. These carrier densities are in good agreement with the results of our simple model. At zero field,

the model predicts that $9.3 \times 10^{11} \text{ cm}^{-2}$ electrons should be in the WW and $0.7 \times 10^{11} \text{ cm}^{-2}$ electrons should be in the NW. The shift reduces to 11.5 meV at an applied field of 74 kV/cm. The reduction of the Stokes shift in the presence of the applied field indicates that an electron concentration of $5.4 \times 10^{11} \text{ cm}^{-2}$ has been transferred from the WW to the NW resulting in the complete bleaching of the NW light- and heavy-hole excitonic features. As shown in Fig. 5-11, the FWHM width of the WW PL emission spectrum shows a corresponding decrease with increasing field. The reduction in width is the result of a red-shift of the short wavelength side of the PL spectrum (see Fig. 5-12).

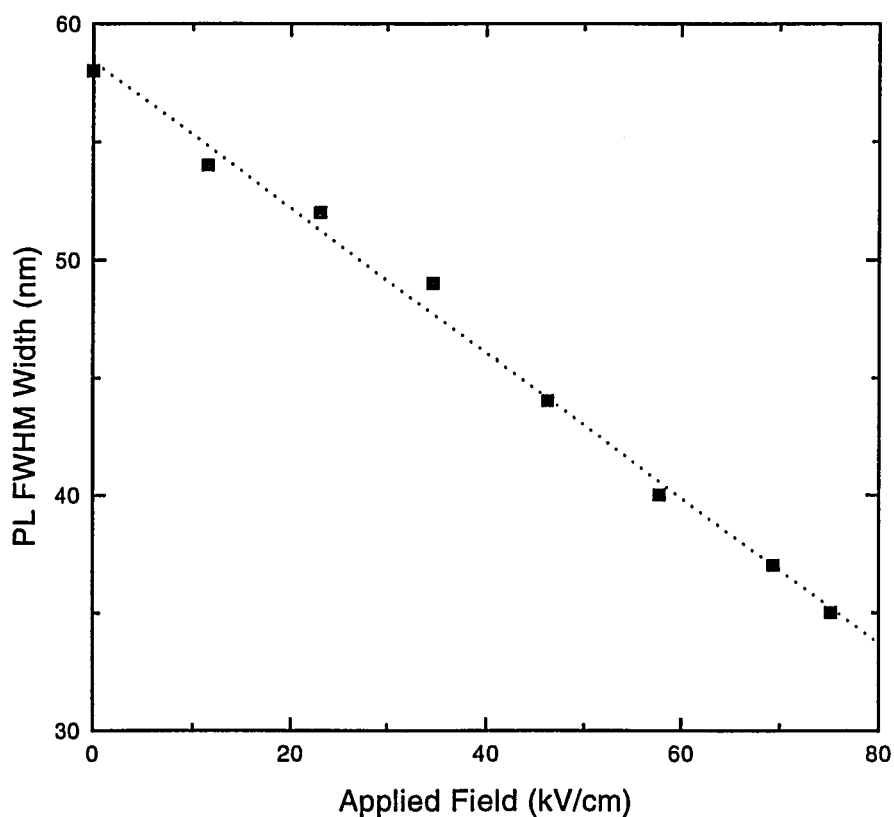


Figure 5-11 Measured decrease in the PL FWHM width as a function of applied field. The dotted line is a linear fit to the measured data.

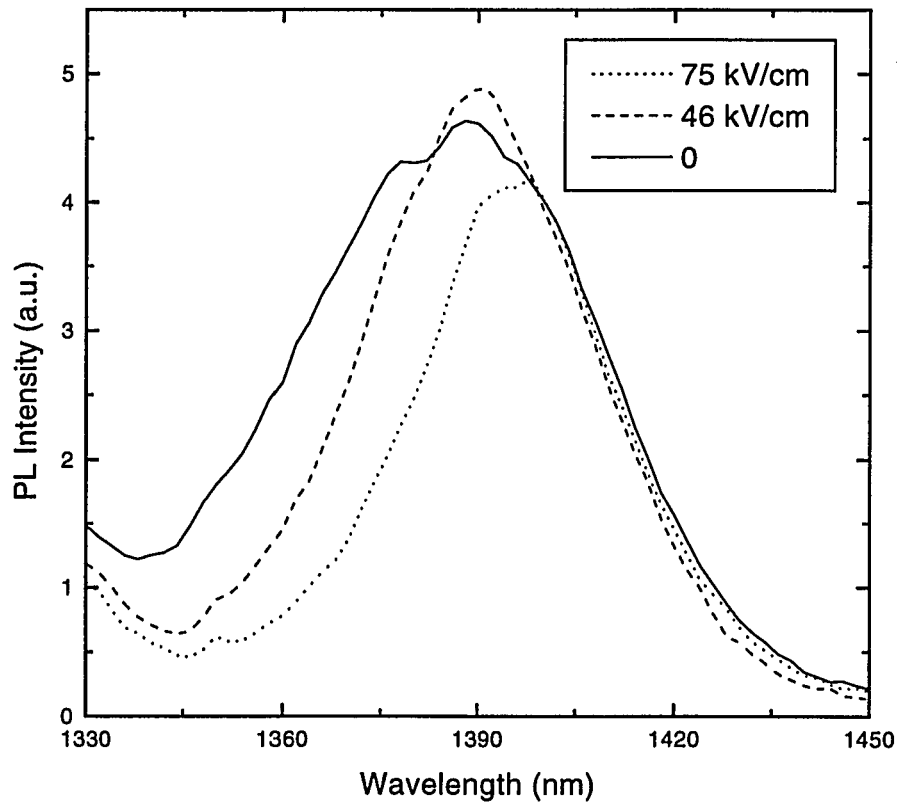


Figure 5-12 Measured PL emission spectrum showing the red shift of the short-wavelength edge with increasing applied field.

This shift corresponds to a decrease in the electron quasi-chemical potential energy with respect to the lowest allowed energy in the WW indicating that electrons are indeed being transferred from the wide to narrow well. The long wavelength edge, however, shows no shift with increasing field since real space transfer of electrons occupying these states is energetically forbidden.

The characteristics of the doped modulator were compared to the electroabsorption characteristics of the undoped 40/35/70 ADQW sample described in

Chapter 4. Since the 35 Å tunnel barrier is relatively thick, the WW and NW are essentially uncoupled for the range of applied fields considered here. Hence, the change in the WW absorption with applied field is strictly due to the QCSE. Figure 5-13 shows the field-dependent absorption spectra of the undoped sample at a temperature of 50 K. To accurately compare the two modulators, the built-in potential of the *p-i-n* diode must be included in the total applied field for the undoped sample. The built-in potential was determined to be -1.63 V at 50 K by using a photovoltage technique.[60] In the photovoltage technique, electrons and holes are generated above the intrinsic region

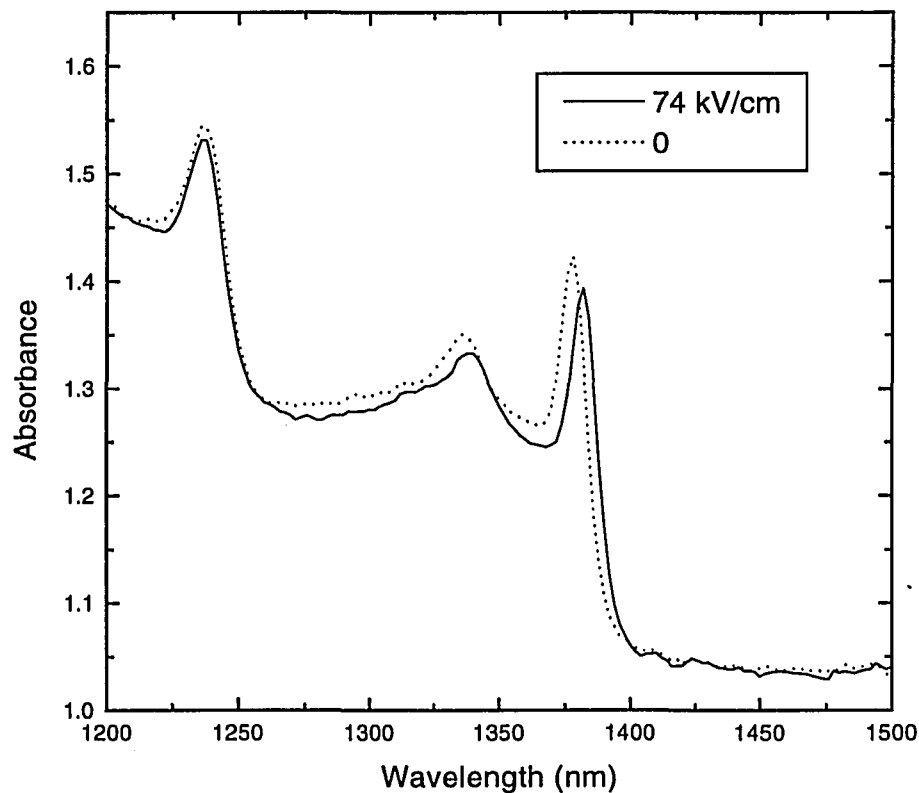


Figure 5-13 Measured absorbance spectra of the undoped 40/35/70 ADQW structure at applied fields of 0 and 74 kV/cm.

bandgap by an argon-ion laser. Due to the presence of the built-in potential, the photogenerated electrons and holes are swept to the *n*- and *p*-sides of the diode, respectively. The carriers accumulate at opposite sides of the diode since the diode is left in the open-circuit configuration. The excess charge generates a space-charge field which self-consistently screens the built-in potential. The accumulation of carriers stops when the photo-induced potential is equal and opposite to the built-in potential of the diode, i.e. further increase in the laser power does not increase the measured photovoltage. The depletion region width of both diodes was assumed to be equal to the corresponding intrinsic region width. Figure 5-14 shows the red-shift of the bandedge as a function of applied field for both the doped (solid squares) and undoped (open squares) modulators. The red-shift was measured as the shift of the WW heavy-hole exciton absorption resonance for the undoped sample and as the shift of the peak in the $\Delta\alpha L$ spectra for the doped sample. The red-shift of the bandedge for the undoped sample is quadratic with increasing field as expected from the QCSE. However, the red-shift of the band edge exhibited by the doped sample is much larger with increasing field and has an almost linear field dependence. In fact, for an applied field of approximately 50 kV/cm (corresponding to an applied voltage of only 4.3 V) the red-shift of the doped sample is more than six times larger than the red-shift of the undoped sample. The shift of the absorption edge of the doped sample follows the red-shift of the short wavelength PL emission edge (open triangles in Fig. 5-14) since both are dependent on the position of the

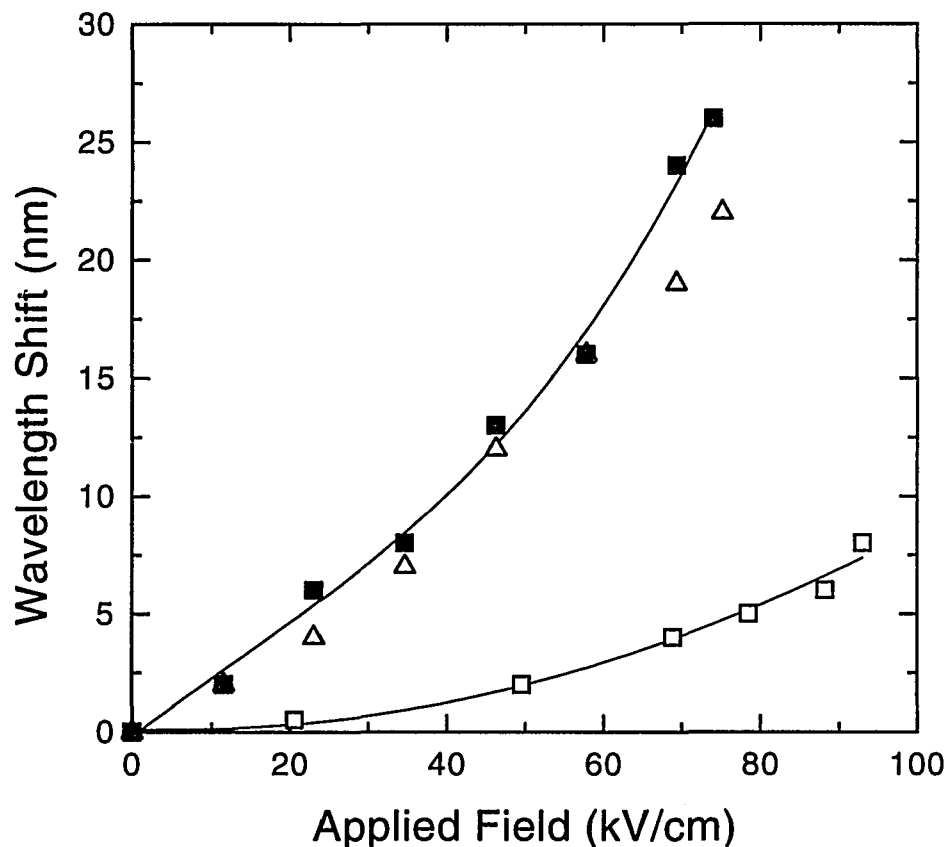


Figure 5-14 Comparison of the band edge shift for the doped (solid squares) and undoped (open squares) ADQW structures. The solid lines are fits to the measured data. The red shift of the short-wavelength PL edge is also shown (open triangles).

electron quasi-chemical potential with respect to the lowest allowed energy in the WW.

The overall qualitative agreement between the experimental data presented in Fig. 5-14 and the theoretical predictions presented in Fig. 5-9 is good except for the slope of the shift vs. field curve for the doped modulator. The slope derived from the experiment is higher than the slope predicted from our self-consistent model. The difference is most likely caused by not included the penetration of the electron wavefunctions into adjacent

wells. Hence, our model over estimates the space-charge field which results in a lower electron transfer rate with increasing field.

5.4 Room Temperature Results

Although the modulator described in the previous section demonstrated enhanced performance over a structure which utilized only the QCSE, the device was operated at a temperature of 50 K. Obviously, for the doped structure to compete with existing technologies room temperature operation must be obtained.

The large absorption changes observed at low temperatures are predicted to persist even at room temperature. Figure 5-15 shows the calculated field-dependence of the 50/35/70 ADQW absorption spectrum at a temperature of 300 K. As before, the WW was assumed to be doped with $1 \times 10^{12} \text{ cm}^{-2}$ donors. The spectra again show the effect of efficient electron transfer between the wells, i.e. as the field is increased the WW absorption recovers while the NW absorption becomes bleached. Although our model predicts that large absorption changes are possible, the model assumes that the diode used to apply the external field will also perform optimally at room temperature. The diode consists of a *n-i-n* structure as opposed to a *p-i-n* structure. The *n-i-n* diode allows both forward and reverse biases to be applied to the structure. A *p-i-n* diode only allows the application of large reverse biases. The application of even relatively small

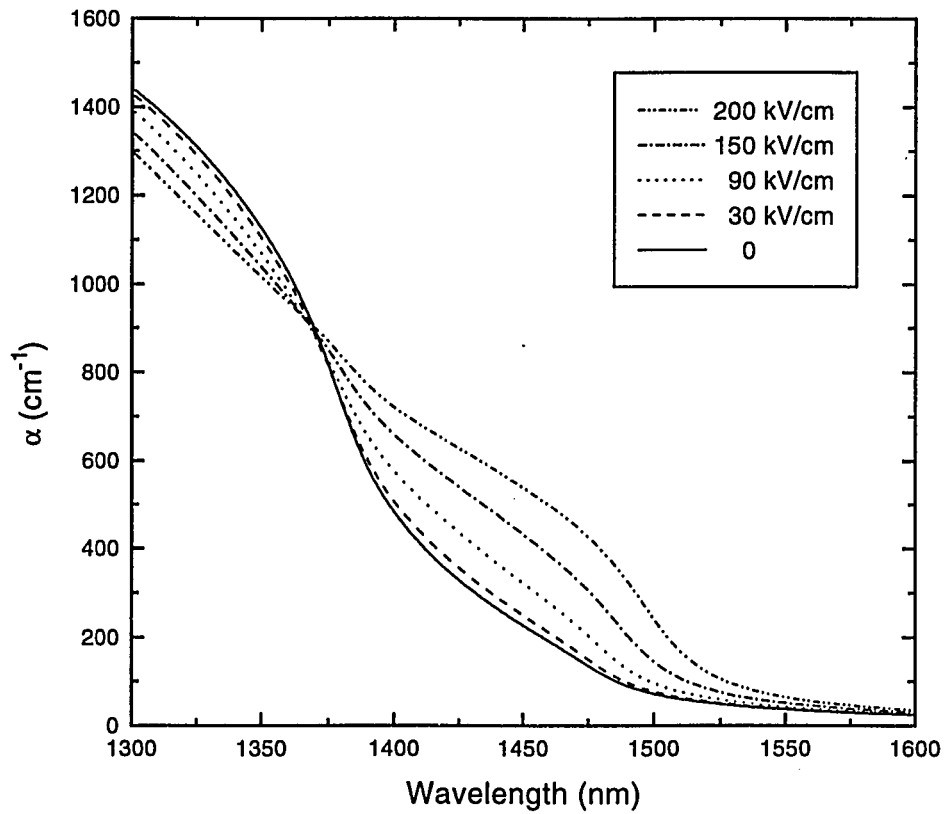


Figure 5-15 Calculated free-carrier absorption spectra of the 50/35/70 ADQW structure at various applied fields. The WW was assumed to be doped with $1 \times 10^{12} \text{ cm}^{-2}$ donors and the sample temperature was assumed to be 300 K.

forward biases (typically 1 V) result in significant current flow through the diode limiting the magnitude of the forward bias that can be applied. The symmetric structure of *n-i-n* diodes, on the other hand, leads to an anti-symmetric I-V characteristic, i.e. the breakdown voltages are the same for both forward and reverse biases with current flowing

in opposite directions. However, since *n-i-n* diodes are monopolar devices, they suffer from increased current leakage at high applied biases.

The degradation of the *n-i-n* diode at room temperature limits the use of the present modulator to low temperatures. As shown in Fig. 5-16, at a temperature of 50 K the maximum bias voltage which can be applied is approximately -6.5 V, corresponding to an applied field of 75 kV/cm. At room temperature, the maximum bias voltage is limited to approximately -4.0 V corresponding to an applied field of only 45 kV/cm. The current at high biases arises from primarily three sources: tunneling of electrons out of the

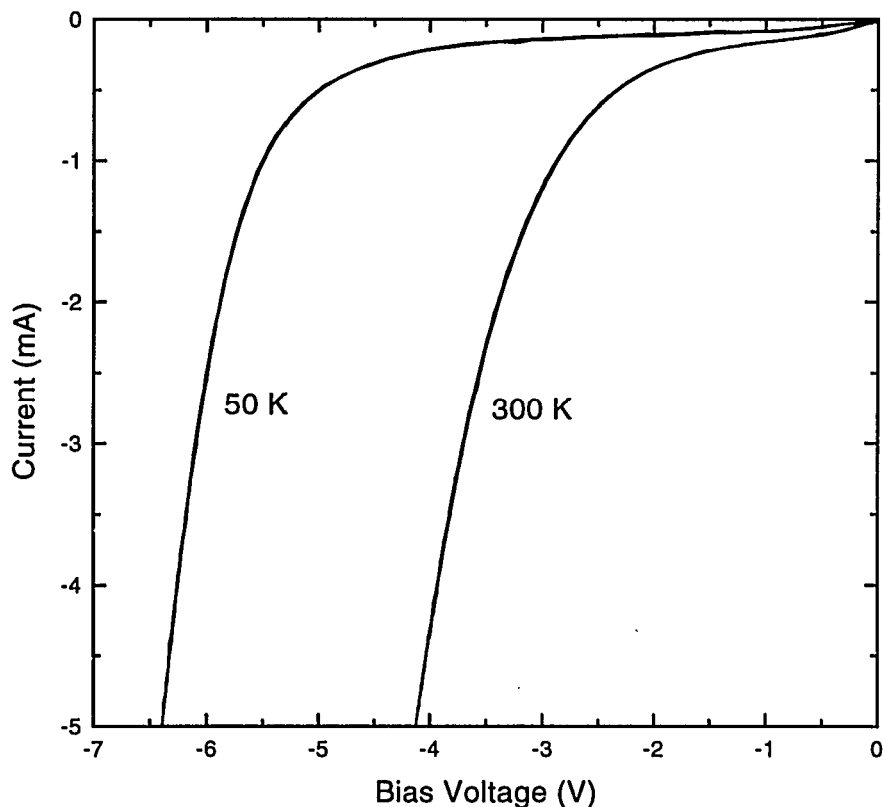


Figure 5-16 Measured I-V characteristic of the *n-i-n* diode used to apply the external field for the doped ADQW structure at temperatures of 50 and 300 K.

ADQW structure, thermionic emission of electrons over the ADQW barrier layers, and leakage current through the diode. Of the three sources, leakage current through the *n-i-n* diode is the most likely cause of the breakdown at room and low temperature. Thermionic emission is also a contributing factor at room temperature.[61]

A new diode design is currently being investigated which uses a *p*-type delta-doped barrier with *n*-type superlattice between ADQW periods as shown in Fig. 5-17. Similar structures have been used by Wegener, et al. to inhibit current flow at room temperature in *n-i-n* diode structures.[28] The doped superlattice helps to ensure that the field across each ADQW period is equal and uniform. The delta-doped *p*-type region increases the potential barrier height for electrons. The result is an increase in the applied field at which breakdown occurs.

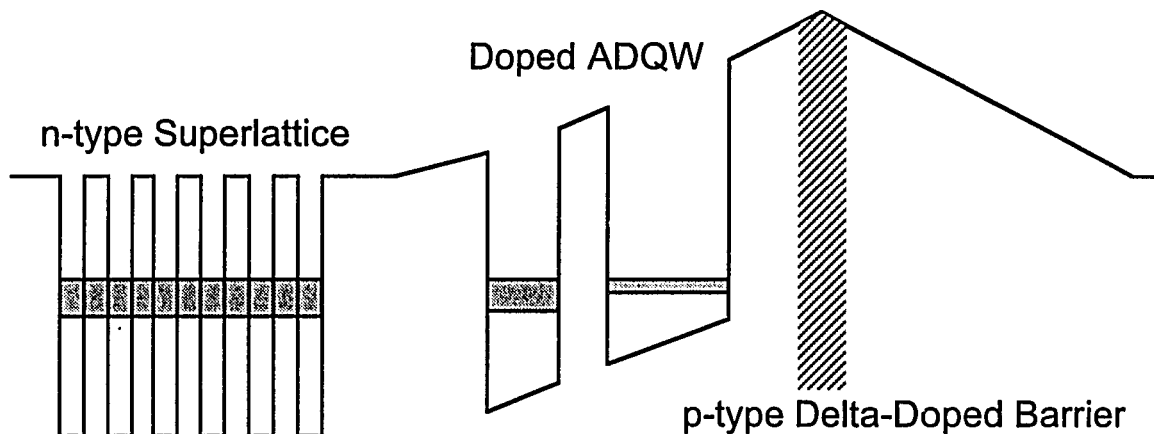


Figure 5-17 Schematic diagram of a ADQW period with *n*-type superlattice and *p*-type delta-doped barrier to suppress current flow. Only the conduction band profile is shown.

A new *n-i-n* diode/ADQW modulator was designed using 10 periods of the structure shown in Fig. 5-17. The *n-i-n* diode structure itself has remained the same as described in the previous section. The intrinsic region now consists of 10 periods of 75 Å undoped Al_{0.48}In_{0.52}As barrier followed by a six period n-type 20 Å Ga_{0.47}In_{0.53}As/25 Å Al_{0.48}In_{0.52}As superlattice (Si, 1x10¹⁸ cm⁻³), another 75 Å undoped Al_{0.48}In_{0.52}As barrier followed by a 50 Å Ga_{0.47}In_{0.53}As narrow well doped n-type over the central 25 Å (Si, 1x10¹² cm⁻²)/ 35 Å Al_{0.48}In_{0.52}As tunnel barrier/ 70 Å Ga_{0.47}In_{0.53}As wide well, followed by 70 Å undoped Al_{0.48}In_{0.52}As and 30 Å p-type Al_{0.48}In_{0.52}As (Be, 3x10¹⁸ cm⁻³) barrier layer all between two layers of 500 Å undoped Al_{0.48}In_{0.52}As. The device is currently in the process of being fabricated by MBE and photolithographic techniques. Once the device is fabricated the room temperature optical and electrical characteristics will be investigated using the techniques described in this chapter. If the modulator performs well at room temperature, the results will be published in the technical literature.

5.5 Summary

In conclusion, we have demonstrated a novel electroabsorption mechanism based on selective doping in ADQW structures. The modulator utilizes real space electron transfer to provide efficient absorption modulation. The electron concentration in both the wide and narrow wells was investigated using field dependent absorption and

photoluminescence spectroscopy. The doped modulator exhibits a significantly larger red-shift with applied field than an undoped structure which utilizes the QCSE. Efforts are currently underway to optimize the coupled quantum well design and diode structure for room-temperature operation.

CHAPTER 6

SUMMARY AND SUGGESTIONS FOR FUTURE RESEARCH

6.1 Summary

In this dissertation, a research program consisting of three phases has been presented. The three phases of the research were:

- 1) The design, fabrication, and testing of an all-optical, high-contrast asymmetric Fabry-Perot reflection modulator for use at the optical fiber compatible wavelength of 1.3 μm (see Reference 34).
- 2) The investigation of ultrafast carrier dynamics in (Ga,In)As/(Al,In)As asymmetric double quantum wells (ADQWs).
- 3) The design and demonstration of a novel electroabsorption modulator which utilized the real-space transfer of excess electrons in (Ga,In)As/(Al,In)As ADQWs.

In the first phase, we demonstrated the first all-optical GaAlInAs/AlInAs multiple quantum well asymmetric reflection modulator for operation at 1.3 μm . By using the combined absorptive and refractive nonlinearities associated with saturating the heavy-hole exciton resonance, an on/off contrast ratio exceeding 30 dB and an insertion

loss of 2.2 dB has been achieved. The modulator was demonstrated to have an operating bandwidth of 5 nm and a speed approaching 1 GHz

Although the modulator was demonstrated to have excellent performance characteristics in terms of contrast ratio and insertion loss, the operating speed of the device was limited by the recombination time of the electrons and holes in the spacer material. An additional limitation of the modulator is that, even for low-speed applications, the device relies on optical control. The remaining two phases of this dissertation addressed the lifetime and control signal limitations of the modulator.

In the second phase, carrier dynamics in (Ga,In)As/(Al,In)As ADQWs were investigated using a novel femtosecond, up-conversion pump/probe technique. We found that at low carrier densities both electrons and holes can tunnel from the wide well (WW) to the narrow well (NW) with at least picosecond speeds. In particular, due to the non-degenerate nature of the experiment, holes were found to tunnel to the WW to NW before relaxing to the bottom of the NW. The fast electron tunneling was verified to be a LO-phonon assisted process as expected from previous work performed with GaAs/(Ga,Al)As ADQWs. The fast hole tunneling was found to be due to scattering from the randomly fluctuating alloy potential of the ternary materials used. Impurity scattering was also considered, however, the hole tunneling times were found to be two orders-of-magnitude greater than the alloy assisted times. The fast dynamics observed in

these materials may make them useful for applications such as the asymmetric reflection modulator discussed above.

The final phase of the research concentrated on a novel electroabsorption mechanism in selectively doped (Ga,In)As/(Al,In)As ADQWs. Real-space transfer of excess electrons was demonstrated in an undoped ADQW structure using low-temperature photoluminescence (PL) spectroscopy. The results of these measurements confirmed the principle of utilizing the spatial transfer of excess electrons to enhance the electro-optic properties of ternary materials used for optical fiber based applications. The concept of the real-space electron transfer modulator was then described and a simple self-consistent model was used to predict the electroabsorption properties of the structure. The electron concentration in both the wide and narrow wells of the doped ADQW structure was investigated using field dependent absorption and PL spectroscopy. The doped modulator was found to exhibit a significantly larger red-shift with applied field than an undoped structure which utilized the quantum confined Stark effect.

Novel work presented in this dissertation includes:

- 1) The first demonstration of an all-optical asymmetric reflection modulator for use at 1.3 μm .
- 2) The modulator exhibited an on/off contrast ratio exceeding 30 dB, the highest contrast ratio measured to date for an all-optical device.

- 3) The first femtosecond study of electron and hole dynamics in (Ga,In)As/(Al,In)As ADQWs using a novel non-degenerate pump/probe technique.
- 4) The first experimental observation with supporting theory of subpicosecond hole tunneling in ADQWs.
- 5) The first demonstration of real-space electron transfer in (Ga,In)As/(Al,In)As ADQWs to enhance the electroabsorption properties of optical fiber compatible semiconductor heterostructure materials.

6.2 Suggestions for Future Research

There are several issues concerning the research presented which should be addressed but were not included in this dissertation due to time constraints.

To gain a better understanding of the electron and hole dynamics in the ternary ADQW structures further time-resolved experimentation is required. In particular, the dynamics of the electrons and holes should be investigated at low temperatures when pumped and probed degenerately. The experimental results would verify that holes tunnel rapidly only when they are generated away from the Γ -point. Currently, a new laser system (a Kerr lens modelocked Cr:Forsterite laser) is being developed to perform these experiments. Additional information could also be gained about the long-lasting

components by performing low-temperature, intensity-dependent PL spectroscopy. Finally, a more accurate model of the ADQW valence band structure (obtained by solving the 8x8 Kane Hamiltonian) and more sophisticated models of the temporal processes (Monte Carlo methods) must be developed to gain a full understanding of the hole dynamics in these structures.

For the further development of the selectively doped ADQW modulator structure, the primary goal is to design a *n-i-n* diode structure which suppresses current flow over the range of bias voltages required for room temperature device operation. Advances in the diode design are currently being made. We have designed a new diode structure which utilizes a *p*-type delta-doped barrier with *n*-type superlattice between ADQW periods. The device is currently in the fabrication stage and hopefully successful results will be obtained in the near future. Finally, a more accurate model based on the self-consistent solution to the coupled Schrödinger and Poisson equations is currently being developed. The model will allow the investigation of trade-offs concerning doping densities and dopant positions within the ADQW structure. Thus, the ADQW and diode designs can be optimized.

APPENDIX A
FERMI'S GOLDEN RULE

In this appendix, modifications to Fermi's Golden Rule required for use in modeling intra- and inter-subband transitions in semiconductor quantum wells will be presented. The derivation starts from the usual form of Fermi's Golden Rule under the Born approximation. An additional assumption of isotropic in-plane effective mass is made, allowing the constant energy surfaces to be considered circular instead of elliptical rings.

The derivation begins with the usual form of Fermi's Golden Rule for transitions between discrete levels[62],

$$\frac{1}{\tau} = \frac{2\pi}{\hbar} \left| \langle \varphi_{k'}(\vec{r}) | V(\vec{r}) | \varphi_k(\vec{r}) \rangle \right|^2 \delta(\Theta) \quad (\text{A.1})$$

where $V(\vec{r})$ is a general scattering potential, $\varphi_k(\vec{r})$ and $\varphi_{k'}(\vec{r})$ are the initial and final state wavefunctions, and ε_k and $\varepsilon_{k'}$ are the initial and final state energies, respectively. In the case of elastic scattering $\Theta = \varepsilon_k - \varepsilon_{k'}$ and in the case of inelastic scattering $\Theta = \varepsilon_k - \varepsilon_{k'} \pm \hbar\omega$, where $\hbar\omega$ is the energy of the scattering particle. As shown in Fig. A.1, an electron in the initial state with energy ε_k can make the transition to the final state with energy $\varepsilon_{k'}$ for a number of final state in-plane momentum vectors.

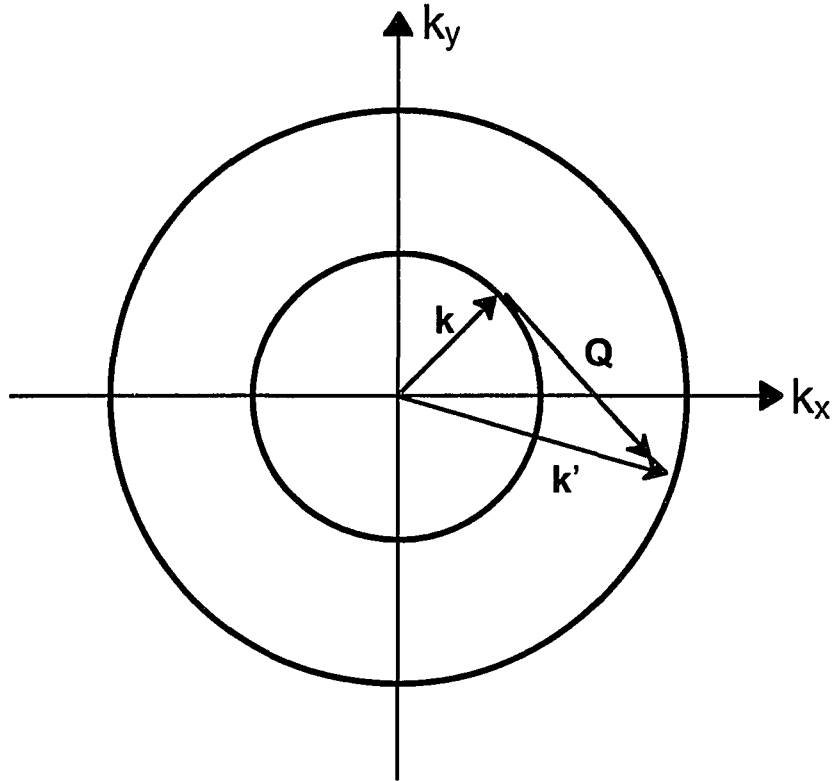


Figure A-1 Schematic diagram of momentum space showing the momentum conservation process for a transition from the initial state $|\epsilon_k, \bar{k}\rangle$ to the final state $|\epsilon_{k'}, \bar{k}'\rangle$.

As a result, Eq. A.1 must be summed over all possible final states, i.e.

$$\frac{1}{\tau} = \frac{2\pi}{\hbar} \sum \frac{\Delta \bar{k}'^2}{\Delta \bar{k}^2} \left| \langle \varphi_k(\bar{r}) | V(\bar{r}) | \varphi_{k'}(\bar{r}) \rangle \right|^2 \delta(\Theta) \quad (\text{A.2})$$

Rearranging this expression and converting the summation to an integral results in the following expression for the transition rate

$$\frac{1}{\tau} = \frac{2\pi}{\hbar \Delta \bar{k}^2} \int d^2 \bar{k}' \left| \langle \varphi_k(\bar{r}) | V(\bar{r}) | \varphi_{k'}(\bar{r}) \rangle \right|^2 \delta(\Theta) \quad (\text{A.3})$$

Since momentum space is circularly symmetric the integral is converted to polar coordinates and the substitution $\Delta k'^2 = 4\pi^2/S$, where S is the sample area, is made. The resulting expression is

$$\frac{1}{\tau} = \frac{S}{2\pi\hbar} \int k' dk' d\theta \left| \langle \phi_k(\bar{r}) | V(\bar{r}) | \phi_{k'}(\bar{r}) \rangle \right|^2 \delta(\Theta) \quad (\text{A.4})$$

Further simplification results upon making the substitution $dk' = d\varepsilon_k (dk'/d\varepsilon_k)$ and integrating Eq. A.4 with respect to ε_k ,

$$\frac{1}{\tau} = \frac{S}{2\pi\hbar} k' \left(\left| \frac{dk'}{d\varepsilon_k} \right| \right) \int_0^{2\pi} d\theta \left| \langle \phi_k(\bar{r}) | V(\bar{r}) | \phi_{k'}(\bar{r}) \rangle \right|^2 \quad (\text{A.5})$$

where from Fig. A.1 $Q^2 = k^2 + k'^2 - 2kk'\cos\theta$, and k and k' are the magnitudes of the initial and final state in-plane wave vectors, respectively.

After rearranging Eq. A.5, the desired expression for the transition rate is finally obtained,

$$\frac{1}{\tau} = \frac{S}{\hbar} \left[k' / \left| \frac{d\varepsilon_{k'}}{dk'} \right| \right] \frac{1}{2\pi} \int_0^{2\pi} d\theta \left| \langle \phi_k(\bar{r}) | V(\bar{r}) | \phi_{k'}(\bar{r}) \rangle \right|^2 \quad (\text{A.6})$$

In Eq. A.6, the term in brackets is the density of final states, while the integral is the average of the matrix element, $|\langle \phi_k(\bar{r}) | V(\bar{r}) | \phi_{k'}(\bar{r}) \rangle|^2$, over angle in momentum space. Equation A.6 is very general and can be applied to the calculation of intra- and inter-subband scattering and tunneling rates in quantum well structures.

APPENDIX B

INTER/INTRA-SUBBAND SCATTERING MECHANISMS

The derivation of inter/intra-subband scattering rates for various scattering mechanisms is the topic of this appendix. In particular, impurity scattering, alloy scattering, and polar LO-phonon scattering will be addressed. The final expressions are quite general and can be applied to both conduction and valence band scattering problems.

B.1 Impurity Scattering

For impurities in semiconductors, the scattering potential is given by [46]

$$V_{\text{imp}}(\vec{r}) = \frac{2\pi e^2}{\kappa_0 S} \sum_{\vec{R}_i} \sum_{\vec{Q}} \left(\frac{1}{Q} \right) \exp[i\vec{Q} \cdot (\vec{\rho} - \vec{\rho}_i) - Q|z - z_i|] \quad (\text{B.1})$$

where $\vec{R}_i = \vec{\rho}_i + z_i \hat{z}$ is the location of the impurities in the quantum well system, \vec{Q} is a two-dimensional wave vector, e is the electronic charge, κ_0 is the static dielectric constant, and S is the sample area, respectively. The wavefunctions of the system are assumed to be in the form

$$\varphi_k(\vec{r}) = \frac{1}{\sqrt{S}} \exp(i\vec{k} \cdot \vec{\rho}) \chi_k(z) \quad (\text{B.2})$$

where the exponential part is the in-plane component and $\chi_k(z)$ is the component parallel to the growth axis. The scattering potential given by Eq. B.1 is substituted into the

modified Fermi Golden Rule given by Eq. A.6. The matrix element $\langle \phi_{\mathbf{k}}(\bar{\mathbf{r}}) | V_{\text{imp}}(\bar{\mathbf{r}}) | \phi_{\mathbf{k}'}(\bar{\mathbf{r}}) \rangle$ is evaluated first. After some algebra the matrix element is given by the following integral

$$\langle || \rangle = \frac{2\pi e^2}{\kappa_0 S} \left(\frac{1}{S} \right) \sum_{\bar{\mathbf{R}}_j} \sum_{\bar{\mathbf{Q}}} \left(\frac{1}{Q} \right) \exp(-i\bar{\mathbf{Q}} \cdot \bar{\rho}_j) \int d^2\bar{\rho} \exp[i(\bar{\mathbf{k}} - \bar{\mathbf{k}}' + \bar{\mathbf{Q}}) \cdot \bar{\rho}] \cdot \int dz \chi_{\mathbf{k}}^*(z) \exp(-Q|z - z_j|) \chi_{\mathbf{k}}(z) \quad (\text{B.3})$$

The above integral can be greatly simplified by making the substitution

$$4\pi^2 \delta(\bar{\mathbf{Q}} + \bar{\mathbf{k}} - \bar{\mathbf{k}}') = \int d^2\bar{\rho} \exp[i(\bar{\mathbf{Q}} + \bar{\mathbf{k}} - \bar{\mathbf{k}}') \cdot \bar{\rho}]$$

The resulting expression for the matrix element is now

$$\langle || \rangle = \frac{2\pi e^2}{\kappa_0 S} \left(\frac{1}{S} \right) \sum_{\bar{\mathbf{R}}_j} \sum_{\bar{\mathbf{Q}}} \left(\frac{1}{Q} \right) \exp(-i\bar{\mathbf{Q}} \cdot \bar{\rho}_j) \cdot 4\pi^2 \delta(\bar{\mathbf{Q}} + \bar{\mathbf{k}} - \bar{\mathbf{k}}') \cdot \int dz \chi_{\mathbf{k}}^*(z) \exp(-Q|z - z_j|) \chi_{\mathbf{k}}(z) \quad (\text{B.4})$$

Rearranging this expression yields

$$\langle || \rangle = \frac{2\pi e^2}{\kappa_0 S} \left(\frac{1}{S} \right) 4\pi^2 \sum_{\bar{\mathbf{R}}_j} \sum_{\bar{\mathbf{Q}}} \frac{I(\mathbf{Q}, z_j)}{Q} \exp(-i\bar{\mathbf{Q}} \cdot \bar{\rho}_j) \delta(\bar{\mathbf{Q}} + \bar{\mathbf{k}} - \bar{\mathbf{k}}') \quad (\text{B.5})$$

Where in Eq. B.5 we have made the substitution

$$I(\mathbf{Q}, z_j) = \int dz \chi_{\mathbf{k}}^*(z) \exp(-Q|z - z_j|) \chi_{\mathbf{k}}(z) \quad (\text{B.6})$$

Now, making use of the identity

$$\sum_{\bar{\mathbf{Q}}} = \sum_{\bar{\mathbf{Q}}} \frac{\Delta\bar{\mathbf{Q}}}{\Delta\bar{\mathbf{Q}}} \rightarrow \frac{S}{4\pi^2} \int d\bar{\mathbf{Q}}$$

Equation B.5 becomes

$$\langle || \rangle = \frac{2\pi e^2}{\kappa_o S} \sum_{\bar{R}_j} \int d\bar{Q} \frac{I(Q, z_j)}{Q} \exp(-i\bar{Q} \cdot \bar{\rho}_j) \delta(\bar{Q} + \bar{k} - \bar{k}') \quad (\text{B.7})$$

Upon evaluating the integral and letting $\bar{Q} = \bar{k} - \bar{k}'$, the matrix element is

$$\langle || \rangle = \frac{2\pi e^2}{\kappa_o S} \left[\frac{I(Q, z_j)}{Q} \right] \sum_{\bar{R}_j} \exp(-i\bar{Q} \cdot \bar{\rho}_j) \quad (\text{B.8})$$

In Eq. A.6 the squared-modulus of the matrix element is desired. Hence, we evaluate the squared-modulus of Eq. B.8:

$$\langle || | \rangle^2 = \left(\frac{2\pi e^2}{\kappa_o S} \right)^2 \frac{|I(Q, z_j)|^2}{Q^2} \left[\sum_{\bar{R}_j} \exp(i\bar{Q} \cdot \bar{\rho}_j) \right] \left[\sum_{\bar{R}_1} \exp(-i\bar{Q} \cdot \bar{\rho}_1) \right] \quad (\text{B.9})$$

Since the two summations are over plane-wave expansions, all the cross terms will be zero, as a result

$$\left[\sum_{\bar{R}_j} \exp(i\bar{Q} \cdot \bar{\rho}_j) \right] \left[\sum_{\bar{R}_1} \exp(-i\bar{Q} \cdot \bar{\rho}_1) \right] = M \quad (\text{B.10})$$

where M is the number of impurities in the sample plane. Finally, the squared-modulus of the matrix element for impurity scattering is

$$\langle || | \rangle^2 = \left(\frac{2\pi e^2}{\kappa_o} \right)^2 \frac{N_{\text{imp}}}{S} \frac{|I(Q, z_j)|^2}{Q^2} \quad (\text{B.11})$$

where $N_{\text{imp}} = M/S$ and is the areal impurity concentration. Upon substituting this expression into Eq. A.6, we finally get the following expression for the impurity scattering rate

$$\left(\frac{1}{\tau}\right)_{\text{imp}} = \frac{2\pi}{\hbar} \left(\frac{e^2}{\kappa_0}\right)^2 N_{\text{imp}} \left\{k' / |d\epsilon_{k'} / dk'|\right\} \int_0^{2\pi} \frac{|I(Q, z_j)|^2}{Q^2} d\theta \quad (\text{B.12})$$

B.2 Alloy Scattering

In ternary semiconductors, fluctuations in the lattice potential due to alloy disorder can contribute to inter/intra-subband scattering. Bastard has used the following potential to model the effects of alloy fluctuations on scattering [42]:

$$V_{\text{alloy}}(\vec{r}) = \Omega_0 \delta V \left[\sum_{\vec{R}_B} x \delta(\vec{r} - \vec{R}_B) - \sum_{\vec{R}_A} (1-x) \delta(\vec{r} - \vec{R}_A) \right] \quad (\text{B.13})$$

where Ω_0 is the volume of the alloy unit cell, δV is the spatial average of the fluctuating alloy potential over the alloy unit cell, x is the A mole fraction in the ternary alloy $A_x B_{1-x} C$, and \vec{R}_i ($i = A$ or B) is the spatial position of the scattering site. Assuming the wavefunctions are given by Eq. B.2 and substituting Eq. B.13 into the matrix element of Eq. A.6, the matrix element can be expressed as

$$\langle || \rangle = \frac{\Omega_0 \delta V}{S} \left[- \sum_{\vec{R}_A} (1-x) \int \exp[i(\vec{k} - \vec{k}') \cdot \vec{\rho}] \delta(\vec{\rho} - \vec{P}_A) d^2 \vec{\rho} \cdot \int \chi_{k'}^*(z) \chi_k(z) \delta(z - Z_A) dz \right. \\ \left. + \sum_{\vec{R}_B} (x) \int \exp[i(\vec{k} - \vec{k}') \cdot \vec{\rho}] \delta(\vec{\rho} - \vec{P}_B) d^2 \vec{\rho} \int \chi_{k'}^*(z) \chi_k(z) \delta(z - Z_B) dz \right] \quad (\text{B.14})$$

where the substitutions $\delta(\vec{\rho} - \vec{P}_i) \delta(z - Z_i)$ and $\vec{R}_i = \vec{P}_i + Z_i \hat{z}$ have been made. Upon evaluation of the integrals and letting $\vec{Q} = \vec{k} - \vec{k}'$, Eq. B.14 can be reduced to

$$\begin{aligned} \langle || \rangle = \frac{\Omega_0 \delta V}{S} & \left[- \sum_{\bar{R}_A} (1-x) \exp[i\bar{Q} \cdot \bar{P}_A] \chi_{k'}^*(Z_A) \chi_k(Z_A) \right. \\ & \left. + \sum_{\bar{R}_B} (x) \exp[i\bar{Q} \cdot \bar{P}_B] \chi_{k'}^*(Z_B) \chi_k(Z_B) \right] \end{aligned} \quad (\text{B.15})$$

Since the positions of atoms B and C are randomly distributed throughout the lattice, the average of the squared-modulus of Eq. B.15 over the entire volume of the sample must be used in Eq. A.6. After considerable algebra, the squared-modulus of this expression can be shown to be

$$\begin{aligned} \langle | | \rangle^2 = \frac{\Omega_0}{S^2} \Omega [\delta V]^2 x(1-x) & \left\{ |\chi_{k'}(z)|^2 |\chi_k(z)|^2 \right. \\ & - \frac{\Omega_0}{\Omega} \sum_{\bar{R}_B} \exp[i\bar{Q} \cdot \bar{P}_B] \chi_{k'}^*(Z_B) \chi_k(Z_B) \sum_{\bar{R}_A} \exp[i\bar{Q} \cdot \bar{P}_A] \chi_{k'}(Z_A) \chi_k^*(Z_A) \\ & \left. - \frac{\Omega_0}{\Omega} \sum_{\bar{R}_A} \exp[i\bar{Q} \cdot \bar{P}_A] \chi_{k'}^*(Z_A) \chi_k(Z_A) \sum_{\bar{R}_B} \exp[i\bar{Q} \cdot \bar{P}_B] \chi_{k'}(Z_B) \chi_k^*(Z_B) \right\} \end{aligned} \quad (\text{B.16})$$

where Ω is the volume of the sample. Averaging Eq. B.16 over the entire sample volume results in

$$\begin{aligned} \langle | | \rangle^2 = \frac{\Omega_0}{S^2} [\delta V]^2 x(1-x) & \int |\chi_{k'}(z)|^2 |\chi_k(z)|^2 dz \{ S \\ & - \frac{\Omega_0}{\Omega} \sum_{\bar{R}_B} \sum_{\bar{R}_A} \int \exp[i\bar{Q} \cdot (\bar{\rho}_A - \bar{\rho}_B)] d^2 \bar{\rho} - \frac{\Omega_0}{\Omega} \sum_{\bar{R}_A} \sum_{\bar{R}_B} \int \exp[i\bar{Q} \cdot (\bar{\rho}_B - \bar{\rho}_A)] d^2 \bar{\rho} \} \end{aligned} \quad (\text{B.17})$$

The integrals over $\bar{\rho}$ in the last two terms will only be nonzero when $\bar{\rho}_A = \bar{\rho}_B$. However, for crystalline materials this can never occur, and as a result, the last two terms in Eq. B.17 are zero. Hence, the averaged squared-modulus of the matrix element is simply

$$\langle | \langle I | I \rangle |^2 \rangle = \frac{\Omega_o}{S} [\delta V]^2 x(1-x) \int |\chi_{k'}(z)|^2 |\chi_k(z)|^2 dz \quad (\text{B.18})$$

Finally, upon substituting this expression into Eq. A.6 and integrating with respect to θ , the expression for the alloy scattering rate is

$$\left(\frac{1}{\tau} \right)_{\text{alloy}} = \frac{\Omega_o}{\hbar} [\delta V]^2 x(1-x) \{k' / |d\epsilon_{k'} / dk'|\} \int |\chi_{k'}(z)|^2 |\chi_k(z)|^2 dz \quad (\text{B.19})$$

B.3 Polar LO-Phonon Scattering

The interaction of electrons with lattice vibrations can induce inter/intra-subband transitions in semiconductors. In particular, the interaction of electrons with LO-phonons can be a very fast, i.e. on the order of picoseconds, scattering mechanism. To treat the electron/LO-phonon interaction, the following scattering potential is employed [62]:

$$V_{\text{LO}}(\vec{r}, \vec{q}) = C(\vec{q}) a^+ \exp(-i\vec{q} \cdot \vec{r}) + C^*(\vec{q}) a^- \exp(+i\vec{q} \cdot \vec{r}) \quad (\text{B.20})$$

where a^+ and a^- are the creation and annihilation operators for a phonon in the mode \vec{q} , and $|C(\vec{q})|^2$ in the Fröhlich coupling constant and is defined as

$$|C(\vec{q})|^2 = \frac{2\pi e^2 \hbar \omega_{\text{LO}}}{\Omega q^2} \left(\frac{1}{\kappa_{\infty}} - \frac{1}{\kappa_0} \right) \quad (\text{B.21})$$

where ω_{LO} is the angular frequency of the LO phonon, e is the electronic charge, κ_0 and κ_{∞} are the static and dynamic dielectric constants of the crystal, respectively, $\Omega = SL$ is the

volume of the sample, and \hbar is Planck's constant divided by 2π . Since both electrons and phonons are involved, the total wavefunctions for the initial and final states will consist of two components, the initial state $|i\rangle = |\varphi_k, P_i\rangle$ corresponding to the initial electron and phonon states, respectively, and the final state $|f\rangle = |\varphi_{k'}, P_f\rangle$ corresponding to the final electron and phonon states, respectively. The matrix element in Eq. A.6 becomes

$$\langle || \rangle = \langle \varphi_{k'}, P_f | C(\bar{q}) a^+ \exp(-i\bar{q} \cdot \bar{r}) | \varphi_k, P_i \rangle + \langle \varphi_{k'}, P_f | C^*(\bar{q}) a^- \exp(+i\bar{q} \cdot \bar{r}) | \varphi_k, P_i \rangle \quad (\text{B.22})$$

The first term corresponds to phonon emission and the second term corresponds to phonon absorption. The operators a^+ and a^- only operate on the phonon states (assumed to be harmonic oscillator states). Thus, Eq. B.22 can be reduced to

$$\langle || \rangle = C(\bar{q}) \sqrt{N+1} \langle \varphi_{k'} | \exp(-i\bar{q} \cdot \bar{r}) | \varphi_k \rangle + C^*(\bar{q}) \sqrt{N} \langle \varphi_{k'} | \exp(+i\bar{q} \cdot \bar{r}) | \varphi_k \rangle \quad (\text{B.23})$$

where N is the phonon occupation number and is equal to

$$N = \frac{1}{\exp(\hbar\omega_{LO}/KT) - 1} \quad (\text{B.24})$$

where K is Boltzmann's constant, and T is the lattice temperature. The overlap integrals in Eq. B.23 can be greatly simplified by substituting wavefunctions of the form given by Eq. B.2 and evaluating the resulting integrals, i.e.

$$\langle \varphi_{k'} | \exp(\pm i\bar{q} \cdot \bar{r}) | \varphi_k \rangle = \frac{1}{S} \iint \exp[i(\bar{k} - \bar{k}' \mp \bar{Q}) \cdot \bar{\rho}] d^2\bar{\rho} \int \chi_k(z) \exp(\pm iq_z z) \chi_{k'}^*(z) dz \quad (\text{B.25})$$

where $\bar{r} = \bar{\rho} + z \hat{z}$ and $\bar{q} = \bar{Q} + q_z \hat{z}$. The integral over $\bar{\rho}$ can be separated into integrals over x and y , respectively, thus the matrix element can be further reduced to

$$\langle || | \rangle = \frac{4}{S} \left\{ \frac{1}{\beta_x \beta_y} \sin[\beta_x(L/2)] \sin[\beta_y(L/2)] \right\} I^\pm(q_z) \equiv \frac{4}{S} \Lambda^\mp(\beta_x, \beta_y) I^\pm(q_z) \quad (\text{B.26})$$

where

$$I^\pm(q_z) = \int \chi_k(z) \exp(\pm i q_z z) \chi_k^*(z) dz \quad (\text{B.27})$$

and $\beta_x = k_x - k_x \pm Q_x$ and $\beta_y = k_y - k_y \pm Q_y$, respectively. The total matrix element given by Eq. B.23 becomes

$$\langle || | \rangle = \frac{4}{S} C(\bar{q}) \sqrt{N+1} \Lambda^-(\beta_x, \beta_y) I^-(q_z) + \frac{4}{S} C^*(\bar{q}) \sqrt{N} \Lambda^+(\beta_x, \beta_y) I^+(q_z) \quad (\text{B.28})$$

Taking the magnitude-squared of Eq. B.28 results in

$$\langle || | \rangle^2 = \frac{16}{S^2} |C(\bar{q})|^2 (N+1) |\Lambda^-(\beta_x, \beta_y)|^2 |I^-(q_z)|^2 + \frac{16}{S^2} |C(\bar{q})|^2 N |\Lambda^+(\beta_x, \beta_y)|^2 |I^+(q_z)|^2 \quad (\text{B.29})$$

In the limit of an infinitely large volume, i.e. $L \rightarrow \infty$,

$$\lim_{L \rightarrow \infty} |4\Lambda^\mp(\beta_x, \beta_y)|^2 \rightarrow 4\pi^2 L^2 \delta(\beta_x) \delta(\beta_y)$$

and, as a result, Eq. B.29 can be reduced to

$$\langle || | \rangle^2 = \frac{4\pi^2}{S} |C(\bar{q})|^2 \left[(N+1) \delta(\bar{k} - \bar{k}' - \bar{Q}) |I^-(q_z)|^2 + N \delta(\bar{k} - \bar{k}' + \bar{Q}) |I^+(q_z)|^2 \right] \quad (\text{B.30})$$

where we have made use of the fact that $S = L^2$ and $\delta(\beta_x) \delta(\beta_y) = \delta(\bar{k} - \bar{k}' \pm \bar{Q})$.

Equation B.30 represents the magnitude-squared of the matrix-element for the interaction of an electron and a single LO phonon. Hence, we need to sum Eq. B.30 over all possible phonon modes, \bar{q} , i.e.

$$| \langle \parallel \rangle |^2 = \frac{4\pi^2}{S} \sum_{\bar{q}} |C(\bar{q})|^2 \left[(N+1) \delta(\bar{k} - \bar{k}' - \bar{Q}) |I^-(q_z)|^2 + N \delta(\bar{k} - \bar{k}' + \bar{Q}) |I^+(q_z)|^2 \right] \quad (\text{B.31})$$

Next, making use of Eq. B.21 and the identity

$$\sum_{\bar{q}} = \sum_{\bar{q}} \frac{\Delta^3 \bar{q}}{\Delta^3 \bar{q}} \rightarrow \frac{\Omega}{8\pi^3} \int d^2 \bar{Q} \int dq_z$$

this expression becomes

$$| \langle \parallel \rangle |^2 = \frac{e^2 \hbar \omega_{\text{LO}}}{\kappa_p S} \left[(N+1) \iint \frac{|I^-(q_z)|^2}{Q^2 + q_z^2} \delta(\bar{k} - \bar{k}' - \bar{Q}) d^2 \bar{Q} dq_z \right. \\ \left. + N \iint \frac{|I^+(q_z)|^2}{Q^2 + q_z^2} \delta(\bar{k} - \bar{k}' + \bar{Q}) d^2 \bar{Q} dq_z \right] \quad (\text{B.32})$$

where $q^2 = Q^2 + q_z^2$ and $\kappa_p^{-1} = \kappa_\infty^{-1} - \kappa_0^{-1}$, respectively. Performing the integral over Q ensures conservation of in-plane momentum, i.e. $\bar{Q} = \pm(\bar{k} - \bar{k}')$. Additionally, the integration over q_z can be shown to be equal to

$$\int \frac{|I^\pm(q_z)|^2}{Q^2 + q_z^2} dq_z = \frac{\pi}{Q^\pm} \iint \chi_k(z) \chi_{k'}(z) \exp(-Q^\pm |z - z'|) \chi_k(z') \chi_{k'}(z') dz' dz \equiv I(Q^\pm) \quad (\text{B.33})$$

In general, the final state momentum will be different for phonon emission (- sign) and phonon absorption (+ sign). Hence, upon substituting Eq. B.32 into Eq. A.6, we finally get the following expression for the polar LO-phonon scattering rate

$$\left(\frac{1}{\tau} \right)_{\text{LO}} = \frac{e^2 \omega_{\text{LO}}}{\kappa_p} \left\{ k' / |d\epsilon_{k'} / dk'| \right\} \frac{1}{2\pi} \int_0^{2\pi} \left[(N+1) I(Q^-) + N I(Q^+) \right] d\theta \quad (\text{B.34})$$

For electrons in semiconductor quantum well systems, the parabolic band approximation is justified, hence, the term in brackets is simply proportional to the two-dimensional density of states, i.e. m^*/\hbar^2 .

REFERENCES

1. N. Peyghambarian, S. W. Koch, and A. Mysyrowicz, *Introduction to Semiconductor Optics* (Prentice Hall, Englewood Cliffs, NJ, 1993).
2. P. R. Prucnal, R. K. Boncek, S. T. Johns, M. F. Krol, and J. L. Stacy, in *Photonic Switching and Interconnects*, edited by A. Marrakchi (Dekker, New York, 1994), p. 115.
3. C.C. Hsu, B.P. McGinnis, J.P. Sokoloff, G. Khitrova, H.M. Gibbs, N. Peyghambarian, S.T. Johns, and M.F. Krol, *J. Appl. Phys.* **70** (10) 5615 (1991).
4. M. G. W. Alexander, W. W. Rühle, R. Sauer, and W. T. Tsang, *Appl. Phys. Lett.* **55** (9) 885 (1989).
5. M. Tsuchiya, T. Matsusue, and H. Sakaki, *Phys. Rev. Lett.* **59** (20) 2356 (1987).
6. N. Sawaki, R. A. Höpfel, E. Gornik, and H. Kano, *Appl. Phys. Lett.* **55** (19) 1996 (1989).
7. M. Nido, M. G. W. Alexander, W. W. Rühle, T. Schweizer, and K. Köhler, *Appl. Phys. Lett.* **56** (4) 355 (1990).
8. G. Bastard, C. Delelande, R. Ferreira, and H. W. Liu, *J. of Lum.* **44** 247 (1989).
9. M. G. W. Alexander, M. Nido, W. W. Rühle, and K. Köhler, *Phys. Rev. B* **41** (17) 12295 (1990).
10. D. Y. Oberli, J. Shah, T. C. Damen, J. M. Kuo, J. E. Henry, J. Lary, and S. M. Goodnick, *Appl. Phys. Lett.* **56** (13) 1239 (1990).
11. B. Deveaud, A. Chomette, F. Clerot, P. Auvray, A. Regreny, R. Ferreira, and G. Bastard, *Phys. Rev. B* **42** (11) 7021 (1990).
12. R. Strobel, R. Eccleston, J. Kuhl, and K. Köhler, *Phys. Rev. B* **43** (15) 12564 (1991).
13. R. Ferreira, P. Rolland, Ph. Roussignol, C. Delalande, A. Vinattieri, L. Carraresi, M. Colocci, N. Roy, B. Sermage, J. F. Palmier, and B. Etienne, *Phys. Rev. B* **45** (20) 11782 (1992).

REFERENCES - *Continued*

14. R. Ferreira and G. Bastard, *EuroPhys. Lett.* **10** (3) 279 (1989).
15. K. Leo, J. Shah, J. P. Gordon, T. C. Damen, D. A. B. Miller, C. W. Tu, and J. E. Cunningham, *Phys. Rev. B* **42** (11) 7065 (1990).
16. M. Nido, M. G. W. Alexander, W. W. Rühle, and K. Köhler, *Phys. Rev. B* **43** (2) 1839 (1991).
17. T. B. Norris, N. Vodjdani, B. Vinter, E. Costard, and E. Böckenhoff, *Phys. Rev. B* **43** (2) 1867 (1991).
18. Ph. Roussignol, A. Vinattieri, L. Carraresi, M. Colocci, and A. Fasolino, *Phys. Rev. B* **44** (16) 8873 (1991).
19. A. Tackeuchi, S. Muto, T. Inata, and T. Fujii, *Appl. Phys. Lett.* **58** (15) 1670 (1991).
20. C. Tanguy, B. Deveaud, A. Regreny, D. Hulin, and A. Antonetti, *Appl. Phys. Lett.* **58** (12) 1283 (1991).
21. M. N. Islam, R. L. Hillman, D. A. B. Miller, D. S. Chemla, A. C. Gossard, and J. H. English, *Appl. Phys. Lett.* **50** (16) 1098 (1987).
22. J. W. Little and R. P. Leavitt, *Phys. Rev. B* **39** (2) 1365 (1989).
23. Y. J. Ding, C. L. Guo, S. Li, J. B. Khurgin, K. K. Law, J. Stellato, C. T. Law, A. E. Kaplan, L. A. Coldren, *Appl. Phys. Lett.* **59** (9) 1025 (1991).
24. R. P. Leavitt, J. W. Little, and S. C. Horst, *Phys. Rev. B* **40** (6) 4183 (1989).
25. A. M. Fox, D. A. B. Miller, G. Livescue, J. E. Cunningham, J. E. Henry, and W. Y. Jan, *Phys. Rev. B* **42** (3) 1841 (1990).
26. Y. Tokuda, K. Kanamoto, Y. Abe, and N. Tsukada, *Phys. Rev. B* **41** (14) 10280 (1990).

REFERENCES - *Continued*

27. N. Sawaki, M. Suzuki, E. Okuno, H. Goto, I. Akasaki, H. Kano, Y. Tanaka, and M. Hashimoto, *Solid-State Elec.* **31** (3/4) 351 (1988).
28. M. Wegener, T. Y. Chang, I. Bar-Joseph, J. M. Kuo, and D. S. Chémbla, *Appl. Phys. Lett.* **55** (6) 583 (1989).
29. M. Wegener, J. E. Zucker, T. Y. Chang, N. J. Sauer, K. L. Jones, and D. S. Chemla, *Phys. Rev. B* **41** (5) 3097 (1990).
30. J. Wang, J. E. Zucker, J. P. Leburton, T. Y. Chang, and N. J. Sauer, *Appl. Phys. Lett.* **65** (17) 2196 (1994).
31. N. Vodjdani, B. Vinter, V. Berger, E. Böckenhoff, and E. Costard, *Appl. Phys. Lett.* **59** (5) 556 (1991).
32. V. Berger, N. Vodjdani, B. Vinter, E. Costard, and E. Böckenhoff, *Appl. Phys. Lett.* **60** (15) 1870 (1992).
33. M. F. Krol, T. Ohtsuki, G. Khitrova, R. K. Boncek, B. P. McGinnis, H. M. Gibbs, and N. Peyghambarian, *Appl. Phys. Lett.* **62** (13) 1550 (1993).
34. M. F. Krol, M. S. Thesis, University of Arizona (1992).
35. M. F. Krol, S. Ten, B. P. McGinnis, M. J. Hayduk, G. Khitrova, and N. Peyghambarian, Submitted to *Phys. Rev. B* June 1995.
36. M. F. Krol, R. P. Leavitt, J. T. Pham, B. P. McGinnis, and N. Peyghambarian, *Appl. Phys. Lett.* **66** (22) 3045 (1995).
37. R. M. Kolbas and N. Holonyak, *Am. J. Phys.* **52** (5) 431 (1984).
38. R. P. Leavitt and J. L. Bradshaw, *J. Appl. Phys.* **76** (6) 3429 (1994).
39. G. Khitrova and H. M. Gibbs, private communication (1994).
40. J. Shah, *IEEE J. Quan. Elec.* **24**, 276 (1988).

REFERENCES - *Continued*

41. B. D. Flugel, Private Communication (1994).
42. G. Bastard, *Wave Mechanics Applied to Semiconductor Heterostructures* (Halsted Press, New York, 1988), Chapters 2,3,4, and 8.
43. J. M. Luttinger and W. Kohn, *Phys. Rev.* **97** (4) 869 (1955).
44. J. M. Luttinger, *Phys. Rev.* **102** (4) 1030 (1956).
45. W. H. Press, B. P. Flannery, S. A. Teukolsky, and W. T. Vetterling, *Numerical recipes in C: The art of scientific computing* (Cambridge University Press, New York, 1988), p. 360.
46. R. Ferreira and G. Bastard, *Phys. Rev. B* **43** (12) 9687 (1991).
47. G. Goldoni and A. Fasolino, *Phys. Rev. Lett.* **69** (17) 2567 (1992).
48. S. Mukhopadhyay and B. R. Nag, *Appl. Phys. Lett.* **60** (23) 2897 (1992).
49. J. S. Weiner, D. A. B. Miller, D. S. Chemla, T. C. Damen, C. A. Burrus, T. H. Wood, A. C. Gossard, and W. Wiegmann, *Appl. Phys. Lett.* **47**, 1148 (1985).
50. R. Shanker, *Principles of Quantum Mechanics* (Plenum Press, New York, 1980), p. 459.
51. R. L. Liboff, *Introductory Quantum Mechanics* (Addison-Wesley, New York, 1980), p.86.
52. E. J. Austin and M. Jaros, *Phys. Rev. B* **31** (8) 5569 (1985).
53. T. E. Wiest, M. J. Hayduk, and M. F. Krol, unpublished (1995).
54. K. Leo, J. Shah, E. O. Göbel, T. C. Damen, S. Schmitt-Rink, W. Schäfer, and K. Köhler, *Phys. Rev. Lett.* **66** (2) 201 (1991).
55. H. G. Roskos, M. C. Nuss, J. Shah, K. Leo, D. A. B. Miller, A. M. Fox, S. Schmitt-Rink, and K. Köhler, *Phys. Rev. Lett.* **68** (14) 2216 (1992).

REFERENCES - *Continued*

56. R. Sauer, K. Thonke, and W. T. Tsang, *Phys. Rev. Lett.* **61** (5) 609 (1988).
57. A. Abou-Elnour and K. Schuenemann, *IEEE MTT-S Digest*, paper HH-2, 1177 (1993).
58. see also A. Abou-Elnour and K. Schuenemann, *Solid State Elec.* **37** (1) 27 (1994) for a detailed discussion of the solution to the coupled Schrödinger/Poisson Equations.
59. C. Delalande, J. Orgonasi, J. A. Brum, G. Bastard, M. Voos, G. Weimann, and W. Schlapp, *Appl. Phys. Lett.* **51** (17) 1346 (1987).
60. J. L. Bradshaw, R. P. Leavitt, J. T. Pham, and F. J. Towner, *Phys. Rev. B* **49** (3) 1882 (1994).
61. J. Nelson, M. Paxman, K. W. J. Barnham, J. S. Roberts, and C. Button, *IEEE J. Quan. Elec.* **29** (6) 1460 (1993).
62. R. Ferreira and G. Bastard, *Phys. Rev. B* **40** (2) 1074 (1989).
63. G. W. Neudeck, *The PN Junction Diode (2nd. Edition)*, edited by G. W. Neudeck and R. F. Pierret (Addison-Wesley, New York, 1989), p. 27.